# Simulations and Mechanisms of Subtropical Low-cloud Response to Climate Change

Thesis by

Zhihong Tan

In Partial Fulfillment of the Requirements

for the Degree of

Doctor of Philosophy

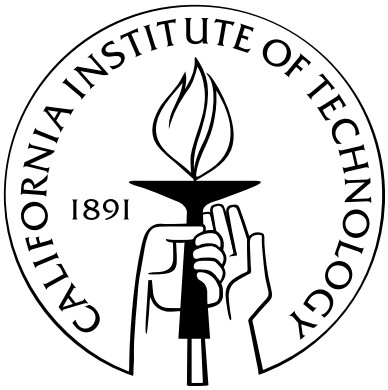


California Institute of Technology

Pasadena, California

2016

(Defended June 15, 2015)

*A bright moon rising above Tian Shan,*

*Lost in a vast ocean of clouds.*

*The long wind, across thousands upon thousands of miles,*

*Blows past the Jade-gate Pass.*

Moon over Mountain Pass

Li Po (tr. Joseph J. Lee)

# Acknowledgements

First, I would sincerely thank my advisor, Tapio Schneider, and my co-advisor, Joao Teixeira, for their great academic guidance during my PhD. My thesis work would not be possible without their scientific expertise on atmospheric dynamics, as well as their invaluable experience on how to survive and prosper in the academia. I would also thank the other members in my thesis committee, Simona Bordoni and John Seinfeld, for their advice and help during my approach to and beyond my PhD degree. I have also received great help from other professors and staff in Caltech, including but not limited to Paul Wennberg, Yuk L. Yung, Andy Ingersoll, Andy Thompson, Jess Adkins, Jared Leadbetter, Nora J. Oshima, Liz Muira Boyd, Kathy Young, and Dian Buchness, as well as Patricia Meile at ETH Zürich. I sincerely owe my thanks to them. I would like to especially thank my collaborators in the cloud research group for their help on coding and debugging the models, and on clarifying the scientific mechanism of clouds. They are Kyle Pressel, Colleen Kaul, Sally Zhang, Florent Brient, Cheikh Mbengue, Bettina Meyer, and Remi Lam. I am also grateful for the extremely helpful discussion with other colleagues in our group and more broadly in the ESE and planetary science at Caltech, including but not limited to Da Yang, Xavier Levine, Tim Merlis, Farid Ait-Chaalal, Robert Wills, Tobias Bischoff,

Michael Byrne, Ori Adam, and Jinqiang Chen.

My experience in both Caltech and ETH Zürich has been memorable, and I would like to thank my friends in both places. I would like to thank Cheng Li, Junle Jiang, and Yuhua Chen, for being my flatmates and enduring my lifestyle; Daiqi Linghu, Shuo Wang, Xi Zhang, Wendian Shi, Tong Chen, Yan Qu, Yubing Yang, and Qiong Zhang, for being wonderful companions in the wild and supporting me whenever I'm in need; Xin Ning, Yihe Huang, Xuan Zhang, Yingrui Chang, Hao Chu, Wen Yan, Yuan Lin, Xinyi Li, and Junliang Shen, for sharing part of their lives with me and making my past six years more enjoyable. Apart from these friends, I have also received help from many other people, to whom I have always been grateful.

Finally, I would like to thank my old classmates and teachers as well as my family in China. They have helped to shape me into the person I am today. My thoughts are always with them even though we are now thousands of miles apart. I would like to especially thank my parents, Min Zhou and Xiangtao Tan, for nurturing and caring me since I was born, and for always being supportive in my pursuit of my dreams.

# Abstract

This thesis focuses on improving the simulation skills and the theoretical understanding of the subtropical low cloud response to climate change.

First, an energetically consistent forcing framework is designed and implemented for the large eddy simulation (LES) of the low-cloud response to climate change. The three representative current-day subtropical low cloud regimes of cumulus (Cu), cumulus-over-stratocumulus, and stratocumulus (Sc) are all well simulated with this framework, and results are comparable to the conventional fixed-SST approach. However, the cumulus response to climate warming subject to energetic constraints differs significantly from the conventional approach with fixed SST. Under the energetic constraint, the subtropics warm less than the tropics, since longwave (LW) cooling is more efficient with the drier subtropical free troposphere. The surface latent heat flux (LHF) also increases only weakly subject to the surface energetic constraint. Both factors contribute to an increased estimated inversion strength (EIS), and decreased inversion height. The decreased Cu-depth contributes to a decrease of liquid water path (LWP) and weak positive cloud feedback. The conventional fixed-SST approach instead simulates a strong increase in LHF and deepening of the Cu layer, leading to a weakly negative cloud feedback. This illustrates the importance of energetic con-

straints to the simulation and understanding of the sign and magnitude of low-cloud feedback.

Second, an extended eddy-diffusivity mass-flux (EDMF) closure for the unified representation of sub-grid scale (SGS) turbulence and convection processes in general circulation models (GCM) is presented. The inclusion of prognostic terms and the elimination of the infinitesimal updraft fraction assumption makes it more flexible for implementation in models across different scales. This framework can be consistently extended to formulate multiple updrafts and downdrafts, as well as variances and covariances. It has been verified with LES in different boundary layer regimes in the current climate, and further development and implementation of this closure may help to improve our simulation skills and understanding of low-cloud feedback through GCMs.

# Contents

# List of Tables

# List of Figures

# Introduction

## 0.1 Background

Subtropical marine boundary layer (MBL) clouds cover a great proportion of the subtropical oceans and contribute strongly to Earth's radiation budget. Two major types of MBL clouds are the stratocumulus (Sc) and cumulus (Cu). Sc clouds prevail in the eastern boundary of subtropical oceans with low sea surface temperature (SST) under the subsiding branches of the Hadley and Walker circulations. The Sc layer is shallow and well-mixed, characterized by high liquid water path (LWP), almost 100% cloud fraction, high albedo, and locally very strong shortwave (SW) cooling effect (e.g., summertime San Francisco). Downwind of the stratocumulus region, where subsidence gradually weakens and SST increases, the Sc layer dissipates and a Cu layer develops, which has typical cloud cover of $\sim 15\%$ and produces much weaker shortwave (SW) cloud radiative effects (CRE) (e.g., Hawaii). However, because the Cu layer covers a much larger proportion of Earth's oceans, its cumulative SW effect is still important. How Sc and Cu clouds change in the future climate is still largely uncertain, and this has been shown to be the largest uncertainty in future climate projections (Bony and Dufresne, 2005; Soden and Held, 2006; Webb et al., 2006;

Dufresne and Bony, 2008; Vial et al., 2013).

The central difficulty in the study of low clouds is the wide range of scales and processes that may be important to cloud dynamics, spanning from the large-scale subsidence and advection that are determined by tropical circulation dynamics at scales of $10^3 - 10^4$ km, to the turbulence and cloud dynamics at the scale of $1 - 10$ m. Therefore, no model is able to resolve the whole range of scales involved, and the study of cloud dynamics usually involves a hierarchy of models at different scales, spanning from global-scale general circulation models (GCM), to the small-scale high-resolution models known as large-eddy simulation (LES). The small-scale turbulent-convection processes are represented by sub-grid scale (SGS) parameterization schemes in GCMs, and the large-scale dynamical processes need to be formulated in LES. These are both very difficult problems that can lead to misleading results if not handled properly.

The SGS parameterizations in GCMs are usually composed of several largely independent parameterization schemes for the different cloud and convective processes (cf. Neale et al., 2010; Donner et al., 2011). For example, a typical climate model separates the total SGS mixing into boundary layer turbulence, shallow convection, and deep convection, which are handled by different schemes. Turbulence is usually represented by eddy diffusivity (ED) and convection is usually parameterized by mass-flux (MF) of entraining plumes. The separation is often artificial, and the transition between different regimes may not be smooth even if it is driven by smoothly varying forcing. Also, these separate parameterizations usually do not converge as the resolution is increased or as physical limits are taken, such as the limit of the latent

heat of vaporization approaching zero in which all SGS closures should represent dry turbulence. The lack of consistency between turbulence and convection schemes have been shown to produce unphysical low cloud behaviors, induce current day biases on low cloud cover, and contribute to the disagreement in the predicted climate response (Nuijens et al., 2015; Brient et al., 2015). Therefore, a unified and physically consistent parameterization scheme is important for realistically representing low clouds in GCMs and reducing the model uncertainty of low cloud responses to climate change.

LES can explicitly simulate the dynamics of boundary layers and clouds, and they have been successful in reproducing the observed boundary layer structures, if realistic current-day forcing is given. However, to understand the climate-change response of low clouds, LES must be coupled to large-scale forcing representing future climate for which no observation is available. Therefore, simple assumptions are usually made for these scenarios, such as fixing the SST increase to match that of the free troposphere, effectively fixing the SST gradient between the subtropics and the tropics. The surface energy budget is not closed, and the surface latent heat flux (LHF) may increase according to the Clausius-Clapeyron relation (Rieck et al., 2012), far exceeding the decrease in the sea-surface net longwave (LW) cooling. Under such assumptions, the ocean acts like an infinite heat bath that can feed this LHF increase. It is unlikely that the ocean circulation can respond so efficiently to maintain the SST gradient. The large-scale forcing of the atmosphere also suffers similar problems, for which the change of upper-tropospheric temperature and the $CO_2$ forcing might not be coherent.

Bridging the gap between small-scale and large-scale models is among the central

difficulties that prevent a clearer understanding of how clouds respond to climate change. This motivates my thesis work on both approaches: to develop an energetically consistent formulation of large-scale forcing for studying the low-cloud response in LES, and to develop a unified and physically consistent parameterization of SGS turbulence and convection processes for studying the low-cloud response in GCMs.

## 0.2 Approach

The first and second chapters of this thesis are motivated by the CGILS LES intercomparison project (Blossey et al., 2013) and the related single-column model (SCM) intercomparison project (Zhang et al., 2013). Unlike previous studies on the transient evolution of low clouds, the CGILS study specifically focuses on the steady state low-cloud regimes in the current climate as well as their response to the perturbed climate for all three representative low-cloud regimes: Sc, Sc-over-Cu, and Cu. It is by far the most systematic endeavor to investigate the low-cloud response under warming conditions. However, the CGILS approach of individually prescribing the SST and upper-tropospheric temperature change without the corresponding change in $CO_2$ may not be a very realistic representation of climate change. Our approach is to start from current low-cloud regimes that are similar to the CGILS study, and study the cloud response to the radiatively-driven climate change of an atmospheric column coupled with a mixed-layer ocean, for which the ocean heat uptake is prescribed but SST is allowed to evolve freely. This approach is commonly used in idealized GCM studies of climate change, such as O'Gorman and Schneider (2008). By fixing surface

heat uptake, the surface energy budget in the steady state is well constrained. Most significantly, the surface LHF under the energetic constraint cannot increase with the Clausius-Clapeyon relation, since no energy source term can compensate for such an exponentially increasing loss of surface energy as the temperature increases. LHF only increases at about 2% $K^{-1}$, only one third of the Clausius-Clapeyon relation of 6% $K^{-1}$, consistent with Held and Soden (2006) and O'Gorman and Schneider (2008). As shown in the second chapter, this is one of the major differences that cause a very different cumulus response under the assumption of fixed surface flux compared to that of fixed SST.

The third chapter of this thesis develops further the eddy-diffusivity mass-flux (EDMF) parameterization introduced by Siebesma and Teixeira (2000), Soares et al. (2004), Siebesma et al. (2007), and Witek et al. (2011). In contrast to the conventional approach of representing the boundary layer completely by ED, and initializing the cumulus updraft at the cloud base with some closure assumptions for MF which may cause a discontinuity of fluxes, the EDMF approach decomposes the boundary layer into the environment and the dry updrafts that are initialized from the most buoyant air parcels in the surface layer. The coexistence of ED and MF components in the boundary layer allows them to interact and adjust continuously, and updrafts that reach the lifted condensation level (LCL) grow into cumulus clouds. Therefore, no cumulus MF closure at cloud base is needed, and the coupling between the boundary layer and the cumulus is more consistent. Starting from this approach, the EDMF equations are reexamined from the viewpoint of domain decomposition, so that the

inclusion of multiple non-steady updrafts and downdrafts and of the second-order moment equations becomes natural. This is suitable to serve as a unified and consistent framework for representing the various SGS processes, including turbulence, shallow convection, deep convection, and the precipitation downdrafts.

## 0.3 Outline of this thesis

This thesis work is composed of three parts. The first chapter is focused on the development of an energetically consistent framework for the LES study on the low cloud response, and the validation of this forcing framework for realistically representing the Sc, Sc-over-Cu, and Cu regimes in the current climate. The second chapter is focused on the investigation of the subtropical cumulus response to warming using the same framework, and contrasting this with the cumulus response under the conventional assumption of fixed SST. The third chapter is focused on the development of an EDMF closure for the unified representation of turbulence and convection processes, and its validation against LES results of boundary layer regimes in the current climate.

# Chapter 1

# Large-eddy simulation of subtropical cloud-topped boundary layers. Part I: Model configuration and role of surface energy balance

## 1.1 Introduction

Marine boundary layers (MBL) over subtropical oceans are often topped by low clouds, predominantly stratocumuli and cumuli (Stevens, 2005). Stratocumuli (Sc) are abundant over the eastern boundaries of subtropical oceans, in the subsiding branches of the Walker and Hadley circulations and over relatively cool sea surfaces. Sc form a dense cover with high albedo exerting a strong shortwave (SW) cooling on the surface locally. Cumuli (Cu) occur over the interiors of subtropical oceans, where subsidence is weaker and sea surfaces are warmer. Although the local albedo modification of Cu is weaker because of their lower fractional cloud cover, they occur over a much greater portion of subtropical ocean surfaces. Therefore, they are also

important regulators of Earth's radiative energy budget. How these clouds change as the climate warms and the large-scale conditions in which they are embedded change remains one of the central unresolved questions in climate dynamics. Uncertainties about this cloud response dominate uncertainties in climate change projections (e.g., Cess et al., 1990, 1996; Bony and Dufresne, 2005; Webb et al., 2006; Dufresne and Bony, 2008; Vial et al., 2013).

Large-eddy simulations (LES) have the potential to reduce these uncertainties because it can explicitly simulate the dynamics of boundary layers and clouds, albeit only in a limited computational domain that typically extends at most over $O(10\ \mathrm{km})$ in the horizontal. LES have been successful in reproducing observed boundary layers topped with Sc (Duynkerke et al., 1999; Stevens et al., 2005; Caldwell and Bretherton, 2009) and Cu (Siebesma et al., 2003; vanZanten et al., 2011). They have also been used to explore how Sc and Cu respond to perturbations in surface temperatures or in large-scale processes such as subsidence that are externally prescribed in LES (e.g., Sandu and Stevens, 2011; Chung et al., 2012; Bellon and Stevens, 2012; Rieck et al., 2012; Bretherton et al., 2013). However, the cloud response to perturbations depends on how the large-scale processes are represented in LES, making it difficult to compare LES results obtained under different large-scale forcing frameworks. To remedy this difficulty in comparing simulation results, the CFMIP/GASS Intercomparison of Large-Eddy and Single-Column Models (CGILS) project recently established a large-scale forcing protocol for LES at a few key locations, representing subtropical Sc, Sc-over-Cu, and Cu regimes (Zhang et al., 2013). The CGILS framework has also

been used to study the cloud response to idealized climate changes, such as a 2-K warming of the surface accompanied by weakened subsidence (Blossey et al., 2013; Bretherton et al., 2013). This has provided insight into the mechanisms responsible for the cloud response to climate changes.

Questions remain, however, whether the perturbations to large-scale conditions prescribed in LES represent realizable climate changes, and thus whether the cloud responses obtained in LES are actually those that will be realized under climate change. For example, when sea surface temperatures (SST) at the lower boundary are prescribed, as is typically done in LES of subtropical MBL clouds, the surface energy budget is not closed. The ocean surface represents an infinite heat bath that can provide fluxes of latent and sensible heat irrespective of the energetic constraints that the real ocean surface usually has to satisfy. Global warming is represented as an prescribed SST increase in this framework, and if the MBL relative humidity is constrained to stay constant (e.g., Rieck et al., 2012), latent heat fluxes (LHF) at the surface will increase rapidly with SST, at the rate given by the Clausius-Clapeyron relation: around 6–7% per kelvin SST warming. In reality, however, LHFs at the surface are energetically constrained—radiative energy is needed to evaporate water. LHFs increase more slowly with SST than indicated by the Clausius-Clapeyron rate: at around 2–3% per kelvin SST warming (Boer, 1993; Knutson and Manabe, 1995; Held and Soden, 2000; Allen and Ingram, 2002; Held and Soden, 2006; Stephens and Ellis, 2008; Schneider et al., 2010). The excessive LHFs arising when warming is represented by an SST increase without closing the surface energy budget can distort

the cloud response to warming, e.g., through distortions in moisture or buoyancy fluxes near the surface.

Here we present a framework of forcing LES that closes the surface energy budget and thus guarantees realizable changes of surface fluxes in response to climate changes. This is achieved by coupling the LES domain to a mixed-layer (slab) ocean that satisfies an energy balance equation, similar to what is commonly done in studies of large-scale dynamics with idealized GCMs (e.g., Frierson et al., 2006; O'Gorman and Schneider, 2008). The surface temperature is no longer prescribed but evolves in accordance with the energy balance. Thus, the surface temperature achieved under this framework depends on energetic forcing parameters, such as the longwave opacity of the atmosphere. Radiative transfer in the atmosphere must also be represented, as well as any large-scale energy fluxes within the atmosphere that are necessary to achieve closure of the atmospheric energy balance. In the free troposphere, we exploit the weakness of horizontal temperature gradients within the tropics (Charney, 1963; Sobel et al., 2001) to represent the effect of large-scale energy fluxes as relaxation to a temperature profile that is representative of the convecting branch of the tropical circulation and is in radiative-convective equilibrium (RCE) with the given energetic forcing parameters. This guarantees broad dynamical consistency between the warming in the free troposphere and in the boundary layer that results, for example, when the concentration of well-mixed greenhouse gases is increased.

We test this forcing framework with the Python Cloud Large Eddy Simulation code (PyCLES, Pressel et al., 2015), coupled to the Rapid Radiative Transfer Model

for GCM Applications (RRTMG, Iacono et al., 2008). We simulate three cases representative of Sc, Sc-over-Cu, and Cu regimes that were also considered under the CGILS framework. Qualitative agreement between the results under our framework and those under CGILS verifies the capacity of the new framework to reproduce the three cloud regimes. Sensitivity tests show that the model results are relatively insensitive to the resolution and domain size. However, they are relatively sensitive to microphysical parameters determining precipitation efficiency. In Chapter 2, we show how this forcing framework can be used to study the response of MBL clouds to changing greenhouse gas concentrations.

This chapter is organized as follows: Section 1.2 describes the PyCLES model and the formulation of large-scale forcings and surface boundary conditions. Section 1.3 describes the experimental set-up of the three representative MBL cloud cases. Section 1.4 presents the LES results under our forcing framework and compares them with results under the CGILS framework. Section 1.5 describes some sensitivity studies. Section 1.6 summarizes our conclusions and their implications for studies of climate change.

## 1.2 Model and forcing framework

### 1.2.1 LES code

We use the PyCLES code, which solves the moist anelastic equations of Pauluis (2008) with specific entropy $s$ and total water specific humidity $q_t$ as prognostic thermody-

namic variables (Pressel et al., 2015). It uses Weighted Essentially Non-oscillatory (WENO) transport schemes for momentum and scalars on a uniform Arakawa C-grid (Arakawa and Lamb, 1977; Liu et al., 1994; Jiang and Shu, 1996; Balsara and Shu, 2000). We use a 5th-order WENO scheme in this study. For time-stepping, we use the strong stability preserving (SSP) 4nd-order, 4-stage Runge-Kutta (RK) method of Shu and Osher (1988), with adaptive time-steps and with a target Courant number of 0.7.

Subgrid-scale (SGS) fluxes of momentum and scalars are computed with the Smagorinsky–Lilly closure (Smagorinsky, 1963; Lilly, 1962), with Smagorinsky coefficient $c_S = 0.23$ and a turbulent Prandtl number $\mathrm{Pr}_t = 1/3$. The momentum, entropy, and water vapor fluxes at the lower boundary are computed using standard bulk aerodynamic formulas, with near-surface fluxes determined by Monin-Obukhov similarity theory (Byun, 1990). The roughness lengths of momentum and entropy (including sensible and latent heat) are $z_m = 10^{-3}$ m and $3 \times 10^{-5}$ m, respectively. At the upper boundary, all fluxes (except radiative fluxes) are set to zero. A sponge layer extends over the top 500 m of the domain and linearly damps fluctuations to the domain mean. See Pressel et al. (2015) for details of the LES code.

### 1.2.2 Radiative transfer

To achieve a closed energy budget at the surface, we need to model radiative transfer. To do so, we integrated the RRTMG scheme (Iacono et al., 2008) in PyCLES. The LES code provides values of temperature ($T$), specific humidity of water vapor ($q_v$),

and specific humidity of cloud liquid ($q_l$) for the radiative transfer calculations in RRTMG. The vertical profiles of ozone are prescribed individually for each case, whereas the default RRTMG concentrations are used for other greenhouse gases. Following Blossey et al. (2013), we estimate the cloud droplet effective radius $r_{\text{eff}}$ needed in radiative transfer calculations from the volume-mean radius

$$r_v = \left( \frac{3\rho_a q_l}{4\pi\rho_l N_d} \right), \tag{1.1}$$

as

$$r_{\text{eff}} = r_v \exp\left[\log(\sigma_g)^2\right], \tag{1.2}$$

where $\sigma_g = 1.2$ is the geometric standard deviation of an assumed log-normal droplet radius distribution (Ackerman et al., 2009). Other constants and variables appearing in these expressions are the density of air $\rho_a$, the density of liquid water $\rho_l$, and an assumed cloud droplet concentration $N_d = 100$ cm$^{-3}$.

Because the LES domain has limited height (5 km in our case), whereas radiative energy fluxes substantially interact with the atmosphere to much greater heights, the radiative transfer calculations need to be extended from the top of the LES domain to the top of the atmosphere (TOA). We do so by extending the reference profiles of temperature and specific humidity used for the large-scale forcing (to be discussed below) to TOA.

Radiative transfer is computed with the RRTMG scheme every 60 seconds. Radiative heating/cooling rates are computed and applied column-by-column within the

LES domain. We have also experimented with horizontally homogenized radiative forcings, computed with horizontally averaged fields in the LES domain. However, the missing local radiative feedback affected the LES's ability to simulate the Cu-over-Sc case.

### 1.2.3 Surface energy balance

A mixed-layer (slab) ocean is coupled to the LES domain and its sea surface temperature (SST, or $T_s$) evolves according to the surface energy balance:

$$(\rho_w C_w H_w)\frac{dT_s}{dt} = F^{\downarrow}_{\mathrm{SW}} - F^{\uparrow}_{\mathrm{SW}} + F^{\downarrow}_{\mathrm{LW}} - F^{\uparrow}_{\mathrm{LW}} + Q - \mathrm{LHF} - \mathrm{SHF}. \tag{1.3}$$

Here, $\rho_w = 10^3$ kg m$^{-3}$ is the density of surface water, $C_w = 4.19\times10^3$ J kg$^{-1}$ K$^{-1}$ is the specific heat capacity of water, and $H_w$ is the depth of the ocean slab, which is chosen to be small ($H_w = 1$ m) to ensure fast equilibration of the model. SHF and LHF are the sensible and latent heat fluxes computed with the bulk aerodynamic formulas and Monin-Obukhov similarity theory. SHF is obtained from the specific entropy and LHF flux as described in Pressel et al. (2015). The parameter $Q$ represents a local energy gain by the slab ocean, either owing to seasonal uptake of energy or convergence of ocean energy transport (details in Section 1.3.1). The other terms are the upward and downward longwave (LW) and shortwave (SW) radiative fluxes at the surface obtained from the radiative transfer scheme.

### 1.2.4 Microphysics

To focus on the dynamical processes controlling clouds and boundary layers, we bracket off microphysical complexities inasmuch as possible (cf. Stevens and Bony, 2013). We employ a simple bulk closure for the microphysical processes of raindrop formation, which is similar in complexity as some common microphysics schemes used in GCMs (e.g., Sundqvist, 1988; Tiedtke, 1993). We assume that any cloud liquid water exceeding a liquid-water specific humidity threshold $q_{l,c}$ immediately rains out. This threshold $q_{l,c}$ is proportional to the saturation specific humidity $q_v^*$,

$$q_{l,c} = f_{\text{prec}} q_v^*. \tag{1.4}$$

Here we choose $f_{\text{prec}} = 0.1$. Under typical conditions of subtropical shallow cumulus ($T = 288$ K and $p = 850$ hPa), this formula gives $q_{l,c} = 1.2 \times 10^{-3}$ kg kg$^{-1}$, similar to the critical value of $10^{-3}$ kg kg$^{-1}$ as used in Sundqvist (1988). No re-evaporation of rain occurs in this simple microphysics scheme. We compare results using this simple microphysics schemes with those produced using the more complex warm-rain microphysics scheme of Seifert and Beheng (2006) in Section 1.5.

### 1.2.5 Large-scale forcing

Four large-scale forcing terms are included in the thermodynamic and water budgets: subsidence, relaxation toward a reference profile in the free troposphere, horizontal advection near the surface, and Coriolis accelerations owing to a prescribed geostrophic

wind.

#### 1.2.5.1 Subsidence

The subsidence tendencies are computed as

$$\left.\frac{d\phi}{dt}\right|_{\text{sub}} = -w_{\text{ls}}\frac{\partial\phi}{\partial z}, \tag{1.5}$$

where $\phi$ stands for any horizontal velocity component ($u$, $v$), specific entropy ($s$), or total water specific humidity ($q_t$). The large-scale subsidence velocity profile $w_{\text{ls}}$ is prescribed and time-independent.

#### 1.2.5.2 Relaxation toward reference profile

In the free troposphere, specific entropy $s$ and total water specific humidity $q_t$ (and thus temperature and moisture) are relaxed toward prescribed reference profiles to represent the combined effects of large-scale horizontal fluxes and vertical eddy fluxes,

$$\left.\frac{d\phi}{dt}\right|_{\text{rel}} = -\frac{\phi - \phi_r}{\tau(z)}. \tag{1.6}$$

Here, $\phi$ stands for $s$ or $q_t$, and the reference profile $\phi_r$ is representative of the location under consideration. In the climate change experiments to be discussed in Chapter 2, $\phi_r$ will be specified as a tropical radiative-convective equilibrium (RCE) temperature profile with a given relative humidity. In this chapter, because we are focusing on specific subtropical locations in the present climate, we use $\phi_r$ profiles

that are close to observations (details in Section 1.3.2). The relaxation time $\tau(z)$ varies continuously with height from very small values (strong relaxation) in the free troposphere to very large values (weak relaxation) in the boundary layer. Specifically, we set

$$\tau(z) = \tau_0 \left[1 - \exp(p/p_0 - 1)\right]^{-k}, \tag{1.7}$$

where $p_0 = 1000$ hPa is the mean surface pressure, and $\tau_0 = 2400$ s, $k = 2$. This formulation gives $\tau \approx 6$ h at 600 hPa (near the top of model domain), $\tau \approx 3$ d at 900 hPa (typically within the boundary layer), and $\tau \to \infty$ at the surface. That is, the relaxation toward the reference profile is very weak compared with typical dynamical adjustments within the boundary layer.

As is common, both a prescribed large-scale subsidence velocity $w_{\rm ls}$ and relaxation toward a reference profile are included to ensure that the free troposphere equilibrates to realistic conditions, without overly constraining features such as the boundary layer height by strongly relaxing toward reference profiles on which a boundary layer structure is already imprinted. Prescribing a subsidence velocity then becomes necessary to obtain a boundary-layer height than can equilibrate at levels below those at which the relaxation timescale becomes fast compared with dynamical adjustment timescales.

#### 1.2.5.3 Horizontal advection

Because the relaxation forcing effectively vanishes near the surface, large-scale fluxes near the surface need to be represented separately. We do so by prescribing horizontal advective tendencies at levels below 800 hPa. Advective tendencies are assumed to

be constant at levels below 900 hPa and linearly decrease to zero between 800 hPa and 900 hPa:

$$\left.\frac{d\phi}{dt}\right|_{\text{adv}} = \begin{cases} \dot{\phi}_s & \text{for} \quad p > 900 \text{ hPa}, \\ \dot{\phi}_s \cdot \frac{p - 800 \text{ hPa}}{900 \text{ hPa} - 800 \text{ hPa}} & \text{for} \quad 800 \text{ hPa} \leq p \leq 900 \text{ hPa}, \\ 0 & \text{for} \quad p < 800 \text{ hPa}. \end{cases} \tag{1.8}$$

Here, $\phi$ stands for temperature $T$ or total water specific humidity $q_t$. The tendency of specific entropy $s$ is then calculated from the tendencies of $T$ and $q_t$, as described in Pressel et al. (2015).

#### 1.2.5.4 Coriolis acceleration

Ageostrophic Coriolis accelerations are included in the horizontal momentum equations as

$$\left.\frac{du}{dt}\right|_{\text{cor}} = -f(v_g - v), \qquad \left.\frac{dv}{dt}\right|_{\text{cor}} = f(u_g - u), \tag{1.9}$$

where $f = 2\Omega \sin(\varphi)$ is the Coriolis parameter which depends on planetary rotation rate $\Omega$ and latitude $\varphi$, and $(u_g, v_g)$ is the prescribed geostrophic wind.

## 1.3 Representative subtropical MBL regimes

We test the forcing framework for the three locations representing prototypical regimes of subtropical MBL clouds that were considered in CGILS (Blossey et al., 2013): Sc (the S12 case), transitional Sc over Cu (the S11 case), and Cu (the S6 case). The

free-tropospheric reference profile $\phi_r$ and the ocean energy uptake $Q$ are taken from the climatological July conditions obtained as averages over the years 1979–2012 from ERA Interim reanalysis (Dee et al., 2011). They differ only slightly from the mean conditions for July 2003 that were used in CGILS.

### 1.3.1 Ocean energy uptake

The surface conditions of the three locations are shown in Table 1.1. The CGILS SHF and LHF data are computed from the mean of all LES model results in Tables 3, 4, and 5 of Blossey et al. (2013). The net surface radiative fluxes (RAD) were not reported in the CGILS study. We estimated them using an offline RRTMG calculation with CGILS reference profiles of temperature and moisture. A stratocumulus layer for the S12 and S11 cases and a cumulus layer (cloud fraction = 0.1) for the S6 case were added to the RRTMG calculation, where the liquid water content was assumed to increase linearly between the cloud-base heights ($z_b$) and the cloud-top heights ($z_i$), and the liquid water path (LWP) was set to match the reported CGILS values. The surface net radiative fluxes are then estimated as the sum of RRTMG cloudy net surface longwave (LW) flux and the clear-sky net surface shortwave (SW) flux, offset by the reported top-of-atmosphere (TOA) shortwave cloud radiative effect (SWCRE) in CGILS, which was scaled by an empirical factor of 1.1 to obtain surface SWCRE values. The direct net-flux output by offline RRTMG calculation is not used because of its significant biases for the cloudy SW fluxes, possibly related to the lack of spatial variations in cloud liquid water. The surface heat uptake (ocean cooling)

is then diagnosed on the basis of the surface energy balance, assuming that SST is stationary ($dT_s/dt = 0$).

The surface fluxes from ERA Interim are also shown in Table 1.1. The ERA Interim surface energy balance is very different from CGILS. Most significantly, the SWCRE may be much underestimated in ERA Interim for the S12 and S11 cases because the Sc cover is biased low in the reanalysis. Thus, the net surface heating by radiation may be overestimated, and the compensating ocean heat uptake is likely biased high. For the S6 case, although the net surface radiative flux agrees much better between ERA Interim and CGILS, their latent heat fluxes differ by over 20 W m$^{-2}$, and thus the difference between ocean heat uptake estimates is still large. While it may be argued that the CGILS results are preferred over reanalysis data because of their better representation of clouds and radiative effects, the spread of net surface radiative fluxes among different CGILS LES are still significant (e.g., $30 - 40$ W m$^{-2}$ for the S12 and S11 cases); thus the estimated ocean heat uptake would also differ as much.

Since no definite values of ocean heat uptake can be determined from either ERA Interim data or CGILS results, we have instead conducted a set of PyCLES experiments with fixed SST using our configuration of large-scale forcings to diagnose the ocean heat uptake required to maintain the SST. The diagnosed values are 60 W m$^{-2}$ for the S12 case, 85 W m$^{-2}$ for the S11 case, and 20 W m$^{-2}$ for the S6 case. These diagnosed heat uptake values differ from the CGILS study because of the differences in simulated cloud LWP, which affect the SWCRE strongly. Further details are provided

in Section 1.5.1.

| Case Name | LAT | LON | SST | SHF | LHF | RAD | QFLUX | INSOL |
|---|---|---|---|---|---|---|---|---|
| S12 (ERA-I) | 34.5 | −124.5 | 289.75 | 10.86 | 61.28 | −230.67 | 158.53 | N/A |
| S12 (CGILS) | 35 | −125 | 290.96 | 3.89 ±2.43 | 82.29 ±3.55 | −157 ±19 | 71 ±19 | 471.64 |
| S11 (ERA-I) | 31.5 | −129.0 | 292.22 | 14.90 | 85.58 | −207.43 | 106.96 | N/A |
| S11 (CGILS) | 32 | −129 | 292.46 | 4.30 ±0.54 | 97.83 ±2.56 | −139 ±17 | 37 ±17 | 470.26 |
| S6 (ERA-I) | 16.5 | −148.5 | 298.86 | 10.29 | 141.60 | −209.95 | 58.06 | N/A |
| S6 (CGILS) | 17 | −149 | 298.76 | 10.05 ±1.99 | 118.57 ±4.65 | −220 ±6 | 91 ±6 | 447.92 |

Table 1.1: The geographical locations and surface energy budgets of the three representative low-cloud cases (S12, S11, and S6), with comparisons between ERA-Interim climatology (ERA-I) and LES results of the CGILS intercomparison study (CGILS). The data fields are as follows: latitudes (LAT) and longitudes (LON) in degrees, sea-surface temperatures (SST) in Kelvin, surface energy budget terms including sensible heat flux (SHF), latent heat flux (LHF), net radiative flux (RAD), and ocean heat uptake (QFLUX) diagnosed as the residue. All energy fluxes are in $W/m^2$, and positive represents loss of energy for the surface. Thus, SHF, LHF, and QFLUX terms are positive, and RAD is negative. The CGILS mean results are reported with the standard deviation of all available models. The solar insolation values (i.e., top-of-atmosphere downward SW radiation) from CGILS cases are also listed (INSOL).

### 1.3.2 Large-scale forcings

The potential temperature ($\theta$) and relative humidity (RH) profiles from the ERA Interim climatology and from CGILS are compared in Figs. 1.1a and b. The $\theta$ and RH profiles are very similar between ERA Interim and CGILS. However, the CGILS boundary layer is slightly shallower in the S12 and S11 cases, so the free-tropospheric air just above the boundary layer top is warmer and drier. The free-tropospheric $\theta$ profiles are very similar between the S12, S11, and S6 cases, reflecting the weak temperature gradient (WTG) constraint in the tropics.

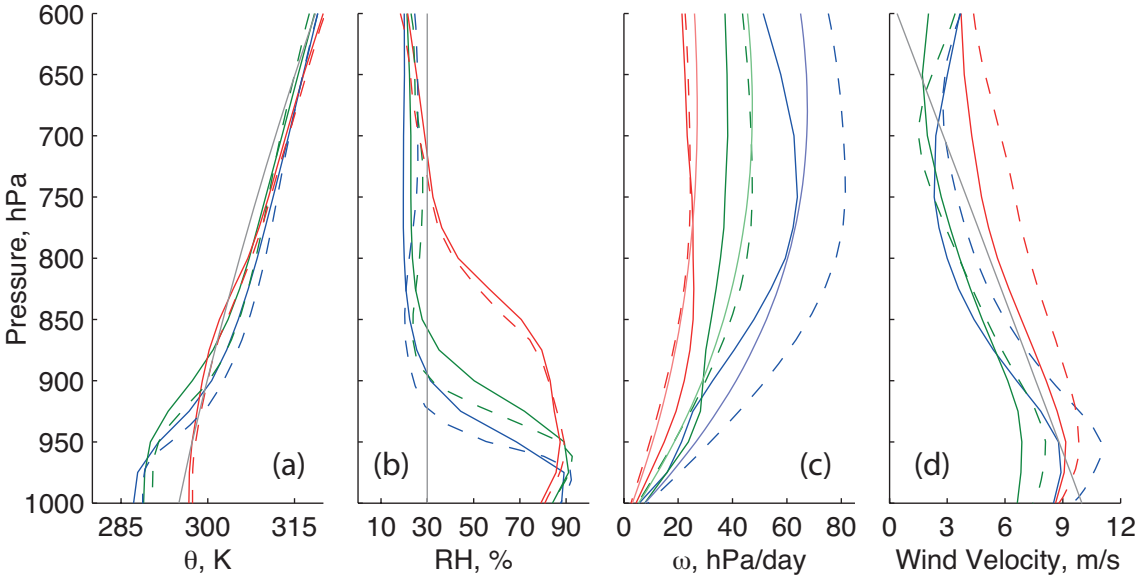


Figure 1.1: Comparison of potential temperature ($\theta$), relative humidity (RH), subsidence ($\omega$) and wind velocity profiles between ERA-Interim climatology (average July conditions for the years 1979-2012, solid lines) and the corresponding profiles used in the CGILS-LES experiment (dashed lines). Blue, green, and red lines represent the S12 (Sc), S11 (Sc-over-Cu), and S6 (Cu) cases, respectively. Grey lines represent the reference $\theta$, RH profiles and the prescribed geostrophic wind profile in the simulation, whereas light blue, light green and light red lines represent the prescribed subsidence rates.

These profiles are all close to the moist adiabat initialized from a saturated parcel at $p = 1000$ hPa, $T = 295$ K. Therefore, this adiabat is used as the reference temperature profile in our study. The free-tropospheric RH is around 25% for all cases, and the reference RH profile is set to be slightly higher at 30% to compensate for the subsidence drying. The reference profiles of specific entropy $s$ and total water specific humidity $q_t$ are computed accordingly. The reference profiles of $s$ and $q_t$ are defined throughout the atmospheric column, but they are only effective above $\sim 800$ hPa where relaxation is significant.

The large-scale subsidence profiles in pressure coordinates (denoted as $\omega$) are compared in Fig. 1.1c. The CGILS subsidence is stronger than the climatology for the S11 and S12 cases, consistent with the shallower boundary layers as seen in the $\theta$ and RH profiles. In our current study, the large-scale subsidence profiles are set to be of the form

$$\omega = -D(p_0 - p_s)(p_0/p_s)^2, \quad \text{and } w_{\text{ls}} = -\frac{\omega}{\rho_0 g}, \tag{1.10}$$

where $\rho_0$ and $p_0$ are the anelastic basic-state profiles of density and pressure. This formulation satisfies that $\partial\omega/\partial p = -D$ at the surface ($p_0 = p_s$), i.e., the surface-layer divergence rate is $D$, and that $\omega = 0$ when $p_0 = p_s$ or $p_0 = 0$. For the S12, S11, and S6 cases, $D$ is taken as $5 \times 10^{-6}$ s$^{-1}$, $3.5 \times 10^{-6}$ s$^{-1}$, $2 \times 10^{-6}$ s$^{-1}$, respectively. The resultant $\omega$ profiles are also shown in Fig. 1.1c, which are roughly consistent with the corresponding CGILS $\omega$ profiles, except for the S12 case in which our prescribed subsidence is weaker than in CGILS.

The wind velocity profiles are compared in Fig. 1.1d. The S12 and S11 wind

velocities decrease strongly from the surface layer into the free-troposphere, consistent with the strong thermal wind near the edge of the Hadley cell. The S6 wind velocity also decreases with height, albeit less strongly. In the current study, the prescribed geostrophic wind profile is chosen to be a linearly decreasing profile from 10 m $s^{-1}$ at the surface to 0 m $s^{-1}$ at $p_0 \approx 600$ hPa, and its direction does not change with height. This profile is similar to the wind velocity magnitudes in ERA Interim and CGILS.

Boundary layer horizontal advective tendencies are prescribed to be $\dot{T} = -1.2$ K $d^{-1}$ and $\dot{q}_t = -0.9 \times 10^{-3}$ kg $kg^{-1}$ $d^{-1}$. The advective tendencies are the same for all three cases. These values are similar to the values used in CGILS.

### 1.3.3 Experimental set-up

The simulations are run on a uniform grid, with horizontal resolution $\Delta x = \Delta y =$ 75 m and vertical resolution $\Delta z = 20$ m. The domain sizes are horizontally $L_x = L_y = 4800$ m and vertically $L_z = 4000$ m. The simulations are run for 20 simulated days, which takes about 4 days of real-time on 64 CPU cores.

For each of the S12, S11, and S6 cases, simulations are run both with fixed SST and with prescribed surface ocean heat uptake. The simulations are run with the RRTMG radiation scheme with the same TOA insolation values without diurnal cycle as in CGILS, and with the simple threshold precipitation scheme. Sensitivity tests on domain size, resolution, prescribed ocean heat uptake, and precipitation scheme are also conducted and will be discussed in Section 1.5.

## 1.4 Results

### 1.4.1 Rough simulation

To accelerate the convergence, a set of three rough simulations with $\Delta x = \Delta y = 100$ m, $\Delta z = 20$ m, $L_x = L_y = 3200$ m, fixed SST and the same large-scale forcings are run for 11 days, and the steady-state conditions of the respective cases are used as the initial condition of the high resolution simulations with evolving SSTs. The initial $\theta$ and RH profiles for these rough runs are the same as the reference profiles above 920 hPa, and the initial profiles below 920 hPa are set to be a vertically well-mixed layer with surface air temperature $T_a = 288$ K and RH = 80%. Therefore, a cloud-deck occurs between 950 hPa and 920 hPa initially. The initial wind profile is the same as the geostrophic wind. The surface pressure is $p_s = 1018$ hPa for all cases.

The time-height profiles of 6-hour mean cloud fraction from the fixed-SST rough simulations are shown in Fig. 1.2, and the evolution of LWP and the diagnosed surface heat uptake are shown in Fig. 1.3. Similar to the CGILS study, all three cases reach a statistically nearly steady state by Day 7. Fluctuations remain evident for the liquid water path and surface heat uptake, a result of the life cycles of the limited sample of turbulent eddies and clouds in the small domain. The S12 case develops a Sc layer between altitudes of 750 m and 950 m with LWP $\approx 40$ g m$^{-2}$; the S11 case grows from the Sc initial condition into the Sc-over-Cu regime, with Cu cloud bottom at 600 m and an Sc layer between 1270 m and 1420 m, with LWP $\approx 18$ g m$^{-2}$; the S6 case grows into a Cu layer with mean cloud cover $\sim 18\%$ and LWP $\approx 17$ g m$^{-2}$. The

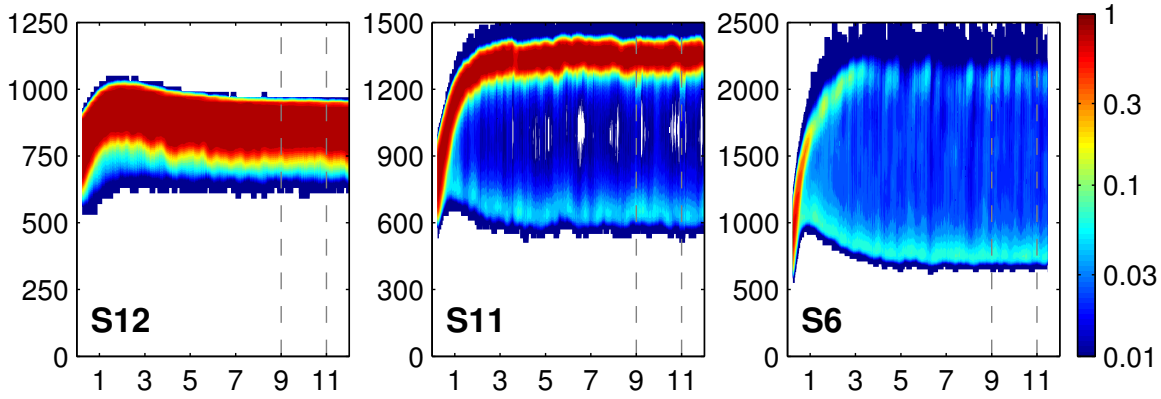


Figure 1.2: 6-hour mean cloud fractions from the rough simulations. Day 9-11 (marked by dashed lines) profiles are used as initial conditions for the high-resolution simulations.

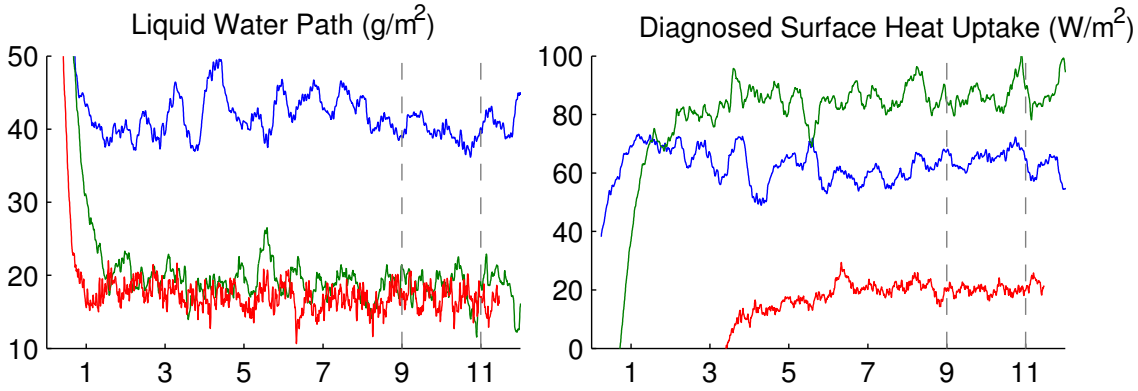


Figure 1.3: Timeseries (day) of the 6-hour mean liquid water path (left) and diagnosed surface heat uptake (right) from the rough simulations. Day 9-11 (marked by dashed lines) profiles are used as initial conditions for the high-resolution simulations.

Day 9-11 surface heat uptake values are diagnosed to be approximately 60 W $m^{-2}$ for S12, 85 W $m^{-2}$ for S11, and 20 W $m^{-2}$ for S6.

The Day 9-11 mean profiles of $\theta$, $RH$, $q_l$ and cloud fraction with the new forcing are shown in Fig. 1.4, in comparison with the Day 8-10 mean profiles of PyCLES simulations with the original CGILS forcing. The new forcing produces a deeper S12 boundary layer, due to the weaker subsidence compared to the original CGILS-S12 forcing, but it remains well-mixed with a single-peak profile of $\overline{w'w'}$. The S11 profiles are very similar, both with two peaks of cloud fraction and liquid water at the bottom of the Cu layer and at the Sc layer, and correspondingly a double peak structure of $\overline{w'w'}$. However, the Sc layer depth and the peak of $\overline{w'w'}$ in the Sc layer are both smaller than the reported values in CGILS study, possibly related to the rough resolution in the current study. The S6 Cu layer under the new forcing is shallower than that under the original forcing, since the relaxation height is much lower in the new forcing resulting in additional drying above 1500 m. Nevertheless, the total cloud fraction and LWP are almost unaffected by the difference in the Cu layer depth. The relaxation drying in the new S6 forcing is compensated by enhanced turbulent-convective moistening: the surface latent heat flux is 185 W $m^{-2}$ with the new forcing, compared to 120 W $m^{-2}$ with the original forcing. This is consistent with the enhanced $\overline{w'w'}$ in the boundary layer.

To test for the regime dependence on the initial condition, all three cases are rerun with the S12 (Sc) and S6 (Cu) steady state conditions as the initial states. The simulations all converge to the same steady state regardless of whether the initial

condition is cloudy or clear. Therefore, the fixed-SST steady state results are likely to be independent of initial conditions.

In summary, the new configuration of large-scale forcing is capable of representing the qualitative features of all three low-cloud regimes, although the relaxation may limit the vertical extent of S6 cumulus clouds within the lowest 2500 m, and the rough resolution may affect the qualitative LWP for the S11 Sc layer. Therefore, the steady state (Days 9-11) profiles will be used as the initial conditions of all higher-resolution runs, and the diagnosed surface heat uptake values are used for the fixed heat uptake experiments.

### 1.4.2 Control experiments: fixed SST vs. fixed surface heat uptake

Fig. 1.5 shows the evolution of cloud fields for the fixed-SST and fixed surface heat uptake experiments, and Fig. 1.6 shows the evolution of liquid water path, surface heat uptake (for fixed-SST experiments), and SST (for fixed heat uptake experiments).

Similar to the rough simulations, the fixed-SST experiments converge to steady state after only 3-5 days, although fluctuations still occur throughout the simulation period. The steady-state cloud fields are almost indistinguishable from the rough simulations. Compared to the rough simulations, the steady-state LWP is significantly higher for the S12 case, but slightly lower for the S11 and S6 cases. The steady-state surface heat imbalance is about $+9$ W m$^{-2}$ for the S11 case, $+2$ W m$^{-2}$ for the S6 case, and $-4$ W m$^{-2}$ for the S12 case. In other words, with the prescribed surface

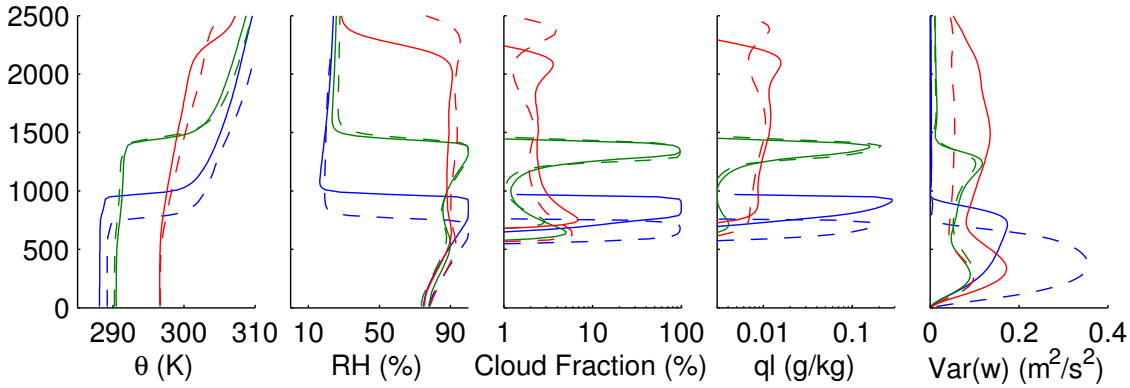


Figure 1.4: Steady-state profiles of potential temperature, relative humidity, cloud fraction, liquid water specific humidity, and resolved variance of vertical velocity. Solid lines are the Day 9-11 mean profiles from the rough simulations, and dashed lines are the Day 8-10 mean profiles from PyCLES simulations with original CGILS forcing. Blue, green, and red lines represent the S12 (Sc), S11 (Sc-over-Cu), and S6 (Cu) cases, respectively.

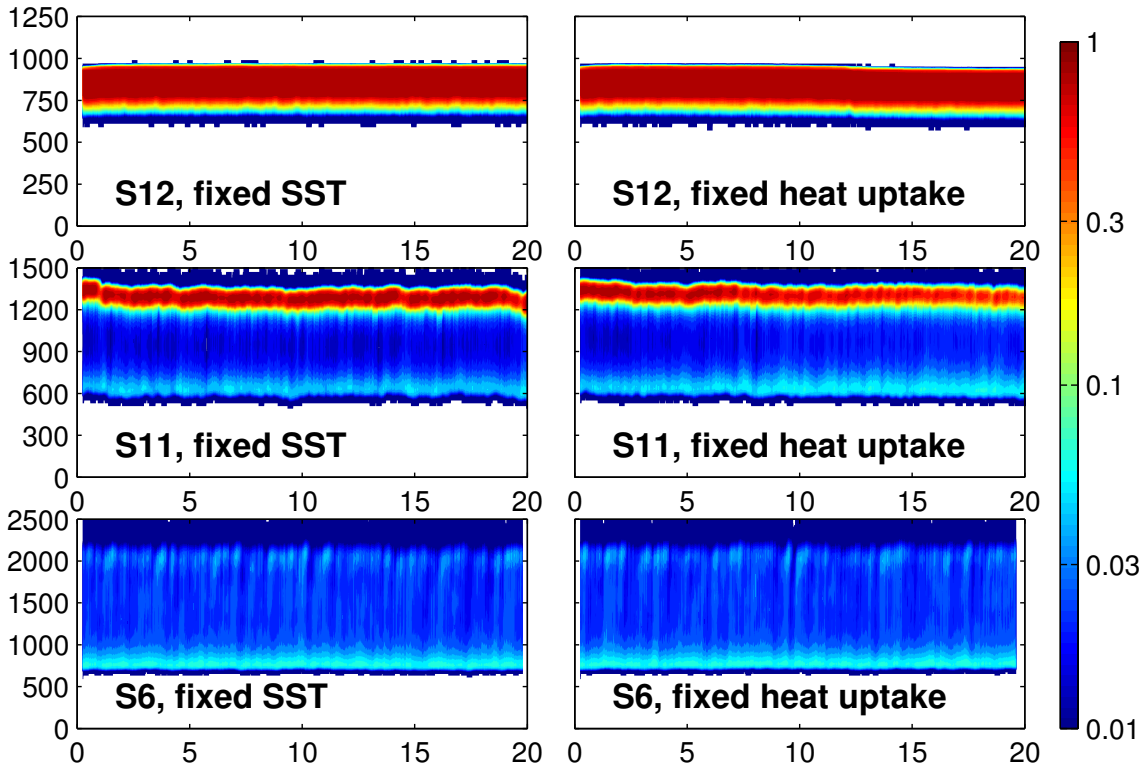


Figure 1.5: 6-hour mean cloud fractions from the control experiments with fixed SST (left column) and fixed surface heat uptake (right column).

heat uptake, we should expect a positive drift of SST for the S11 and S6 cases, and a negative drift for the S12 case.

The drift of SST in the fixed heat uptake experiments is consistent with our expectations. The SST drift in the S6 case is insignificant ($\sim$ 0.1 K), while SST decreases by $\sim -0.3$ K for the S12 case, and it increases by $\sim 1.5$ K over 20 days for the S11 case. From the evolution of the surface heat imbalance, we can see that the S6 and S12 cases both reach steady state after about 16 days, but the S11 case does not reach steady state even after 20 days (S11 seems to reach steady state after 25 days with SST drift of 1.8 K.) The increase of SST in the S11 case is accompanied by a decrease of LWP and cloud cover, i.e., the Sc layer becomes less liquid-abundant but the Cu fraction increases. However, the cloud layer depth does not change.

Fig. 1.7 shows the Day 16-20 mean profiles of both experiments. The S6 and S12 profiles are very similar, except that the peak of $q_l$ at the Cu detrainment layer is less pronounced in the control experiment, contributing to the lower LWP. This is even more significant for the S11 case, in which the control experiments (with a larger horizontal domain and higher horizontal resolution) simulate a Sc layer that is less abundant in liquid water, and the cloud-top entrainment is thus weaker, resulting in a shallower boundary layer. The cloud SW cooling effect weakens correspondingly, which can feedback onto SST if surface heat uptake is prescribed.

In summary, the prescribed surface heat uptake experiments reach steady states similar to the fixed-SST experiments for the S6 and S12 cases, but the S11 experiment does not stabilize due to the cloud SW feedback accompanying the Sc-Cu transition.

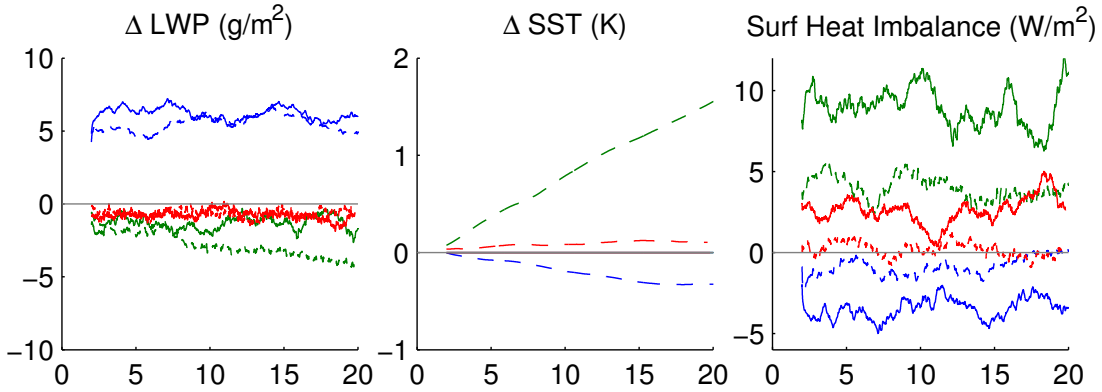


Figure 1.6: The 2-day mean timeseries of control experiments with fixed SST (solid) and fixed surface heat uptake (dashed). The left panel shows the LWP difference from the rough simulations; the middle panel shows the departure from the initial SST; the right panel shows the surface energy imbalance with the prescribed surface heat uptake (positive means net gain of energy). Blue, green and red lines represent the S12 (Sc), S11 (Sc-over-Cu), and S6 (Cu) cases, respectively.

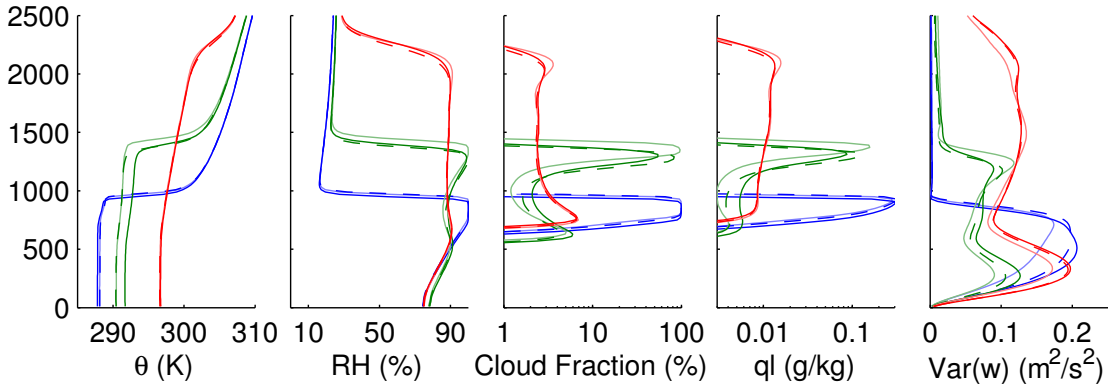


Figure 1.7: Mean profiles as in Figure 1.4, but for Days 16-20 of control experiments with fixed surface heat uptake (solid) and with fixed SST (dashed). All simulations are in steady state, except for the S11 case with prescribed surface heat uptake (green solid curves). The light solid curves are steady-state profiles from the rough experiment.

The sensitivity of the steady state conditions to the prescribed surface heat uptake will be further discussed in the next subsection.

## 1.5 Sensitivity studies

### 1.5.1 Ocean energy uptake

In this experiment, we perturb the prescribed surface heat uptake by $\pm 20$ W m$^{-2}$, and compare the simulation results with the control experiments. The evolution of cloud fields is shown in Fig. 1.8, and the evolution of liquid water path and SST are shown in Fig. 1.9. The Day 16-20 mean profiles are shown in Fig. 1.10.

The response of S6 case to the perturbation is almost linear. For both $+20$ W m$^{-2}$ and $-20$ W m$^{-2}$ perturbations, the SST reaches steady state after about 12 days, which changes by $-0.9$ K and $+1.0$ K compared with the initial SST, respectively. The LWP with both perturbations does not differ much from the control run, but the inversion height, the LCL height and the boundary layer turbulence kinetic energy (as indicated by $\overline{w'w'}$) all decrease with enhanced surface heat uptake (and lower SST). This is consistent with the decreased surface sensible and latent heat fluxes. The cloud fraction at the top of Cu layer increases with enhanced heat uptake, consistent with the strengthened inversion. The cloud fraction and $q_l$ in the middle of the Cu layer are almost unchanged with the perturbation.

The S12 $+20$ W m$^{-2}$ case maintains the Sc layer and reaches steady state after 10 days. The steady state SST is 0.9 K lower than the S12 control case, and the

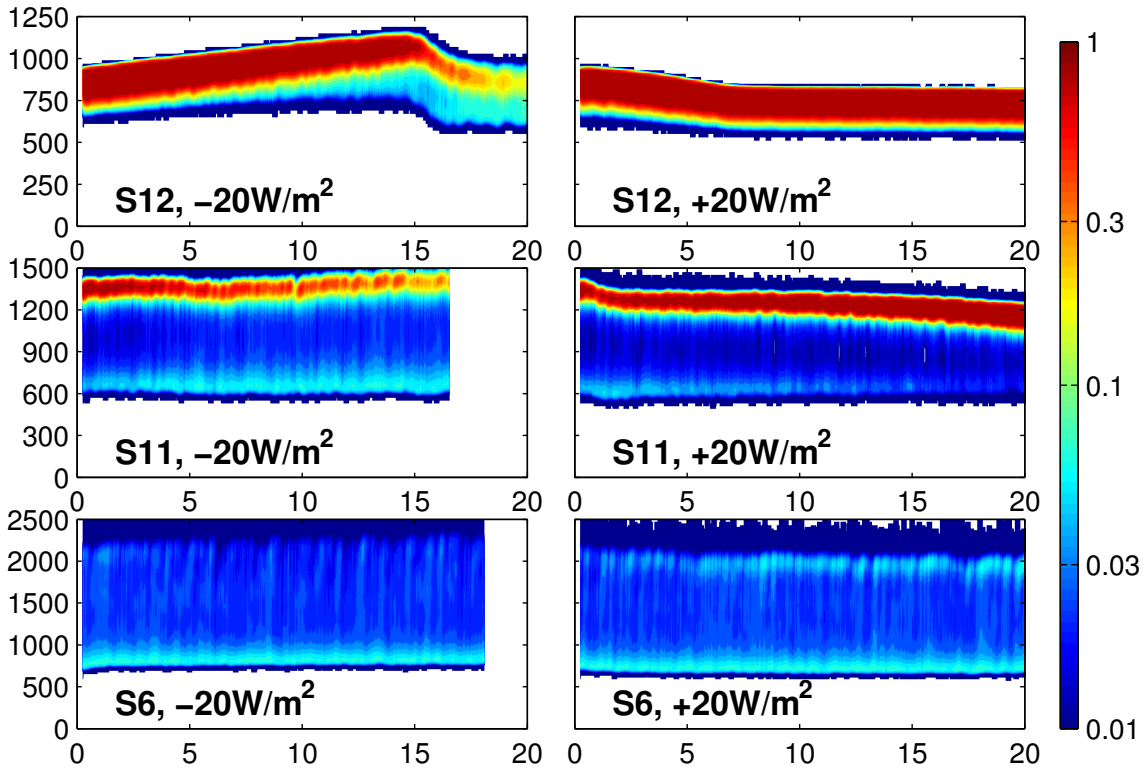


Figure 1.8: Similar to Figure 1.5, but with perturbed surface heat uptake: $-20$ W m$^{-2}$ (left column), and $+20$ W m$^{-2}$ (right column).

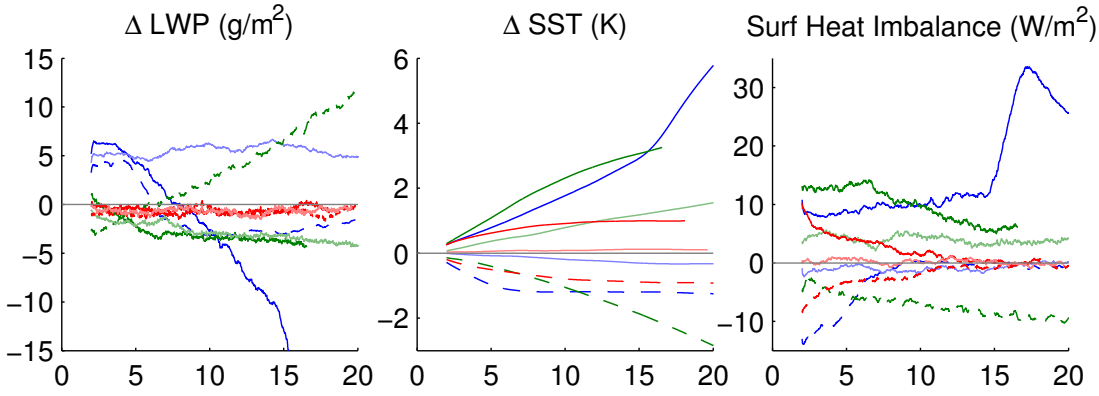


Figure 1.9: Similar to Figure 1.6, but with perturbed surface heat uptake: $-20$ W m$^{-2}$ (solid), $+20$ W m$^{-2}$ (dashed), and control (light colors).

Sc layer shifts down by $\sim$ 100 m. With lower mixed-layer $\theta$ and $q_t$, LWP is slightly lower by $\sim$ 6 g m$^{-2}$. In contrast, the S12 $-20$ W m$^{-2}$ case fails to reach steady state after 20 days. The Sc layer grows higher with increasing SST, but the LWP decreases continuously and cloud SW cooling weakens, which helps to maintain the surface energy imbalance. At Day 15 with a 3 K increase of SST, the Sc layer collapses, the cloud SW cooling greatly weakens, and the SST starts to increase more rapidly. With an extended run, the S12 $-20$ W m$^{-2}$ case finally reaches steady state at $\sim$ Day 30, in a shallow Cu regime with cloud top at 1200 m, SST at 298 K (i.e., an SST increase of 8 K), and LWP = 8 g m$^{-2}$.

For the S11 cases, none of the simulations reach steady state after 20 days. In the S11 $+20$ W m$^{-2}$ case, SST decreases by 3 K by Day 20, and the boundary layer correspondingly gets shallower and Sc becomes thicker, indicative of the early stage of transition from the Sc-over-Cu regime into the well-mixed Sc regime. In the S11 $-20$ W m$^{-2}$ case, SST increases by 3.5 K, and the boundary layer deepens while the Sc layer becomes more broken with cloud fraction $\sim$ 30%. Compared to the Day 20 condition of the control simulation, the LWP is 16 g m$^{-2}$ higher in the $+20$ W m$^{-2}$ case but only 1 g m$^{-2}$ lower in the $-20$ W m$^{-2}$ case.

The S11 cases (especially the $+20$ W m$^{-2}$ case) and the S12 $-20$ W m$^{-2}$ case are indicative of a strong positive cloud feedback that results in a regime transition. To understand this phenomenon, we write the steady-state energy budget of the boundary layer and the surface, i.e.,

$$Q_s - \overline{\rho} H \dot{m}_{adv} - \frac{\omega}{g}\big[L(q_+ - q_m) + c_p(\theta_+ - \theta_m)\big] - \frac{\overline{\rho} H}{\tau}\big[L(q_{ref} - q_m) + c_p(\theta_{ref} - \theta_m)\big]$$
$$= (1-\alpha)F_{SW}^{\downarrow} + F_{LW}^{\downarrow} - F_{LW}^{\uparrow}, \tag{1.11}$$

where $Q_s$ is the surface heat uptake; $H$ is the depth of boundary layer; $\dot{m}_{adv}$ is the advective tendency of moist static energy; $\omega$ is the bulk subsidence rate, which is equal to the subsidence rate at inversion if boundary layer is well-mixed; $\tau$ is the bulk relaxation timescale dependent on the height of boundary layer; $\phi_+, \phi_m, \phi_{ref}$ are the free tropospheric, boundary layer and reference conditions; $\alpha$ is the total albedo of the boundary layer and the surface; $F_{SW}^{\downarrow}$ is the downward SW flux at the top of boundary layer; and $F_{LW}^{\downarrow}, F_{LW}^{\uparrow}$ are downward and upward LW fluxes at the top of boundary layer.

Now assume that for the same large-scale forcing configuration, the steady state solution of each fixed SST corresponds to a value of ocean heat uptake, i.e., $Q_s = Q_s(T_s)$. The invertibility of this function depends on its monotonicity. If this function is monotonic, i.e., $dQ_s/dT_s < 0$ (higher ocean heat uptake corresponds to lower SST generally), then it can be inverted as a single-valued function $T_s = T_s(Q_s)$, which dictates the steady state SST given the ocean heat flux. However, if this function is non-monotonic, $Q_s$ may not be a single-valued function of $T_s$, and some solution of $Q_s(T_s)$ may be unstable if locally $dQ_s/dT_s > 0$. In other words, if some feedback process is able to increase the bulk energy gain when SST increases, (and, consistently, the required surface heat uptake for equilibration), it will lead to local

runaway feedback that shifts SST further away from the initial state.

For further illustration, we may take the derivative of equation (1.11) with respect to $T_s$, i.e.,

$$\begin{aligned}
&\frac{dQ_s}{dT_s} - \overline{\rho}\frac{dH}{dT_s}\dot{m}_{adv} + (\frac{\omega}{g} + \frac{\overline{\rho}H}{\tau})\left(L\frac{dq_m}{dT_s} + c_p\frac{d\theta_m}{dT_s}\right) \\
&- \frac{dH}{dT_s}\left[\frac{1}{g}\frac{d\omega}{dH}\big[L(q_+ - q_m) + c_p(\theta_+ - \theta_m)\big] + \frac{d(\overline{\rho}H/\tau)}{dH}\big[L(q_{ref} - q_m) + c_p(\theta_{ref} - \theta_m)\big]\right] \\
&= -\frac{d\alpha}{dT_s}F^{\downarrow}_{SW} - \frac{dF^{\uparrow}_{LW}}{dT_s}. \qquad (1.12)
\end{aligned}$$

Note that we have assumed $\omega, \rho, \tau$ are all functions of $H$ only (i.e., the feedback of SST on the large-scale circulation is neglected for now), $\dot{m}_{adv}$ is constant, and that $F^{\downarrow}_{LW}$ and $F^{\downarrow}_{SW}$ are also constant. Thus the corresponding terms are omitted.

Generally for the CGILS conditions, the horizontal advection cools and dries the boundary layer, thus $\dot{m}_{adv} < 0$. The subsidence $\omega$ and relaxation factor $1/\tau$ both increase with height, thus $d\omega/dH > 0$ and $d(\overline{\rho}H/\tau)/dH > 0$. Therefore, the bracketed term in the second line of the equation is positive if subsidence/relaxation warming dominates, and negative if drying dominates. Apart from these boundary layer height-dependent terms, the last term in the first line (subsidence/relaxation feedback) is clearly positive, and the term $dF^{\uparrow}_{LW}/dT_s$ (LW feedback) is also positive, since the outgoing LW radiation from boundary layer top increases with boundary layer emission temperature which generally increase with $T_s$. Note that we are considering the bulk budget including the surface, and thus the cloud LW effect is much less significant than in the boundary layer budget.

The last remaining term is the cloud SW feedback term $(d\alpha/dT_s)F_{SW}^{\downarrow}$. As SST increases, the boundary layer regime generally transitions from Sc to Cu, and thus $d\alpha/dT_s$ can be strongly negative during the transition, contributing to positive $dQ_s/dT_s$. In contrast, the subsidence/relaxation and LW feedback terms both contribute to negative $dQ_s/dT_s$. Therefore, with the prescribed surface heat uptake, the cloud SW feedback may locally run away in the transitional regime, leading to a bifurcation into either the Sc regime or the Cu regime (possibly with anvil).

To verify this idea, we have rerun the S11 rough simulations with perturbed fixed SST and diagnosed the steady-state surface heat uptake, and the result $Q_s(T_s)$ is shown in Fig. 1.11. As in the above discussion, SST increase is accompanied by a strong decrease of LWP, especially between $T_s = 287$ K and 292 K. The cloud SW feedback locally dominates the $Q_s(T_s)$ function, causing $dQ_s/dT_s > 0$ locally. Multiple solutions of $T_s$ thus arise with some specific value of $Q_s$. For example, for $Q_s = 85$ W m$^{-2}$, three solutions occur at about 283 K, 291 K, and 295 K. The solutions $T_s = 283$ K and 295 K are stable, corresponding to Sc and Cu (with anvil) regimes, respectively. The solution $T_s = 291$ K (transitional Sc regime) is unstable, and a slight perturbation will shift it further away. Also, a perturbation of $Q_s$ by $+20$ W m$^{-2}$ will shift the $T_s = 295$ K Cu-solution all the way down to about 282 K with transition to Sc regime, while a perturbation by $-20$ W m$^{-2}$ will shift the $T_s = 283$ K Sc-solution to the Cu regime. These phenomena are similar to the cloud evolutions in the S11 $+20$ W m$^{-2}$ and S12 $-20$ W m$^{-2}$ simulations.

In summary, the prescribed ocean heat uptake experiments can reach steady state

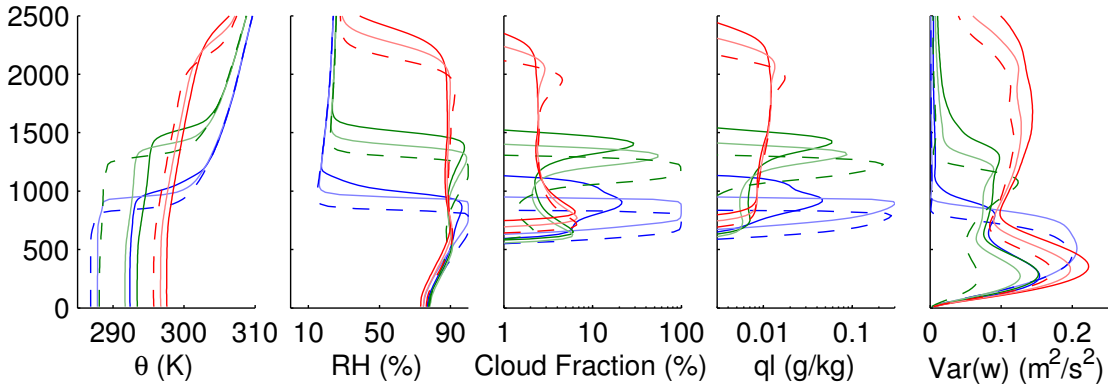


Figure 1.10: Similar to Figure 1.7, but with perturbed surface heat uptake: $-20$ W m$^{-2}$ (solid), $+20$ W m$^{-2}$ (dashed), and control (light colors). All simulations are in steady state, except for the S11 cases (green) and the S12 $-20$ W m$^{-2}$ case (blue solid).

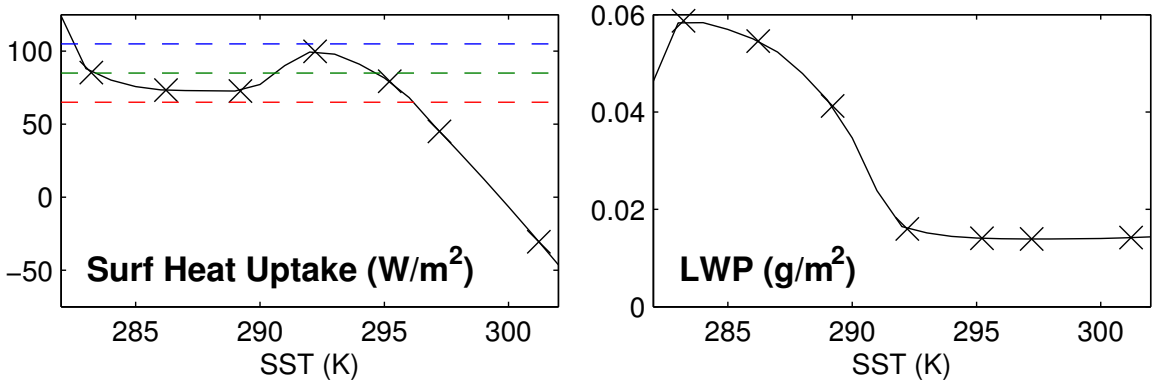


Figure 1.11: Bifurcation phenomenon demonstrated by rough S11 simulations with perturbed fixed SST. The surface heat uptake $Q_s$ and LWP are plotted as functions of SST. The green, blue and red dashed lines correspond to the surface heat uptake values of control, $-20$ W m$^{-2}$, and $+20$ W m$^{-2}$ simulations.

in about 15 days in the pure Sc and Cu regimes (S6, S12 control, and S12 +20 W $m^{-2}$ cases), where cloud SW feedback is insignificant. They correspond to the high-end and low-end values of $Q_s$, respectively. For cases with intermediate $Q_s$, the steady state may not be unique, and a perturbation of $Q_s$ may result in transition between Sc and Cu regimes.

### 1.5.2 Domain size and resolution

To test the sensitivity of model results on the domain configuration, we have run fixed-SST simulations on different domain sizes of $L = 3.2$ km, 6.4 km, and 9.6 km, with proportionally changing horizontal resolution (i.e., $\Delta x, \Delta y = 50$ m, 100 m, and 150 m, respectively) and uniform vertical resolution $\Delta z = 20$ m. The S12 and S6 cases are qualitatively insensitive to the choice of domain size, although quantitative differences occurs. The S12 steady state LWP increases slightly with domain size (41.5 g $m^{-2}$ for $L = 3.2$ km compared to 49.5 g $m^{-2}$ for $L = 9.6$ km), and the implied surface heat uptake differs by 8 W $m^{-2}$. The S6 steady state LWP decreases slightly with domain size (17.5 g $m^{-2}$ for $L = 3.2$ km compared to 14.9 g $m^{-2}$ for $L = 9.6$ km), and the inferred surface heat uptake differs by 9 W $m^{-2}$. The vertical structures of S6 and S12 cloud layers are very similar, except that the cumulus fraction is higher with a more pronounced detrainment peak in the 3.2-km domain.

The steady-state regime for the S11 transitional case, however, is sensitive to the choice of domain size. Domains smaller than $L = 4.8$ km are able to maintain the Sc-over-Cu structure, while in larger domains the Sc layer collapses and the boundary

layer transitions into a shallow Cu regime. The left column of Fig. 1.12 shows the evolution of cloud fields over the first 8 days after initialization from a cloudy initial condition. The initial boundary layer growth is similar for all cases until Day 1.5, when the Sc layers in larger domains start to dry up and collapse. It takes more than 8 days for both 6.4 km and 9.6 km cases to reach the new steady state. By Day 8, the largest domain simulation has lost half its LWP compared to the smallest domain (9.3 g $m^{-2}$ compared to 17.6 g $m^{-2}$), resulting in an increased surface heating imbalance of 41.5 W $m^{-2}$. This would lead to a significant increase of SST if surface heat uptake were prescribed instead of SST.

This sensitivity is due to the domain size, not the horizontal resolution, as revealed by two additional tests: one doubles $\Delta x$ in the 3.2-km domain, and the other halves $\Delta x$ in the 6.4-km domain. The results are shown in the right column of Fig. 1.12. For the 3.2-km domain, doubling $\Delta x$ does not affect the evolution and steady state of the Sc-over-Cu layer. For the 6.4-km domain, refining $\Delta x$ helps to maintain a Sc layer with cloud fraction of $\sim 75\%$ up to Day 7, but the LWP and inversion height are still lower than in the 3.2-km simulation with the same $\Delta x$. These two resolution tests are also performed with the S6 and S12 cases, and no significant sensitivity is observed.

Finally, we have tested a rougher vertical resolution $\Delta z = 40$ m on the 6.4-km domain. The S11 Sc layer collapses quickly, similar to the simulation with $\Delta z = 20$ m on the 9.6-km domain. The S6 simulation is insensitive to the change in vertical resolution, but the S12 case is somewhat sensitive: the Sc layer lowers by about

100 m with LWP significantly reduced to 27 g $m^{-2}$. This is consistent with the CGILS study, in which the sensitivity of S12 and S11 cases to the vertical resolution necessitates the choice of $\Delta z = 5$ m. Due to computational constraints, we have not tested our configuration at such high vertical resolution, but we have found that the choice of $\Delta z = 20$ m is sufficient for realistically representing the three cloud regimes with our advective schemes (which differ from those used in CGILS models), and will thus be used throughout this study.

In summary, the S6 Cu-case is insensitive to horizontal and vertical resolution, but is slightly sensitive to the domain size. The S11 and S12 cases are sensitive to the vertical resolution, where $\Delta z = 20$ m seems to be the minimum required resolution to maintain a realistic Sc layer. The S11 case is additionally sensitive to the domain size: transition into the Cu regime may occur with domain size $L \geq 6.4$ km. For reference, the S11 case in the CGILS study is run on a $L = 4.8$ km domain. It will be interesting to test whether this transitional regime will still be stable in a larger domain, or whether it will bifurcate into either of the Sc and Cu regimes.

### 1.5.3 Precipitation scheme

In the fixed surface heat uptake experiments with threshold precipitation scheme, the precipitation rates are diagnosed to be less than 0.01 mm $d^{-1}$ for S12 case, 0.08 mm $d^{-1}$ for S11 case, and 0.7 mm $d^{-1}$ for S6 case. To test the model sensitivity to precipitation scheme, we have rerun all three cases with the warm-rain scheme of Seifert and Beheng (2006). As expected, the S12 steady state is not affected by

the choice of precipitation scheme, consistent with its negligible precipitation. The S11 case shows further reduced precipitation with the warm-rain case: the surface precipitation rate decreases from 0.08 mm $d^{-1}$ to less than 0.01 mm $d^{-1}$. The LWP is 5% higher and the inversion height is about 50 m higher with the Seifert-Beheng scheme. The surface energy imbalance still leads to an increasing SST and a gradual decay of the Sc layer, but the transition is slower than with threshold precipitation.

The most significant difference occurs with the S6 case, which is shown in Fig. 1.13. With the threshold microphysics scheme, precipitation starts above 1500 m and is comparatively strong. As illustrated in Blossey et al. (2013), precipitation reduces the liquid water in the cumulus-top entrainment layer, which corresponds to reductions of the entrainment rate and the inversion height. The precipitation with the Seifert-Beheng scheme is much weaker and occurs a slightly higher levels (above 1800 m). This leads to an increase of inversion height by 300 m and higher liquid water content at the entrainment layer, and the column LWP increases from 17 g $m^{-2}$ to 21 g $m^{-2}$. The diagnosed precipitation rate is only 0.1 mm $d^{-1}$ with the warm-rain scheme, but this is due to the growth of cumulus into levels with significant large-scale relaxation, where it dominates over the precipitation scheme. The energetic analysis shows that the drying and warming effects by large-scale relaxation are $15-20$ W $m^{-2}$ stronger with the Seifert-Beheng scheme, which exactly compensates the decreased drying/heating by precipitation. This shows that the default relaxation may be too strong and may interfere with other processes for the S6 cumulus case, which will be further tested in the following subsection.

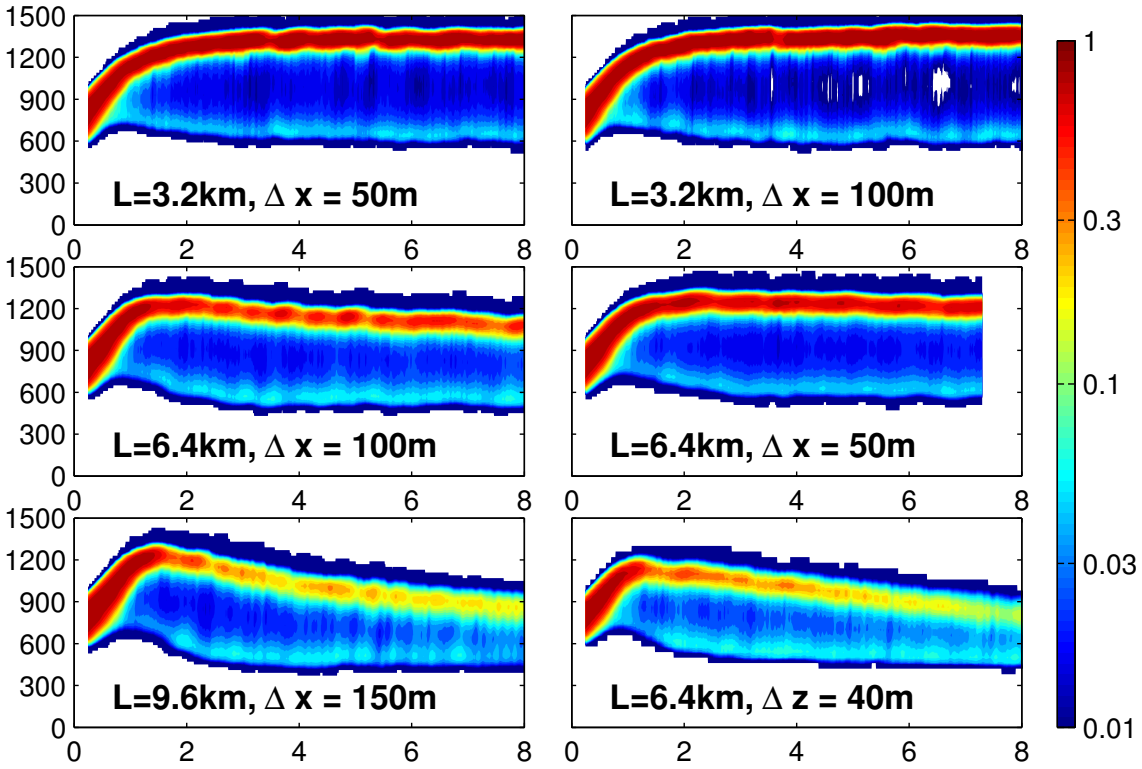


Figure 1.12: Similar to Figure 1.5, but for S11 fixed SST sensitivity tests for domain size and resolution. The default size and resolution are in this set of tests are $\Delta x =$ 100 m, $\Delta z = 20$ m, $L = 6.4$ km.

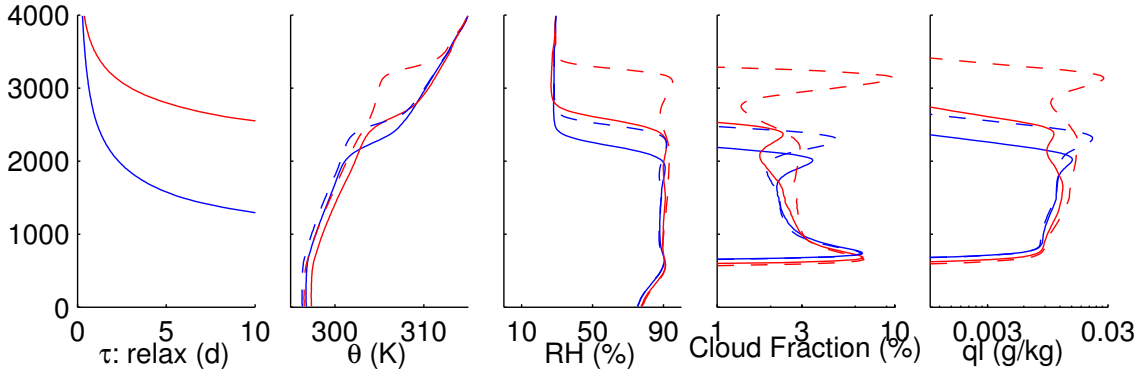


Figure 1.13: Similar to Figure 1.7, but with S6 sensitivity tests on precipitation schemes and relaxation profiles. The relaxation timescales of default (blue) and reduced (red) configurations are shown as the left figure. Solid lines represent threshold precipitation scheme, and dashed lines represent warm rain scheme. Results are taken from mean-profiles of Days 5-6.

In summary, the S12 and S11 cases are comparatively insensitive to the choice of precipitation scheme, but the threshold scheme produces stronger precipitation in the S6 case compared to the Seifert-Beheng scheme, which corresponds to reduced entrainment, inversion height, and liquid water at entrainment level. The effect of precipitation scheme on the cloud fractions in the lower part of S6 cumulus layer (i.e., below 1500 m) is negligible.

### 1.5.4 Large-scale relaxation profile

In the default simulations, the large-scale relaxation forcing becomes significant above 1800 m, which is well above the boundary layers of the S12 (Sc) regime and S11 (Sc-over-Cu) regime. However, the S6 Cu layer grows into the relaxation layer, where relaxation exerts an additional drying and warming analogous to enhanced subsidence. To test the sensitivity of the S6 Cu layer to the relaxation forcing, we have rerun the fixed flux simulations with reduced relaxation. The parameters in equation (1.7) are changed to $\tau_0 = 0.2$ s, $k = 10$, and the profile of the new relaxation timescale $\tau$ is plotted in comparison to the default profile in Fig. 1.13. As the relaxation is now disabled below 2500 m, Cu layers with both the threshold and Seifert-Beheng schemes grow deeper. The reduced relaxation drying/warming is mostly compensated by strengthened precipitation with the threshold scheme, in which the precipitation rate increases to 1.32 mm $d^{-1}$. However, the Seifert-Beheng scheme adjusts less sensitively to the changed forcing, with which the precipitation rate only increases to 0.4 mm $d^{-1}$. The unrestrained entrainment causes the Cu layer to grow up to 3300 m

where both relaxation and subsidence provide the required drying and warming, and the peak of cloud fraction is significant just below the inversion. With both precipitation schemes, the enhanced latent heating contributes to the slight increase of boundary layer temperature, but the changes of cloud fraction and liquid water in the lower Cu layer are again much weaker compared to changes at cloud top.

## 1.6 Discussion and conclusion

In this study, we have configured a forcing framework for the simulation of three subtropical boundary layer cloud regimes: Sc, Sc-over-Cu, and shallow Cu. Instead of fixing SST or fixing surface fluxes, this configuration couples the atmosphere with a slab ocean layer and prescribes the ocean heat uptake, so that surface energy budget is realistically closed at steady state. Three components of large-scale atmospheric forcing are formulated: the large-scale subsidence, the relaxation towards the tropical moist adiabat in the free troposphere, and the horizontal advective cooling and drying in the lower troposphere. The model is coupled to the RRTMG radiation scheme and microphysics schemes.

We have tested three cases with forcings representative of summer-time subtropical marine boundary layer conditions that are similar to the S12, S11 and S6 cases in the CGILS study. All three low-cloud regimes are simulated with ocean heat uptake of respectively 60 W $m^{-2}$ (S12, Cu), 85 W $m^{-2}$ (S11, Sc-over-Cu) and 20 W $m^{-2}$ (S6, Cu), and the results are similar to the fixed-SST results. It takes longer for the fixed ocean heat uptake cases to reach a steady state (about 10 days for S6 and S12 cases,

and $> 20$ days for S11 case), and the stabilization timescale depends on the strength of stabilizing feedbacks to SST perturbation, mostly by subsidence drying and LW cooling.

The S6 cumulus case is insensitive to perturbations of ocean heat uptake due to its weak SW cloud feedback, but the S11 and S12 cases are sensitive to ocean heat uptake perturbation of $\pm 20$ W m$^{-2}$, which may result in a shift between Sc and Cu steady states. The multiple steady states are related to the strong positive SW feedback during the Sc-Cu transition, where a positive perturbation of SST reduces the cloud LWP and albedo, increases the SW heating of the coupled system of the boundary layer and the ocean mixed-layer, which is not sufficiently compensated by the stabilizing effects of increased subsidence drying and LW cooling. Thus the system is unstable to SST perturbations and will continue to shift towards warmer or cooler states until $d$LWP$/d$SST becomes small (i.e., destabilizing SW cloud feedback is weak), such as in the Sc and Cu regimes.

We notice that this bifurcation phenomenon and the two final steady states of Sc and Cu are similar to the results by Bretherton et al. (2010) (the latter regime is referred to 'decoupled shallow patchy clouds' by the authors). The configurations of their study differed from our experiments, more significantly in that the SST was fixed in their study and radiation was nocturnal, and thus the destabilizing feedback was provided by the cloud-top LW-cooling effect acting on the boundary layer, instead of the cloud SW-albedo effect acting on the combined system in our study. Both feedbacks depend sensitively on the LWP, and thus the cloud regimes in both studies

converge to either Sc or shallow Cu regimes in which the cloud feedbacks are much less sensitive on LWP. Our study also agrees with Bretherton et al. (2010) in that the bifurcation does not require precipitation processes, and that the convergence towards the final steady state can be slow ($>$ 10 days), especially if the initial state is close to the bifurcation point. This implies that low clouds might not be in steady state, if the cloud regime is near the Sc-Cu transition and the large-scale synoptic forcing changes faster than the convergence timescale. Including representations for time-varying large-scale forcing in the LES may be important for such situations (e.g., the winter-time subtropics which is affected by the intrusion of mid-latitude synoptic systems). This also implies that the cloud regime under transitional conditions is dependent on its history, thus the representation of past conditions may be important for turbulence-convection parameterizations in climate models.

Apart from the bifurcation phenomenon, the S11 transitional regime is also the most susceptible to the choice of resolution and domain size. The Sc layer is better maintained with higher horizontal and vertical resolutions, which has been consistently reported by various previous studies such as Bretherton et al. (1999), Stevens et al. (2005), Cheng et al. (2010), and Blossey et al. (2013). However, the break-up of Sc layer may also be more favorable with a larger horizontal domain, even with the same resolution. Especially, the Sc layer starts to collapse when domain size exceeds 6.4km, which is slightly larger than the CGILE-LES S11 domain size of 4.8km. The dynamical explanation for this domain size dependence is unclear and will be investigated in a future study.

The natural extension of the current study will be to investigate the climate change response of low cloud regimes within the same forcing framework. This will be the main topic of Chapter 2. In the current framework, the SST under climate change is jointly determined by the direct radiative effect of increased $CO_2$ concentrations, the shifted free-tropospheric conditions due to the change of radiative-convective equilibrium profile in the deep tropics induced by increased $CO_2$, and the boundary layer processes in the LES. The SST is thus internal to the coupled system and is solved interactively, rather than being prescribed a priori. The surface energy budget is closed, and the changes of surface fluxes (e.g., the sub-Clausius-Clapeyron scaling of latent heat flux increase, and the surface buoyancy flux decrease) are more comparable to what happens in climate models. Such an energetic constraint is strongly violated if the subtropical SST is simply prescribed to increase as much as in the deep tropics. We will show that the response of Cu regime to warming differs significantly under these two scenarios.

# Chapter 2

# Large-eddy simulation of subtropical cloud-topped boundary layers. Part II: Constraints on the cumulus response to climate change

## 2.1 Introduction

Uncertainties about the climate change response of subtropical boundary layer clouds are the major contributors to uncertainties in climate change projections. Large-eddy simulations (LES) have been successful in reproducing the observed features of current-day boundary layer clouds, and they have been used to study the cloud responses to idealized changes in large-scale conditions. Some recent LES studies have investigated the response of shallow cumulus (Cu) clouds to perturbed sea surface temperature (SST) and free tropospheric conditions (Bellon and Stevens, 2012; Rieck et al., 2012), the parameter dependence of the Cu layer to surface fluxes and lower-tropospheric divergence (Schalkwijk et al., 2013), the steady states and

climate-change responses of stratocumulus (Sc) layers with different estimated inversion strength (EIS) and inversion moisture jump (Gesso et al., 2014; van der Dussen et al., 2015), the steady-state transition from Sc to Cu with gradually increasing SST (Chung et al., 2012), and the climate-change response of the non-equilibrium Sc-Cu transition process (Bretherton and Blossey, 2014). The CGILS LES intercomparison project (Blossey et al., 2013) includes an idealized experiment on the response of Sc, Sc-over-Cu, and Cu boundary layer regimes (S12, S11, and S6 cases, respectively) to a 2 K increase of SST, accompanied by a commensurate increase of free-tropospheric temperature and decrease of subsidence. Starting from the CGILS-LES study, a set of extended LES experiments has been designed to investigate the cloud responses to the individual factors (Bretherton et al., 2013). These studies have explored a vast parameter space of different cloud regimes, and they have been useful in providing theoretical insights to the cloud response mechanisms, and in helping to validate simpler models under shifted climate conditions, such as mixed-layer models (MLM) and simplified cumulus models.

For most of the idealized LES experiments, the large-scale conditions are characterized by the following idealized assumptions: (a) the change of SST is prescribed and fixed; (b) the change in radiative parameters (e.g., $CO_2$ concentration) is separately prescribed and may not be energetically consistent with the SST change; (c) the upper-tropospheric temperature profile is also prescribed separately, usually assumed to be the tropical moist adiabat under the same SST change. Under these assumptions, the energy budgets of the atmospheric column and the surface ocean

mixed-layer are not closed. The implied oceanic and atmospheric energy transports may need to change unrealistically to compensate for the energetic imbalance. As discussed in Chapter 1, the fixed-SST formulation may lead to surface latent heat flux (LHF) to increase with Clausius-Clapeyron scaling that exceeds the constraint by surface energy budget, resulting in an over-convective boundary layer after warming. Additionally, the subtropical boundary layer is effective in longwave (LW) cooling due to the dryness aloft, and the local climate sensitivity may be lower than the tropical value. This contrast in LW cooling efficiency has been discussed by Pierrehumbert (1995). The CMIP models also tend to simulate weaker warming in the subtropics compared to the deep tropics. Thus, the assumption that the free troposphere will warm as much as the surface may also be invalid. For a more realistic representation of climate change, the large-scale forcing in the LES simulations should be set up in an energetically consistent way. This motivates the current study on developing a forcing framework for LES with explicit energetic constraints.

In Chapter 1, we have presented an energetically consistent forcing framework for LES of subtropical low clouds, in which the LES domain is coupled to a slab ocean with prescribed surface heat uptake and interactive SST, and the energy budget is closed at equilibrium. The upper troposphere is relaxed to a representative tropical moist adiabat and the subsidence and boundary layer horizontal advection are prescribed. With large-scale forcing comparable to the ERA-Interim July climatology of the GCSS Pacific Cross-Section (Teixeira et al., 2011), the current day low-cloud regimes of Sc (S12), Sc-over-Cu (S11), and Cu (S6) layers are well sim-

ulated and are qualitatively comparable to the CGILS-LES study, which uses the fixed-SST approach. In this chapter, an extension of this study to idealized climate change scenarios is presented, in which multiple simulations of the perturbed Cu (S6) condition are run with different $CO_2$ concentrations and correspondingly altered upper-tropospheric conditions while the ocean heat uptake is held constant. These fixed heat uptake experiments are compared to a set of conventional fixed-SST experiments. The most significant difference with fixed heat uptake is that SST increases less in the subtropics than in the deep tropics due to the weaker water vapor feedback. This is responsible for the shallowing of the Cu-topped boundary layer, accompanied by a decreased liquid water path (LWP) and a positive cloud SW feedback. The fixed-SST experiments instead show a huge increase in surface LHF and a deepening Cu layer similar to Rieck et al. (2012). The current focus is on the Cu case only, and a companion study on the climate response of Sc-over-Cu and Sc regimes will be undertaken as a natural extension of this work.

This chapter is organized as follows: Section 2.2 briefly reviews the LES forcing framework and describes the configurations of climate change experiments. Section 2.3 briefly discusses the sensitivity of LES results to the precipitation scheme. Section 2.4 presents the main results of how different components of the cumulus layer respond to climate change. These results under the fixed surface heat uptake assumption are compared with the fixed-SST results, and the mechanisms of the responses are discussed. Section 2.5 summarizes the conclusions of the current study. Section 2.6 is an appendix describing the algorithm that is used to calculate the tropical radiative-

convective equilibrium (RCE) profiles.

## 2.2 Description of climate-change experiments

### 2.2.1 Forcing framework

The numerics of the PyCLES code and the formulations of large-scale forcing and boundary condition have been described in detail in Chapter 1. Briefly, the large-scale forcing includes three components: the large-scale subsidence, the boundary layer horizontal advection, and the large-scale relaxation. The large-scale subsidence velocity is formulated as a prescribed lower-tropospheric divergence rate multiplied by a fixed profile of subsidence that maximizes at around 700 hPa (i.e. 3000 m), and the subsidence warming and drying are computed interactively. The boundary layer horizontal advective tendencies of temperature and moisture are prescribed and are constant below 900 hPa, zero above 800 hPa, and linear in between. The large-scale relaxation represents the combined effect of the departure of mean advection from the idealized formulations of subsidence and horizontal advection, and the time-average effects of transient advection. It is represented by a Newtonian relaxation towards the tropical radiative-convective equilibrium temperature profile with prescribed relative humidity, and the relaxation timescale is on the order of 6 hours at 600 hPa and tends to infinity at the surface. The LES is coupled to a mixed-layer ocean with SST subject to the energy budget equation, and the ocean heat uptake is prescribed. The RRTMG radiation scheme (Iacono et al., 2008) and a simple threshold microphysics scheme

are used to compute tendencies due to the radiation and precipitation processes.

### 2.2.2 Large-scale forcing

#### 2.2.2.1 Reference profiles

In this study, the simulated warming is driven by a change of $CO_2$ concentration, while the other well-mixed greenhouse gases are assumed to remain unchanged. The reference temperature profile is assumed to be the equatorial radiative convective equilibrium (RCE) profiles with surface temperature corresponding to a tropical equilibrium climate sensitivity (ECS) of 4 K per doubling of $CO_2$. The reference relative humidity is assumed to be the same as the present condition: 30% below the tropopause, and decrease from 1% just above the tropopause to 0% at the top of the atmosphere. The detailed algorithm of the RCE calculation with RRTMG is described in the Appendix (i.e., Section 2.6).

Alternatively to prescribing a fixed equatorial SST increase with doubling $CO_2$, it is also possible to prescribe the combined atmospheric/oceanic energy export from the equatorial column and determine the temperature. However, we find that if the energy export is fixed at its present value, the equatorial ECS will increase with $CO_2$ concentration and transition into a run-away greenhouse at $2.5 \times CO_2$, due to the water-vapor feedback associated with the high relative humidity in the convecting region. In reality, the magnitude of energy export depends on both thermodynamics and the large-scale dynamics that both change with climate. Due to the complexity and uncertainty of these mechanisms, the assumption of a fixed ECS seems to be

simpler and preferable. The energy budget of the equatorial column corresponding to the 4 K ECS is summarized in Table 2.1. The required total energy export to maintain the 4 K ECS is diagnosed to vary from about 50 W $m^{-2}$ for 0.25× and 1.0 × $CO_2$, to 65 W $m^{-2}$ for 16.0 × $CO_2$.

Table 2.1: The equatorial surface energy budget from the offline calculation of climate sensitivity, assuming that the ECS for the surface air temperature is 4 K, the surface RH is 80%, and the bulk transfer coefficient is $C_D\|U\| = 5 \times 10^{-3}$ m $s^{-1}$. Two sets of calculations are performed assuming that the ocean heat uptake is 0 W $m^{-2}$ and 50 W $m^{-2}$, respectively. The data fields are as follows: $CO_2$ concentration relative to the default value of 287 ppm ($CO_2$), sea-surface temperatures (SST), and surface air temperature (TA) in Kelvin, surface energy budget terms including sensible heat flux (SHF), latent heat flux (LHF), net longwave (LW) and shortwave (SW) radiative fluxes, and ocean heat uptake (QFLUX). All energy fluxes are in W $m^{-2}$, and positive represents loss of energy for the surface. Thus, SHF, LHF, LW, and QFLUX are positive, and SW is negative. The total energy loss (LOSS), i.e., the sum of atmospheric and ocean heat export, is also shown in positive numbers. Note that the surface net SW flux does not depend on the partitioning of total heat export.

| $CO_2$ | QFLUX | SST | TA | SHF | LHF | LW | SW | LOSS |
|---|---|---|---|---|---|---|---|---|
| 0.25× | 0 | 294.33 | 289.75 | 27.58 | 92.42 | 112.59 | -232.59 | 48.51 |
| | 50 | 292.33 | | 15.50 | 65.42 | 101.67 | | 51.27 |
| 1.0× | 0 | 301.21 | 297.75 | 20.21 | 117.17 | 86.13 | -223.51 | 48.70 |
| | 50 | 299.57 | | 10.63 | 86.34 | 76.53 | | 50.17 |
| 4.0× | 0 | 308.19 | 305.75 | 13.79 | 144.98 | 55.45 | -214.22 | 53.56 |
| | 50 | 306.86 | | 6.28 | 110.84 | 47.10 | | 54.11 |
| 16.0× | 0 | 315.06 | 313.75 | 7.17 | 168.05 | 29.54 | -204.77 | 64.51 |
| | 50 | 313.98 | | 1.25 | 131.25 | 22.26 | | 64.62 |

#### 2.2.2.2 Subsidence and horizontal advection

An offline diagnosis of temperature tendencies is performed to determine the change in subsidence rate. The result shows that, if the upper-tropospheric radiative cooling is assumed to exactly balance the subsidence warming, the subsidence rate should decrease by about 40% per doubling $CO_2$ around default conditions, and stay almost

constant for $CO_2$ concentrations higher than $4\times$ the default value. However, the diagnosed subsidence rate for the default condition is much smaller than the actual value based on the ERA-Interim climatology. This indicates that the cooling by horizontal advection is very important for the subtropical low-cloud regions, and the subsidence rates cannot be constrained by the radiative cooling alone. Therefore, due to the same concern for the uncertainty in the circulation dynamics, we have opted to keep using the same default subsidence profile for perturbed climates. Consistently, the geostrophic wind profile is also assumed to be unchanged.

For better agreement of surface LHF values between the LES results and the ERA-Interim climatology, the horizontal advective drying tendency for the S6 cumulus case is reduced to 40% of the value presented in Chapter 1 (i.e., $\dot{q}_t = -0.36 \times 10^{-3}$ kg kg$^{-1}$ d$^{-1}$). Under climate change, the horizontal advective tendencies are assumed to take the same profile shapes as the default condition. The advective drying is assumed to scale with the Clausius-Clapeyron relation (i.e., the drying tendency increases by 6% K$^{-1}$, or by about 25% per doubling $CO_2$ according to the assumed tropical ECS), and the advective cooling is assumed to be unchanged.

The assumption underlying these simplifications is that the horizontal temperature gradient and the strength of the tropical overturning circulation do not change much with climate, and thus the subsidence rate and horizontal wind profiles are also unchanged. Further tests will be designed to investigate the sensitivity of low-cloud responses to changes in large-scale tropical circulation, such as by multiplying the subsidence, horizontal advection, and geostrophic wind profiles by a scaling parame-

ter that characterizes the circulation strength relative to the current condition, and by scaling the temperature and moisture gradients in the calculation of advective tendencies interactively with the LES solution, but these are beyond the scope of the current study.

#### 2.2.2.3 Interactive relaxation

The relaxation timescale in the free troposphere is assumed to be the same (6 hours) for all cases. However, the boundary layer depth may depend on the cloud regime and change with climate, so an interactive profile of relaxation is formulated instead of the fixed profile as formulated in Chapter 1. For every step, the boundary layer height $h$ is determined to be the lowest layer that satisfies the inequality:

$$q_t(h) \leq \alpha q_{t,r}(h), \tag{2.1}$$

where $q_t$ is the horizontal mean of total water specific humidity, and $q_{t,r}$ is the reference profile. This formulation works well for the subtropical cloud-topped boundary layers, in which the $q_t$-jump is strong at the inversion. The value $h$ is insensitive to the threshold ratio $\alpha$ as long as $1 < \alpha < 2$, and in the current study $\alpha = 1.2$ is used. The profile of relaxation coefficient $\xi_r(z)$ depends on $h$ as follows, similar to the original

CGILS-study (Blossey et al., 2013):

$$\xi_r(z) = \begin{cases} 0 & \text{for} \quad z/h < 1.2, \\ 0.5\tau_r^{-1}\left[1 - \cos\left(\frac{z/h-1.2}{1.5-1.2}\right)\right] & \text{for} \quad 1.2 \leq z/h \leq 1.5, \\ \tau_r^{-1} & \text{for} \quad z/h > 1.5. \end{cases} \tag{2.2}$$

And the relaxation tendencies for $\phi$ (specific entropy $s$ and total water specific humidity $q_t$) are determined as:

$$\left.\frac{d\phi}{dt}\right|_{\text{rel}} = -\xi_r(z)(\phi - \phi_r). \tag{2.3}$$

The results of the default simulations are insensitive to the change of the formulation of relaxation coefficient.

### 2.2.3 Microphysics

It has been shown previously that the S6 case is weakly precipitating, and the depth of the cumulus layer is dependent on the microphysics scheme. Thus multiple simulations are run with different microphysics schemes, including the Seifert-Beheng warm-rain scheme (Seifert and Beheng, 2001, 2006; Stevens and Seifert, 2008), the warm-rain component of the Grabowski mixed-phase scheme (Grabowski, 1998), and the simple threshold precipitation scheme with threshold values at 2%, 10% and 20%.

### 2.2.4 Case studies

For each of the microphysics scheme, simulations are run with 4 levels of $CO_2$ concentrations: 0.25×, 1.0× (default), 4.0× and 16.0× the default $CO_2$ volume mixing ratio of 287 ppm. The prescribed surface heat uptake is increased to 65 W $m^{-2}$ compared to Chapter 1, consistent with the decreased surface LHF due to reduced horizontal advective drying. This value is also closer to the ERA-Interim climatology (58 W $m^{-2}$). Due to computation constraints, the simulations are run on coarser resolutions than the control study: the horizontal and vertical resolutions are $\Delta x = 100$ m, $\Delta z = 40$ m for the S6 case. Simulations with such rough resolutions have been shown in Chapter 1 to produce qualitatively similar results to the higher-resolution control experiments. The horizontal domain size is $L_x = 4.8$ km and the vertical domain size is $L_z = 6.4$ km. Due to computational constraints, all simulations are run on 64 cores for 1 day of wall time ($\sim$ 5-7 days of model time), and are then restarted twice from the final conditions of the previous day. This roughly corresponds to 20 days of simulation for S6 cases with simple threshold microphysics, and 15 days of simulation with more sophisticated microphysics. For comparison with the previous studies, we have also run fixed-SST simulations with the same numerical configurations and large-scale forcing formulations. The SST in these simulations are also assumed to change by 4 K per doubling $CO_2$, which means that the SST gradient between the deep tropics and the subtropics is assumed to be unchanged in these fixed-SST experiments.

## 2.3 Sensitivity to the precipitation scheme

Fig. 2.1 shows the steady-state potential temperature, relative humidity, cloud fraction, and liquid water specific humidity profiles from the S6 fixed surface heat uptake experiments (solid lines), in comparison with results from corresponding fixed-SST experiments (dashed lines). Results of the five different precipitation schemes are all shown.

The steady state Cu layer profiles are strongly dependent on the choice of microphysics scheme. This phenomenon has been discussed in Blossey et al. (2013) and Chapter 1 of this thesis: a microphysics scheme with higher precipitation efficiency reduces the upward total water flux, allowing less liquid water to reach the cloud-top entrainment layer. Thus, the turbulent mixing weakens with reduced LW radiative and evaporative cooling. The reduced entrainment rate contributes to the sink of the Cu layer top. This effect is most clearly demonstrated in the fixed-SST experiments with the simple threshold precipitation scheme: compared to the default 10%-threshold, the Cu layer top is about 900 m higher with the 20%-threshold, and about 1000 m lower with the 2%-threshold. Similar tendencies also occur in the fixed surface heat uptake simulations, except for the warm cases with high precipitation thresholds, in which precipitation efficiencies are all too low to affect the entrainment rates. The difference in Cu layer depths between Grabowski and Seifert-Beheng schemes can also be explained similarly, for which the former precipitates more efficiently and entrains less strongly at cloud top.

The weak precipitation of threshold schemes in warmer climate is related to their

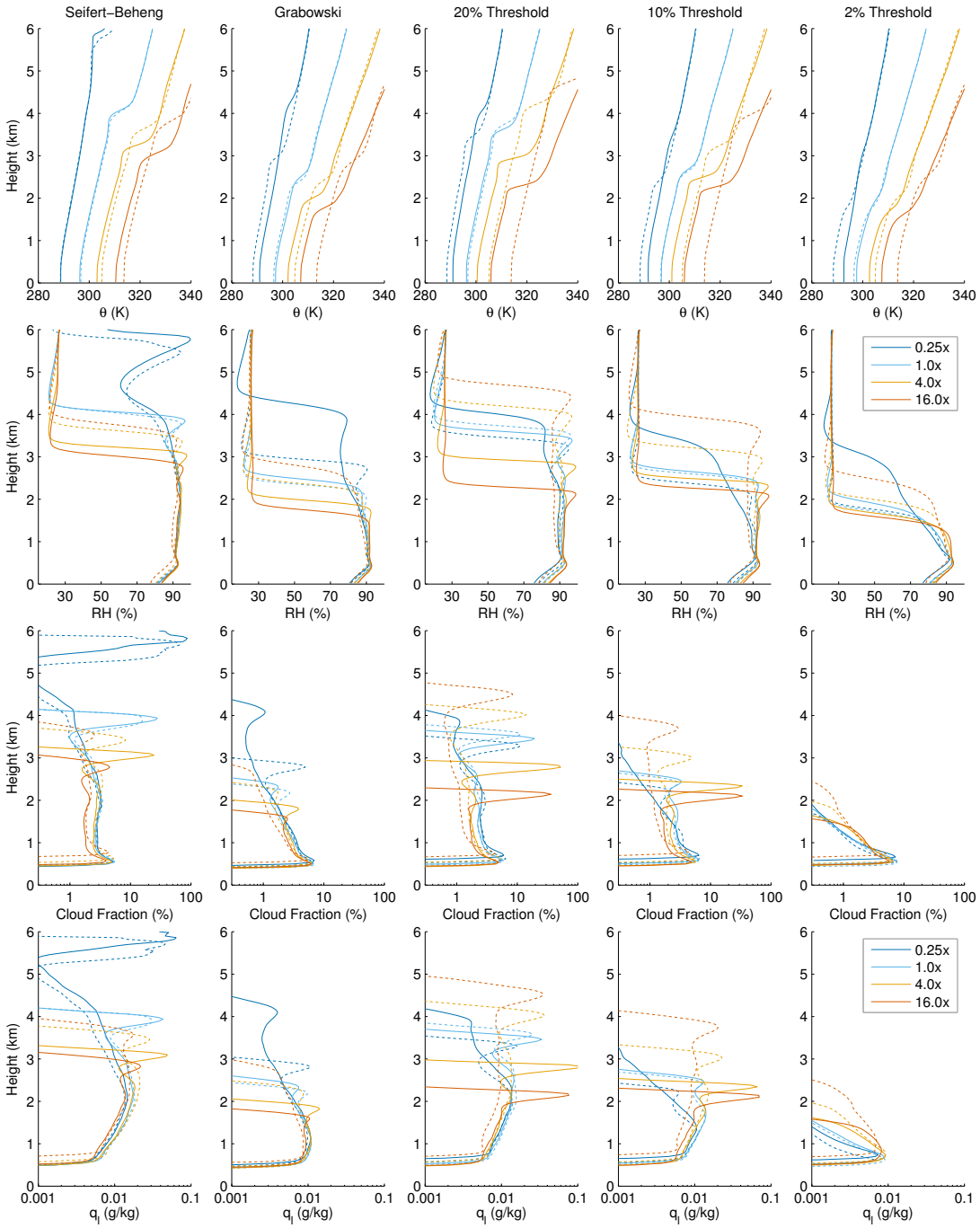


Figure 2.1: The steady-state potential temperature, relative humidity, cloud fraction and liquid water specific humidity profiles of S6 cases with 0.25× (Dark Blue), 1.0× (Light Blue), 4.0× (Orange), and 16.0× (Red) the default $CO_2$ concentrations. Solid lines represent fixed surface heat uptake simulations; dashed lines represent fixed-SST simulations.

Clausius-Clapeyron scaling of the precipitation threshold, which means that precipitation onsets at higher $q_l$ in warmer conditions. For the almost non-precipitating cases (10%- and 20%-threshold for 4.0× and 16.0 × $CO_2$), the liquid water transported by cumulus updrafts is trapped below the inversion layer, appearing as an anvil layer with peak cloud fractions $> 30\%$. This effect is less significant in the fixed-SST experiments, for which the inversion peak of cloud fractions are all lower than 15%. In contrast, the warm-rain schemes don't have explicit cut-off thresholds of precipitation onset, and the cloud morphology differs less significantly between cooler and warmer climate. The Cu layer depths with Grabowski scheme are roughly comparable to those of 15%- and 5%- threshold schemes, respectively, for the coldest and warmest cases of fixed surface heat uptake experiments, and all cases show a weak peak of cloud fraction ($< 5\%$) at the inversion. The Seifert-Beheng scheme precipitates less and is closer to the 20%-threshold. It also fails to precipitate sufficiently in the coldest climate, resulting in an excessively deep Cu layer with an anvil layer with almost 100% cloud cover. This problem may be resolved by including the compatible mixed-phase precipitation scheme as in Seifert and Beheng (2006).

Despite the sensitivity to the precipitation scheme, some phenomena are found to occur robustly with all different microphysics schemes. These phenomena are constrained by the energetic coupling between the surface, the boundary layer, and the free-troposphere, and they are modulated by the dynamical and radiative processes related to turbulence and clouds. These phenomena will be identified in the next subsection, and some mechanistic explanations will be provided subsequently.

## 2.4 Robust cumulus layer responses to warming

### 2.4.1 Reduced subtropical climate sensitivity

The temperature profiles in Fig. 2.1 show that the simulated subtropical local climate sensitivity is much lower in the fixed surface heat uptake experiments, compared to the prescribed change in SST. The steady state SST only increases by about 2 to 2.5 K per doubling $CO_2$, which is much smaller than the assumed tropical ECS. The only exceptions are the Seifert-Beheng simulations, in which the break-up of cold-case anvil layer leads to positive cloud SW feedback, enhancing the SST increase to $> 3$ K per doubling $CO_2$.

The analyses of surface energy budget are shown Table 2.2 and 2.3 for both sets of LES experiments. Compared to the offline equatorial RCE results (Table 2.1), the subtropical LHF is much stronger, but the surface temperature jump is smaller and the surface RH is similar. This is a result of the strong trade wind that enhances the subtropical surface fluxes: the subtropical surface bulk transfer coefficient is diagnosed to be about twice the equatorial value.

The major difference between the two sets of subtropical simulations is found to be the change of surface LHF. In the fixed-SST experiments, the surface energy budget is unconstrained. Thus, the LHF increases exponentially with the Clausius-Clapeyron relation. The surface RH remains almost unchanged, or even decreases slightly with extreme warming. Comparing the $4\times$ and $1 \times CO_2$ cases, the strong increase of LHF by $\sim 60$ W m$^{-2}$ is found to be balanced mostly by the reduced

Table 2.2: Mean and 1× standard deviation of steady-state surface energy budget from fixed-SST experiments with the 5 microphysics schemes (Seifert-Beheng, Grabowski, simple threshold of 20%, 10%, and 2%). SST is assumed to increase by 4 K for doubling $CO_2$. The data fields are the same as Table 2.1, except that QFLUX now represents the required surface energy sink to maintaining the SST, which is not prescribed but diagnosed from the residue of the surface energy budget. The relative humidity (RH) at the surface layer is also presented.

| $CO_2$ | SST | TA | RH | SHF | LHF | LW | SW | QFLUX |
|---|---|---|---|---|---|---|---|---|
| 0.25× | 290.83 | 290.05 | 80.18 | 9.48 | 91.42 | 75.47 | −271.83 | 95.46 |
| | (fixed) | ±0.14 | ±1.37 | ±1.84 | ±5.58 | ±11.48 | ±35.71 | ±19.08 |
| 1.00× | 298.86 | 298.22 | 81.99 | 7.67 | 131.32 | 55.65 | −268.82 | 74.18 |
| | (fixed) | ±0.11 | ±1.04 | ±1.40 | ±3.56 | ±6.09 | ±17.33 | ±13.83 |
| 4.00× | 306.90 | 306.58 | 81.67 | 3.77 | 193.87 | 32.30 | −261.02 | 31.07 |
| | (fixed) | ±0.15 | ±1.07 | ±1.79 | ±7.94 | ±2.98 | ±11.79 | ±15.33 |
| 16.00× | 314.94 | 315.27 | 78.73 | −3.49 | 285.36 | 14.28 | −256.57 | −39.58 |
| | (fixed) | ±0.18 | ±1.68 | ±1.90 | ±14.52 | ±0.83 | ±7.17 | ±18.11 |

Table 2.3: The same as Table 2.2, but for the prescribed surface flux experiments. QFLUX is prescribed in these cases, and small residues of less than 5 W $m^{-2}$ are present in the surface energy budget.

| $CO_2$ | SST | TA | RH | SHF | LHF | LW | SW | QFLUX |
|---|---|---|---|---|---|---|---|---|
| 0.25× | 293.43 | 292.58 | 78.44 | 10.41 | 118.21 | 72.39 | −267.65 | 65.00 |
| | ±1.62 | ±1.47 | ±3.22 | ±3.15 | ±24.77 | ±10.67 | ±41.30 | (fixed) |
| 1.00× | 299.18 | 298.53 | 81.53 | 7.70 | 137.67 | 54.66 | −267.76 | 65.00 |
| | ±0.87 | ±0.77 | ±1.29 | ±1.67 | ±10.85 | ±4.96 | ±17.86 | (fixed) |
| 4.00× | 303.73 | 303.35 | 83.70 | 4.37 | 148.05 | 36.68 | −255.46 | 65.00 |
| | ±1.08 | ±1.00 | ±0.70 | ±1.61 | ±13.57 | ±4.27 | ±18.65 | (fixed) |
| 16.00× | 308.77 | 308.70 | 84.49 | 0.72 | 168.39 | 22.50 | −255.79 | 65.00 |
| | ±1.31 | ±1.36 | ±0.51 | ±1.49 | ±12.29 | ±2.80 | ±12.84 | (fixed) |

ocean heat uptake (40 W $m^{-2}$), and partly by the the weakened LW cooling due to water vapor feedback (20 W $m^{-2}$). In contrast, the change of LHF is constrained by the surface energy budget in the fixed surface heat uptake experiments. With the fixed surface heat uptake, the increase of LHF can only be balanced by the modest changes in the net LW and SW radiation at the surface, and the SHF change is small compared to LHF because of the high Bowen ratio. Therefore, it increases much less strongly than the Clausius-Clapeyron relation (O'Gorman and Schneider, 2008). The weakest LHF increase is found with the 10%- and 20%- threshold schemes, with which the precipitation weakens significantly during warming. Similarly, the strongest increase of LHF with the Seifert-Beheng scheme is consistent with the strengthened precipitation. The boundary layer generally moistens with warming, contrary to the fixed-SST experiments. The surface RH increases slightly with warming, and the larger RH increase occurs with the weaker increases of LHF (i.e., the threshold schemes), since the background wind speed is assumed to be unchanged.

The reduced climate sensitivity in the subtropics is consistent with the mechanism proposed by Pierrehumbert (1995). The free troposphere is very moist in the deep tropics, and the strong LW water vapor feedback limits the increase of outgoing longwave radiation (OLR) with surface warming, resulting in a very high climate sensitivity or even a transition into the runaway greenhouse (c.f. Appendix for further discussion of this phenomenon and how it affects the calculation of the tropical RCE profile). The subtropical free troposphere is relatively dry, and the OLR can respond more sensitively with surface warming, i.e., the subtropical climate sensitivity would

be small if no lateral energy exchange could occur. In reality, the subtropical and tropical regions are coupled by the large-scale circulations (the Hadley and Walker cells, and the wind-driven ocean circulation), which transports excessive energy from the tropics into the subtropics, where it can be radiated out of the atmosphere. Although this mechanism is schematically clear, it is complicated by the existence of the subtropical boundary layer, which contributes strongly to the OLR but is decoupled from the free troposphere by the trade-wind inversion. Larson et al. (1999) further investigated this problem with a two-box energy balance model that represents the tropical warm-pool and the subtropics respectively, and the subtropics is further separated into free troposphere and the boundary layer. Their approach differs from our study by their formulation of interactive large-scale energy flux, which effectively limits the SST difference between their tropical and tropical boxes.

In the fixed heat uptake LES experiments, a larger subtropical climate sensitivity is attainable if the total heat export decreases strongly with cooling, either by reducing the surface heat uptake (similar to the fixed-SST experiments), or by decreasing the advective drying/cooling in the boundary layer. The latter mechanism affects the surface energy budget mostly by controlling the surface RH: if the surface RH increases with warming, LHF can increase only modestly with significant increase of SST, and the surface energy balance is still satisfied. Based on the fixed-SST results, if 4 K sensitivity were to occur in the subtropics with unchanged LHF after doubling $CO_2$, the surface heat uptake should decrease by 20 W $m^{-2}$, or RH should increase by 3%, or the surface wind speed should decrease by 20%. Whether these changes or

their combinations are dynamically probable is left open for future study.

### 2.4.2 Height of Cu layer base: matching between the buoyancy flux and the lifted condensation level

The liquid water buoyancy flux is defined as the 'buoyancy flux' carried by $\theta_l$ and $q_t$ as if no condensation occurs. It includes the virtual effects of water vapor, but does not account for the buoyancy production by latent heat release. This flux is equivalent to the flux $\tilde{Q}_\rho$ in Stevens (2007), which is shown to be related to the $\theta_l$ and $q_t$ fluxes ($Q_l = \overline{w'\theta_l'}$ and $R = \overline{w'q_t'}$ respectively) by equation (17) in that paper:

$$\tilde{Q}_\rho = a_1 Q_l + a_2 \theta R, \tag{2.4}$$

where

$$a_1 \approx \left(\frac{\theta_v}{\theta_l}\right)\left(1 + \frac{q_l L_v}{c_p T}\right)^{-1} \approx 1, \quad a_2 = \frac{R_v}{R_d} - 1 \approx 0.61. \tag{2.5}$$

Here, $\theta_l$ is the liquid water potential temperature, $\theta_v$ is the virtual potential temperature, $L_v$ is the latent heat of water vapor, $R_v$ and $R_d$ are gas constants of vapor and dry air, and $c_p$ is the isobaric specific heat of air. In the subcloud layer where no condensates are present, $\tilde{Q}_\rho$ is just the $\theta_v$-flux.

Now we express all fluxes in the energy form, i.e., writing $S = \rho c_p Q_l$, $L = \rho L_v R$, and $\tilde{B} = \rho c_p \tilde{Q}_\rho$. Thus, $S$ and $L$ are equal to SHF and LHF at the surface, and

equation (2.4) can be rewritten as:

$$\tilde{B} = a_1 S + \frac{a_2 c_p \theta}{L_v} L, \tag{2.6}$$

where $(a_2 c_p \theta)/L_v \approx 7.3\%$ when $\theta = 300$ K. This means that the contribution to the surface buoyancy flux change per unit change of LHF is only 7.3% of that per unit change of SHF.

In Fig. 2.2 (top row), the steady-state $\tilde{B}$ profiles are plotted against height. The surface buoyancy flux generally increases with warming in the fixed-SST experiments, as the increase of LHF is exponential ( $+30$ W m$^{-2}$ for doubling $CO_2$) and dominates over the corresponding SHF change ($-2$ W m$^{-2}$) even after multiplying the small factor of 7.3%. This is most significant in the Seifert-Beheng cases in which the surface RH decreases significantly with warming. In comparison, the fixed surface heat uptake experiments generally show decrease of surface buoyancy flux with warming, corresponding to the weakened increase of LHF under the surface energy constraints. The slope of the subcloud layer buoyancy flux profile corresponds to the buoyancy sink by other processes, such as by horizontal advection and by radiative cooling. Since the advective cooling is prescribed to remain fixed with warming and the advective drying is not strong enough to contribute significantly to the buoyancy sink with the 7.3%-factor, the slope is thus proportional to the radiative cooling rate. In warmer climates, the clear-sky radiative cooling is weakened, and the buoyancy flux should decrease more slowly with height. This is found to be true for most cases, except for the coldest case of Seifert-Beheng scheme in which the unrealistic cloud

deck strongly reduces the subcloud layer radiative cooling.

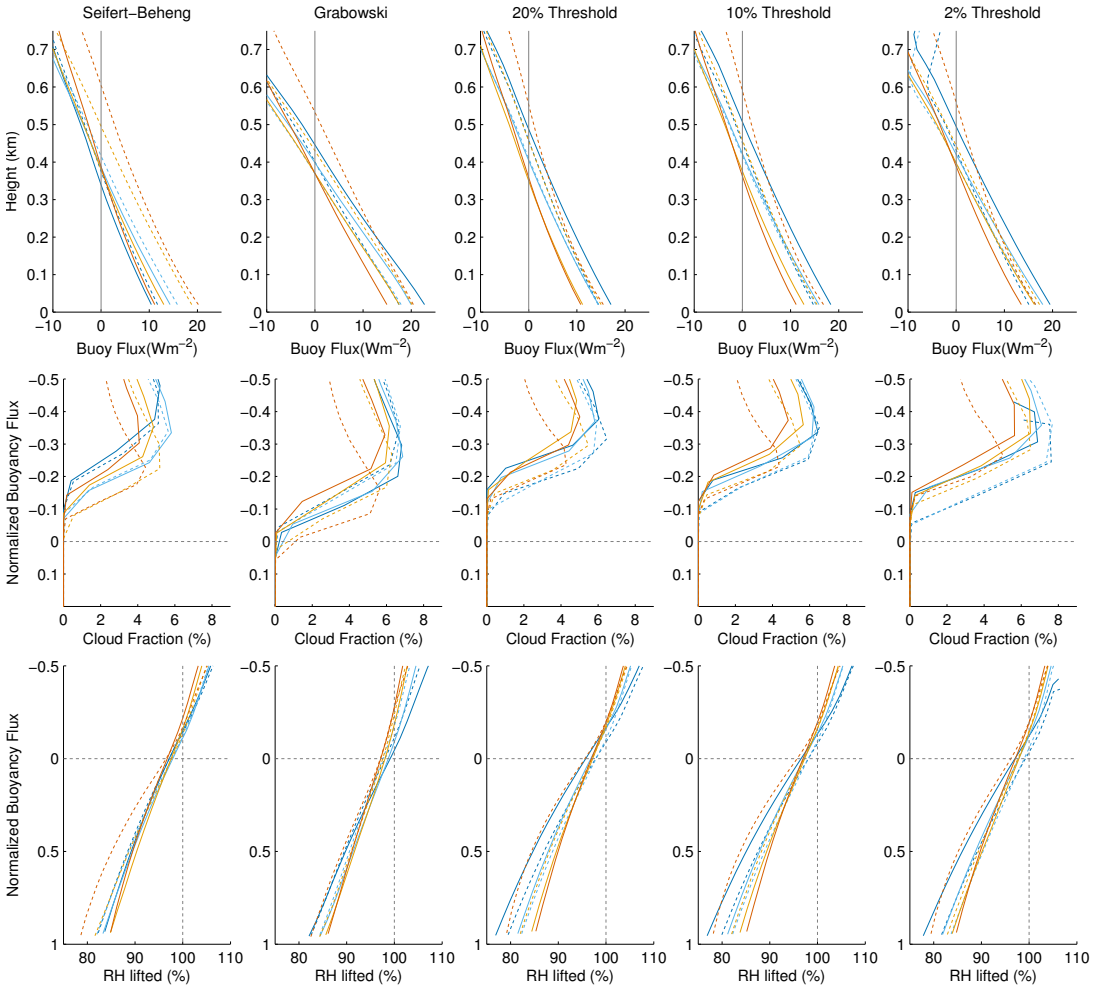


Figure 2.2: The steady-state subcloud layer profiles of buoyancy flux, cloud fraction and RH of a lifted surface parcel. The line color and styles are the same as in Fig. 2.1.

The intercept (the surface buoyancy flux) and slope (the radiative cooling) effects jointly determine the level of zero buoyancy flux (LZBF). In the fixed-SST experiments, both the increase of surface buoyancy flux and the decrease of radiative cooling contribute to the higher LZBF. However, these two effects counteract in the fixed surface heat uptake experiments, and the decrease in the LZBF with warming is only significant in the colder climates where the decrease of surface buoyancy flux dominates over the change in radiative cooling.

As the vertical buoyancy flux decreases with height in the subcloud layer, it can be used as the vertical coordinate. In Fig. 2.2, the mean cloud fraction (middle row) and RH of a lifted surface parcel (bottom row) are plotted against the normalized buoyancy flux. The results show that LZBF is very close to the base of Cu clouds. This is consistent with the traditional conception that the subcloud layer is dynamically similar to a dry-convective boundary layer (DCBL), the top of which is marked by the level where the buoyancy flux decreases to some ratio $k$ of its surface value. This entrainment efficiency $k$ usually takes a small negative value (e.g., $k = -0.2$), representing the entrainment of the more buoyant air aloft into the DCBL at the expense of turbulent kinetic energy (TKE) related to the overshooting dry updrafts. It has been argued by Neggers et al. (2006, Fig. 5) that the dynamical feedbacks by the cumulus updraft mass flux and the compensating subsidence are very effective in regulating the subcloud layer conditions, which keep the LCL near the subcloud mixed-layer top as predicted by the DCBL theory. However, it was shown in Schalkwijk et al. (2013) that the entrainment efficiency $k$ for the subcloud layer may be dependent on the configuration of LES, and in our simulations $k \approx -0.1$, which is slightly smaller in magnitude than the DCBL value.

The base height of Cu layer also roughly corresponds to the lifted condensation level (LCL) of a surface air parcel, which generally decreases with increased surface RH. The predicted changes of LCL from surface RH tendencies are also consistent to the model results of Cu layer base (Fig. 2.1): surface RH decreases with warming in fixed-SST experiments corresponding to the rise of LCL, and vice versa in the fixed

heat uptake experiments. This is also clear in Fig. 2.2, where the LCL of a lifted surface parcel (with 1 standard deviation of moisture anomaly, i.e., $q_t = \bar{q}_t + \sigma_{q_t}$) is almost the same as the LZBF.

Therefore, we have two separate constraints of Cu layer base (LZBF and LCL), and they should match each other in the steady state. A simple model can be developed with this constraint to study the equilibrium condition of surface temperature, given the surface energetic budget terms of net radiative fluxes and surface heat uptake, the atmospheric advective and radiative tendencies, and the surface bulk transfer coefficients. The system is not yet closed, since there are only two constraints (LCL-LZBF matching and the surface energy balance) but three unknowns (SST, air temperature at the surface layer, surface RH). The remaining constraint is related to the regulation of subcloud layer by interaction with the cumulus layer. Similar approaches have been taken as early as by Betts (1976), and more recently by various studies, such as Neggers et al. (2006); Bellon and Stevens (2012); Schalkwijk et al. (2013). These simple models usually involve some assumption of the interaction between the subcloud layer and cumulus layer, either by explicitly representing the fluxes across the transition layer, or by implicitly coupling both layers and studying the heat and moisture budgets of the whole system. Instead of the studying the coupled system, we have chosen to bracket off the cumulus-subcloud interaction for now, and study the subcloud layer separately and close the equations by prescribing the surface RH. In reality, the change of the cumulus-subcloud interaction affects the subcloud layer conditions, including the RH. Thus, the surface RH can be seen as an indicator for

such interaction. The equations and closures are as follows:

$$S_0 = \rho c_p (C_D \|U\|)(\mathrm{SST} - T_a), \quad S(z) = S_0 + \frac{\partial S}{\partial z} z, \tag{2.7}$$

$$L_0 = \rho c_p (C_D \|U\|)(q_s(\mathrm{SST}) - q_a), \quad L(z) = L_0 + \frac{\partial L}{\partial z} z, \tag{2.8}$$

$$B = \frac{\theta_v}{\theta} S + \frac{a_2 c_p \theta}{L_v} L = (1 + a_2 q_a)\, S + a_2 \frac{c_p \theta}{L_v} L, \tag{2.9}$$

where $a_2 = R_v/R_d - 1 \approx 0.61$. And the closures are given by

$$q_a = q_s(T_a) \cdot \mathrm{RH}_a, \tag{2.10}$$

$$h = \mathrm{LCL}(\mathrm{RH}_a, T_a), \quad B(h) = kB(0), \tag{2.11}$$

$$0 = S_0 + L_0 + Q - \Delta R. \tag{2.12}$$

The model is then solved with parameters diagnosed from the LES: surface net radiative heating $\Delta R = 213$ W m$^{-2}$ in the current conditions, and increase by 7.5 W m$^{-2}$ per doubling $CO_2$ corresponding to reduced LW cooling partly compensated by reduced SW heating, both due to the increase of water vapor. The subcloud radiative cooling contributes to $\partial S/\partial z|_{\mathrm{rad}} = -1.87 \times 10^{-2}$ W m$^{-3}$, and this cooling decreases by $1.25 \times 10^{-3}$ W m$^{-3}$ per doubling of $CO_2$. The advective tendencies follow the LES configurations, contributing to $\partial S/\partial z|_{\mathrm{adv}} = -1.63 \times 10^{-2}$ W m$^{-3}$ which is constant with climate, and $\partial L/\partial z|_{\mathrm{adv}} = -1.14 \times 10^{-2}$ W m$^{-3}$ in the control climate, which increases by 20% per doubling of $CO_2$ according to the Clausius-Clapeyron relation. The parameter $k = 0$ is found to agree better with the LES results, and we assume fixed values of ocean heat uptake $Q = 65$ W m$^{-2}$, and $C_D\|U\| = 1 \times 10^{-2}$ m s$^{-1}$,

RH = 80% for the reference climate and increases by 1% per doubling of $CO_2$. The system is then solved iteratively, and the surface budgets are shown in Table 2.4. In comparison, the results with ocean heat uptake values and RH similar to the fixed-SST experiments are also shown. It is as expected that this subcloud model mimics the LES results, such as the SST tendencies, change of surface fluxes, and the height of the cumulus base. However, this simple model is extremely sensitive to the prescribed RH: a 1% increase in RH from the control case will lead to a 1.2 K increase of SST. The reduced LCL imposed by the increased RH is matched by corresponding reduction of $B_0$. Since the total surface heat flux is kept fixed, this reduction of $B_0$ is only possible with reduced SHF and increased LHF concurrently, i.e., with increased Bowen ratio corresponding to warmer SST. Since the subcloud temperature increases with RH, the moist static energy is also very sensitive of RH. Thus, some closure for the cumulus-subcloud interaction that regulates the subcloud conditions is important, so as to maintain the cumulus layer at neutral buoyancy with the saturated updrafts from the subcloud layer (Stevens, 2007).

In summary, the height of Cu-base generally increases with warming in the fixed-SST experiments, but decreases in the fixed surface heat uptake experiments. This is linked to the opposite trend of surface buoyancy flux in the two experiments, mostly contributed by the different response of LHF, which increases exponentially if SST is prescribed, but only grows modestly if SST and surface flux are constrained by the surface budget. The RH tendency is consistent with the change of Cu-base, indicative of a matching between LCL and LNBF. A simple model with prescribed surface RH

reproduces the LES results, but RH is in itself affected by the cumulus-subcloud interaction, and its closure depends on the representation of such interaction.

Table 2.4: The same as Table 2.3, but from the simple subcloud layer model with prescribed RH and QFLUX. RAD is the prescribed surface net downward radiative flux, and the top of LCL is also presented. FLUX experiments use fixed ocean heat uptake with prescribed RH similar to LES results; SST experiments use prescribed heat uptake values that are similar to the LES fixed-SST experiments and the corresponding RH.

| $CO_2$ | CASE | SST | TA | RH | SHF | LHF | RAD | QFLUX | LCL (m) |
|---|---|---|---|---|---|---|---|---|---|
| 0.25× | FLUX | 294.48 | 293.62 | 78.00 | 10.33 | 122.67 | 198.00 | 65.00 | 501.41 |
| | SST | 291.08 | 290.25 | 80.00 | 10.12 | 92.88 | 198.00 | 95.00 | 438.37 |
| 1.00× | FLUX | 299.38 | 298.82 | 80.00 | 6.66 | 141.34 | 213.00 | 65.00 | 471.65 |
| | SST | 300.20 | 299.73 | 82.00 | 5.56 | 132.44 | 213.00 | 75.00 | 423.61 |
| 4.00× | FLUX | 304.55 | 304.29 | 82.00 | 3.08 | 159.92 | 228.00 | 65.00 | 440.00 |
| | SST | 306.67 | 306.45 | 80.00 | 2.50 | 195.50 | 228.00 | 30.00 | 502.55 |
| 16.00× | FLUX | 310.21 | 310.25 | 84.00 | −0.36 | 178.36 | 243.00 | 65.00 | 406.87 |
| | SST | 313.85 | 314.08 | 78.00 | −2.59 | 285.59 | 243.00 | −40.00 | 593.89 |

### 2.4.3 Cloud fraction at the base of Cu layer

From Figs. 2.1 and 2.2, a peak in cloud fraction is found near the cloud base, and its value varies between 4% and 8%. While its exact value is dependent on the microphysics scheme, it tends to decrease slightly in the warmer climates in both fixed-SST and fixed heat uptake experiments. Since the two sets of experiments have very different responses of subcloud conditions and Cu-base height to warming, it is interesting that this behavior is shared by both experiments.

In Neggers et al. (2006) and Neggers et al. (2007), the cloud fraction at the Cu-base is formulated similarly to the probabilistic cloud scheme by Sommeria and Deardorff

(1977) and Cuijpers and Bechtold (1995): the total water specific humidity $q_t$ at the Cu-base is assumed to follow a Gaussian distribution, and the cloud fraction $A$ is a function of the normalized saturation excess $S = (q_t - q_{sat})/\sigma_{q_t}$. They then continue to parameterize $\sigma_q$ using the second moment equation, which is simplified into the following form:

$$\sigma_{q_t}^2 = -\overline{w'q_t'}\Big|_h \frac{\partial q_t}{\partial z}\Big|_h \cdot \frac{h}{w_*}, \tag{2.13}$$

where $h$ is the height of Cu-base, $w_*$ is the convective velocity scale in the subcloud layer. The underlying assumption is that the variance production by down-gradient turbulent transport is balanced by dissipation over the large-eddy timescale $h/w_*$. By combining this formulation with their assumption that the transport $\overline{w'q_t'}_h$ is also proportional to the area fraction $A$, the system is closed. The end result is a scaling that $A \propto \Delta h/h$, where $h$ is the depth of subcloud layer, and $\Delta h$ is the height between the cloud-base height and the height where the cloud fraction peaks. However, the scaling of $\Delta h/h$ and why it remains approximately constant is not discussed.

With our simulations, we test this idea by comparing the Cu-base peak cloud fraction against their respective normalized saturation excess $S$ and $\Delta h/h$ among different cases. The results are plotted in Fig. 2.3. It is found that the saturation excess at the layer of peak cloud fraction is generally a good predictor for the cloud fraction: higher excess (less negative) corresponds to larger cloud fraction. However, the results with different microphysics schemes don't collapse into a single line, which indicates that the shape of cloud-bottom distribution may depend on the choice of microphysics scheme. More specifically, the microphysics schemes that precipitate

more efficiently and simulate a shallower Cu layer, such as the Grabowski scheme and the threshold scheme at 2%, are more cloudy than the other schemes with the same normalized saturation excess. The saturation excess at the cloud bottom is still positively correlated with the peak cloud fraction, but the correlation is somewhat weaker. The predicted cloud core fraction from the equation (12) of Neggers et al. (2006), i.e.,

$$a^c = 0.5 + 0.36 \text{ atan}\left(1.55S\right), \tag{2.14}$$

would evaluate to 1% to 2.5% of cloud core fraction for $S = -3$ to $-2.5$ as typical from the LES results. This means that more than half of the clouds at Cu-base are mechanically driven and non-buoyant. The estimate for cloud core is related to the estimate of cloud fraction in the interior of the Cu layer, and it is also found in both sets of LES simulations that (Fig. 2.3) the interior Cu fraction is strongly linked to the peak Cu fraction by a factor of roughly 0.5, except for the 2%-threshold scheme with which the precipitation is strong and cloud fraction decays quickly with height.

In contrast, the index $\Delta h/h$ does not seem to be a good predictor of cloud fraction. It is further found that $\Delta h$ does not change much in the different cases (varying between 110 m and 160 m), but $h$ differs by $> 300$ m. Therefore, $\Delta h/h$ is just the inverse of $h$, and the positive correlation in the fixed-SST experiments might just be a coincidence that both $1/h$ and the peak cloud fraction increases with warming, and vice versa for the negative correlation in the fixed heat uptake experiments. It should be noted that the current vertical resolution of LES at $\Delta z = 40m$ is just sufficient to resolve the transition layer, and it remains to be tested whether increasing the

vertical resolution will improve the correlation between $\Delta h/h$ and cloud fraction.

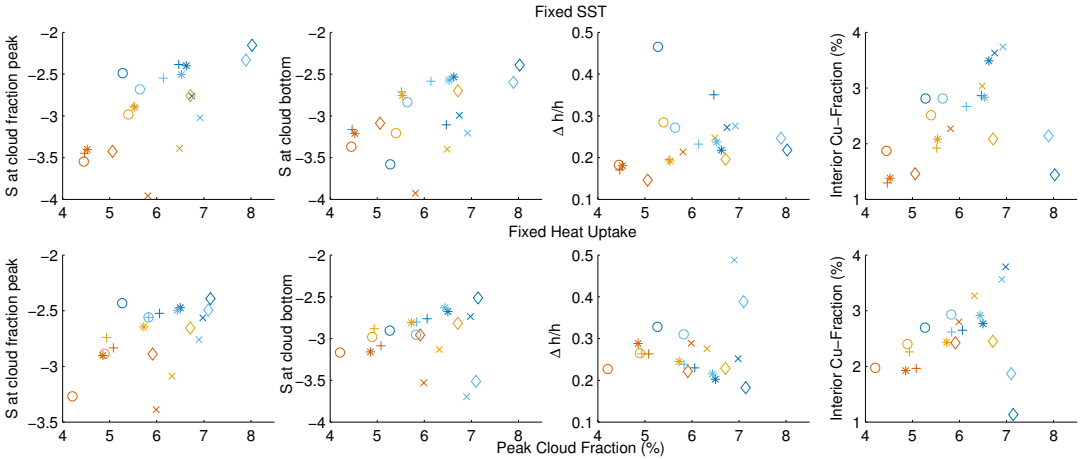


Figure 2.3: The predictors for Cu-base cloud fraction: normalized saturation excess ($S$) at the cloud fraction peak and at the cloud bottom, and the ratio between depths of the transition layer and the subcloud layer. The rightmost figure shows the cloud fraction in the interior of Cu layer. The different colors represent different $CO_2$ concentrations as in Fig. 2.1 and 2.2. The signs represent different microphysics schemes (square: Seifert-Beheng; cross: Grabowski; plus: 20%-threshold; star: 10%-threshold; diamond: 2%-threshold).

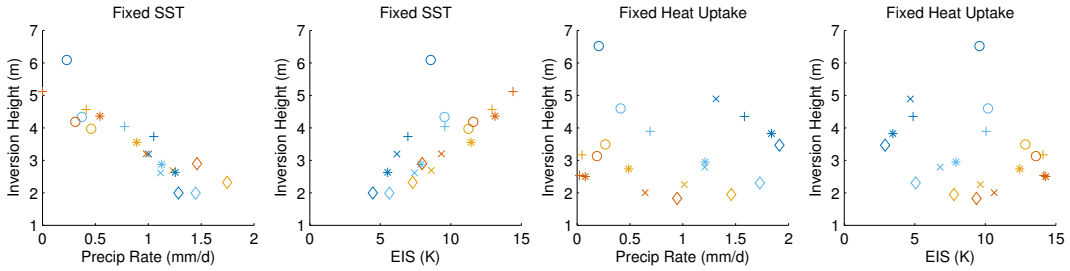


Figure 2.4: The relation between precipitation rate, estimated inversion strength (EIS), and the inversion height. The colors and signs represent the same cases as in Fig. 2.3.

Finally, it has been shown in Fig. 2.2 (bottom row) that the derivative of RH of the lifted parcel with respect to the normalized buoyancy flux (as the height coordinate) decreases with warming in the absolute sense. If the normalized buoyancy flux is

denoted as $B_n$, then we can write:

$$\left|\frac{\partial \mathrm{RH}}{\partial B_n}\right| = \left|\frac{\partial \mathrm{RH}}{\partial \mathrm{T}}\right|\left|\frac{\partial \mathrm{T}}{\partial \mathrm{z}}\right|\left|\frac{\partial B_n}{\partial \mathrm{z}}\right|^{-1} = \Gamma h\left|\frac{\partial \mathrm{RH}}{\partial T}\right|, \tag{2.15}$$

where $\Gamma$ is the lapse rate. Note that if $h$ does not change much, this equation will be dependent on the derivative of RH with respect to $T$ at constant $q$. It can be calculated from the Clausius-Clapeyron relation that, by warming a saturated parcel by 1 K, its RH will decrease by 6.6% if initially $T = 281$ K, but only by 5.5% if initially $T = 306$ K. From equation (2.15), this decrease in $|\partial \mathrm{RH}/\partial \mathrm{T}|$ with warming contributes to a decrease of $|\partial \mathrm{RH}/\partial B_n|$, if $h$ decreases or remains fixed as in the fixed heat uptake experiments. However, if $h$ increases as in the fixed-SST experiments, the tendency of $h$ will contribute to a strong increase of the slope. The comparison of the slopes in Fig. 2.2 shows that the $h$ contribution is mostly limited in the subcloud layer, and it is not strongly linked to the slope $|\partial \mathrm{RH}/\partial B_n|$ in the cloud layer. In the cumulus layer where condensation affects $\Gamma$, it is also expected that $\Gamma$ will decrease with warming, which means that the conditional stability becomes stronger and less favorable for dry updrafts to ascend.

It is also shown in Fig. 2.2 (bottom row) that the slope $|\partial \mathrm{RH}/\partial B_n|$ is linked to the RH of the lifted parcel in the cloud layer. If the cloud layers were dynamically similar, i.e., the peak cloud fraction occurs at the same $\partial B_n$, this slope would be proportional to the saturation excess of the lifted parcel and therefore linked to the cloud fraction. There is evidence in Fig. 2.2 that the warmer profiles have smaller RH-slopes and are less over-saturated in the cloud layer, consistent with the decrease

of cloud fraction. However, this argument is incomplete: the peak cloud fractions do not occur at exactly the same $\partial B_n$; the change of $|\partial \mathrm{RH}/\partial T|$ is small compared to the change of this slope; the condensational heat of Cu clouds feeds back into this slope through its influence on $\Gamma$. Therefore, a more quantitative analysis is needed to further evaluate this change and its possible effect on the cloud fraction.

### 2.4.4 Inversion height and strength: entrainment competes with precipitation

Fig. 2.4 shows the inversion heights versus the precipitation rates and the estimated inversion strength (EIS) across the different climates and precipitation schemes. The EIS is linked to the SST, the static stability ($\gamma = \partial\theta/\partial z$), and the inversion height $H_{\mathrm{inv}}$ as follows:

$$\mathrm{EIS} \approx \theta_{\mathrm{trop}}(H_{\mathrm{inv}}^{+}) - \theta_{\mathrm{sub}}(H_{\mathrm{inv}}^{-}) = (\mathrm{SST}_{\mathrm{trop}} - \mathrm{SST}_{\mathrm{sub}}) + (\gamma_{\mathrm{trop}} - \gamma_{\mathrm{sub}}) \cdot H_{\mathrm{inv}}, \quad (2.16)$$

with the assumption that the subtropical free tropospheric temperature profile follows that of the tropics. The $\gamma_{\mathrm{trop}}$ and $\gamma_{\mathrm{sub}}$ terms represent the average static stabilities below the inversion height in the tropics and in the subtropics, respectively. From the LES results, the EIS is estimated as the potential temperature difference between the level just above the inversion and the level 600 m below the inversion.

As the climate warms, the static stability below $H_{\mathrm{inv}}$ increases more strongly in the tropics than in the subtropics because of the stronger latent heat effect, i.e.,

the difference in stability $\Delta\gamma = \gamma_{\rm trop} - \gamma_{\rm sub}$ increases with warming. This already contributes to the increase in estimated inversion strength as discussed by Wood and Bretherton (2006). The second panel of Fig. 2.4 shows that, when $\Delta{\rm SST} = {\rm SST}_{\rm trop} - {\rm SST}_{\rm sub}$ is fixed, the warmer cases usually have higher EIS than the colder cases with the same $H_{\rm inv}$. For the same magnitude of warming (i.e, the same color), $\Delta\gamma$ are similar and thus EIS seems to be proportional to $H_{\rm inv}$. However, the fourth panel of Fig. 2.4 shows that the effect of the reduced subtropical surface climate sensitivity also contributes strongly to the EIS in the fixed surface heat uptake experiments. Comparing the different warming scenarios (different colors), this is both reflected in a shift of x-intercept to the right (i.e., $\Delta$SST increases) with warming, and an increased slope of $d{\rm EIS}/dH_{\rm inv}$ (i.e., $\Delta\gamma$ increases). However, from the energetic point of view, the EIS cannot increase too strongly with unchanged subsidence, since this will induce a strong warming in the boundary layer by top entrainment. This constraint on EIS is consistent with the decrease of inversion height with warming in the fixed heat uptake experiments that maintains realistic EIS values. The steady state EIS in the fixed surface heat uptake experiments is only slightly different from that in the fixed-SST experiments, implying that the sensible heat gain by entrainment is very similar between both sets of experiments, but their inversion heights differ significantly.

As discussed in Section 2.3, the precipitation process warms and dries the boundary layer, which competes against the similar effects by the entrainment process. A stronger precipitation efficiency usually corresponds to weaker entrainment warming and drying, corresponding to a lower EIS value and lower inversion height. This is

found to be robust for all experiments: 0.2 mm $d^{-1}$ precipitation leads to a latent heating of about 6 W $m^{-2}$ (Blossey et al., 2013), which can exactly compensate for the decrease of entrainment heating due to a 1 K decrease of EIS (assuming a typical subsidence rate of 5 mm $s^{-1}$ at the top of Cu layer).

In both experiments, the non-precipitating limit of EIS is approximately 15 K. Thus, based on the heating-compensation argument, precipitation rate can be estimated as [0.2 mm $d^{-1}$ $K^{-1}\cdot$(15 K$-$EIS)]. Fig. 2.5 shows that the actual precipitation rates agree well with the estimated values, especially for the fixed heat uptake experiments. Reversely, the EIS can be estimated quantitatively if the precipitation rate is known.

For some simulation cases with very weak precipitation, an anvil layer occurs at the inversion layer. Fig. 2.6 shows the analyses of how the peak inversion cloud fraction is linked to the characteristics of the inversion layer, such as EIS (Wood and Bretherton, 2006), and the cloud top entrainment instability (CTEI) parameter $\kappa$ (Lock, 2009) defined as

$$\kappa = \frac{\Delta\theta_e}{(L/c_p)\Delta q_t} = 1 + \frac{\Delta\theta_l}{(L/c_p)\Delta q_t}, \tag{2.17}$$

which quantifies the strength of negative buoyancy generation by the evaporation of detrained liquid water from cumulus top. Specifically, Lock (2009) shows in a set of idealized LES experiments that a cumulus layer robustly develops an anvil layer when $\kappa < 0.3$. Similar increase of anvil fraction with decreased $\kappa$ is also found in our simulations, but the relation is much less clear. Especially in the fixed heat

uptake experiments, the cold climate may have a very small $\kappa$ due to the low $\Delta q_t$, but EIS $\approx \Delta\theta$ is also small and seems to be dominant, consistent with a small anvil fraction. This may suggest that the EIS acts as a cap on the CTEI criterion, which is only effective when EIS is high enough to suppress overshooting updrafts. The precipitation process, albeit deemed as unimportant for the anvil formation in Lock (2009), can indirectly affect the EIS by reducing the required entrainment, as discussed above. This indirect precipitative effect on EIS makes it difficult to clarify whether the positive correlation between EIS and anvil fraction is due to the direct dynamical effect of inversion on turbulent mixing, or due to the precipitative effect that reduces liquid water flux into the inversion which also happens to reduce the EIS. Further investigation is required to separate these two effects.

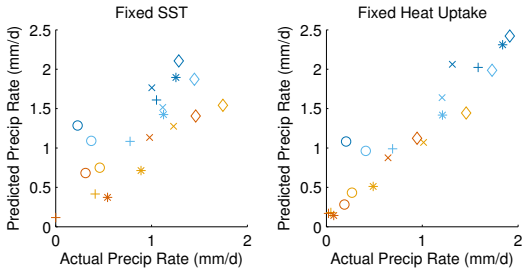


Figure 2.5: Similar to Fig. 2.4, but for the comparison between actual precipitation rate and estimated precipitation rate from EIS.

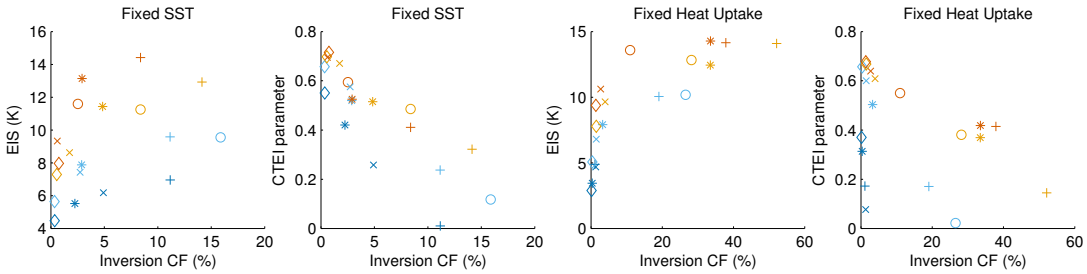


Figure 2.6: Similar to Fig. 2.4, but for the comparison between the peak cloud fraction at inversion layer and the predictors (EIS and CTEI).

### 2.4.5 Summary of cumulus response mechanisms

The response of the different components of the Cu-topped boundary layer to the idealized climate change has been analyzed in detail, under the assumptions that the surface heat uptake, the lateral advection, the subsidence, and the surface wind don't change significantly. The major results are summarized as follows:

1. The subtropics warm less than the deep tropics under the same increase of $CO_2$: the dryness of the subtropical free troposphere allows more efficient radiative cooling of the surface and the boundary layer (Pierrehumbert, 1995). Under such circumstances, the SST and lapse rate differences between the tropics and the subtropics would increase, resulting in a strong increase of EIS at a given height. With unchanged subsidence, the inversion height has to decrease so that the EIS and the subsidence warming both decrease and match the boundary layer energy heat budget.

2. The inversion height is very sensitive to the precipitation process. With stronger precipitative warming and drying, the required entrainment warming and drying across the inversion are reduced, corresponding to weaker EIS and a lower inversion height. This effect is modulated by the change of precipitation efficiency with warming, and model results show some sensitivities to the choice of microphysics scheme.

3. Under the surface energy constraint, LHF can only increase modestly with warming, subject to the upper limit of net downward radiative flux at the sur-

face (O'Gorman and Schneider, 2008). The surface RH increases with warming, consistent with the decreased surface buoyancy flux. The base height of Cu layer decreases correspondingly, but not as strongly as the decrease of inversion height.

4. The local maximum cloud fraction at the base of Cu layer decreases slightly with warming, consistent with the increase of the normalized saturation deficit at the level of maximum cloud fraction. This may be related to the reduced adiabatic RH lapse rate and the enhanced static stability in the Cu-base transition layer with warming. The decrease of Cu cloud fraction may also be related to the decrease of cloud fraction in the interior of the Cu layer.

5. Anvil at the inversion layer may be enhanced with warming, but it is strongly sensitive to the precipitation scheme. Further investigation is required to determine which of the increased cloud-top stability, increased CTEI, or decreased precipitation is the main contributor.

We may further separate the contributions to the change of LWP by cloud-base, cloud-top, and the interior. The cloud-base and cloud-top are respectively defined as the bottom and top 10% height of the whole Cu layer, and the rest is defined as the interior. The LWP and maximum cloud fraction of the base and top layers, as well as the LWP and mean cloud fraction of the interior layer are shown in Tables 2.5 and 2.6. Although the spread among models with different microphysics is large, the total LWP shows a decreasing trend from 1.0× to 16.0× $CO_2$ in the fixed heat uptake experiments, mostly contributed by the decrease in the middle of the Cu layer,

even though the cloud fraction does not change much. Additionally, the decrease of bottom cloud fraction also contributes to the decrease of LWP, although the reduced precipitation in threshold schemes contributes to an increase of anvil LWP. Therefore, the LWP change in the fixed heat uptake experiment is mostly contributed by the LWP decrease related to the Cu layer shallowing, because of the sinking of the Cu layer top with warming. The fixed-SST experiments, however, show an increase of LWP up to $4.0 \times$ $CO_2$ related to the increase of LWP in the middle layer.

In summary, the sinking of inversion layer, which arises from the reduced subtropical warming and the consequent increase of inversion strength, is related to the weak decrease of LWP with warming in the fixed heat uptake experiments. Subsequent research will focus on improving the coupling between the large-scale circulation and the cloud-topped boundary layer, and relating the change of subsidence and horizontal advection to dynamical constraints. This will help us to better quantify the current results.

## 2.5 Conclusion

In this study, we have performed LES experiments to investigate the response of the subtropical marine boundary clouds to the idealized climate change driven by increase of $CO_2$. Different from previous approaches with fixed SST, we have coupled a mixed-layer ocean surface interactively with the atmosphere, such that the surface energy budget is closed at the steady state under the assumption that the surface heat uptake does not change significantly.

Table 2.5: The diagnosis of cloud layer parameters for the fixed-SST experiments. $z_B$, $z_T$ are the bottom and top of cumulus layer, $CF_l$ and $CF_h$ are the lower and upper peaks of cloud fraction, and $CF_m$ is the mean cloud fraction in the middle of cumulus layer. $LWP_l$, $LWP_m$, and $LWP_h$ are the liquid water path (g m$^{-2}$) in the lower 20%, middle 60%, and upper 20% of the cumulus layer, and $LWP_t$ is the column total liquid water path.

| $CO_2$ | $z_B$ | $z_T$ | $CF_l$ | $CF_m$ | $CF_h$ | $LWP_l$ | $LWP_m$ | $LWP_h$ | $LWP_t$ |
|---|---|---|---|---|---|---|---|---|---|
| 0.25× | 420.00 | 3359.99 | 6.48 | 1.93 | 16.60 | 3.77 | 13.56 | 4.09 | 21.42 |
| | ±40.00 | ±1495.91 | ±0.89 | ±0.52 | ±27.00 | ±2.49 | ±8.81 | ±4.37 | ±15.28 |
| 1.0× | 388.00 | 3020.00 | 6.48 | 2.25 | 6.60 | 3.46 | 17.89 | 4.75 | 26.10 |
| | ±52.15 | ±940.08 | ±0.79 | ±0.48 | ±6.61 | ±1.50 | ±11.37 | ±4.18 | ±16.98 |
| 4.0× | 436.00 | 3256.37 | 5.79 | 1.94 | 5.93 | 3.43 | 18.71 | 5.55 | 27.69 |
| | ±53.67 | ±875.55 | ±0.57 | ±0.59 | ±5.50 | ±1.08 | ±10.61 | ±4.29 | ±15.75 |
| 16.0× | 564.00 | 3763.86 | 4.75 | 1.26 | 3.04 | 3.27 | 15.26 | 4.92 | 23.45 |
| | ±82.95 | ±858.56 | ±0.58 | ±0.40 | ±3.16 | ±0.86 | ±7.52 | ±4.20 | ±11.93 |

Table 2.6: The same as Table 2.5, but for the fixed heat uptake experiments.

| $CO_2$ | $z_B$ | $z_T$ | $CF_l$ | $CF_m$ | $CF_h$ | $LWP_l$ | $LWP_m$ | $LWP_h$ | $LWP_t$ |
|---|---|---|---|---|---|---|---|---|---|
| 0.25× | 460.00 | 4389.95 | 6.28 | 1.34 | 16.70 | 5.42 | 14.41 | 4.18 | 24.01 |
| | ±109.54 | ±1138.71 | ±0.69 | ±0.60 | ±35.69 | ±2.45 | ±9.63 | ±6.44 | ±17.23 |
| 1.0× | 404.00 | 3148.58 | 6.37 | 2.17 | 10.15 | 3.62 | 17.59 | 4.58 | 25.78 |
| | ±45.61 | ±879.79 | ±0.59 | ±0.60 | ±11.89 | ±1.48 | ±11.28 | ±4.00 | ±16.64 |
| 4.0× | 372.00 | 2589.82 | 5.60 | 2.26 | 23.85 | 2.25 | 13.96 | 7.96 | 24.18 |
| | ±43.82 | ±603.50 | ±0.75 | ±0.36 | ±21.25 | ±0.66 | ±6.85 | ±6.62 | ±12.98 |
| 16.0× | 372.00 | 2283.97 | 5.10 | 2.10 | 17.29 | 1.49 | 10.25 | 6.37 | 18.11 |
| | ±43.82 | ±486.21 | ±0.72 | ±0.26 | ±17.27 | ±0.42 | ±3.92 | ±5.33 | ±8.60 |

For the cumulus regime, it is found that the subtropical SST cannot keep up with the assumed 4 K tropical climate sensitivity per doubling $CO_2$, since the LW cooling is very effective to cool off the subtropical boundary layer and the ocean surface. The inversion layer sinks in response to the increased SST difference between the tropics and the subtropics, contributing to the shallowing of the cumulus layer and the decrease of LWP with warming. Weaker but robust responses of decreased cloud fraction at cloud base and the sinking of LCL also occur, but they don't contribute significantly to the change in LWP. The simulations are relatively sensitive to the modeled precipitation efficiency, which counteracts the entrainment and affects the inversion strength and height. The decrease of inversion height does not occur in the fixed-SST experiments: the surface energy budget is unconstrained and contributes to an exponential increase of LHF into the boundary layer, which instead causes the inversion to rise slightly. This comparison highlights the importance of the energetic constraints on the predicted cloud-topped boundary layer response to the climate change. Further investigation will be undertaken to improve the representation of the large-scale circulation and energy fluxes under warming conditions in the LES experiments.

# 2.6 Appendix: Determination of the tropical RCE reference profiles

## 2.6.1 Basic assumptions and governing equations

The relaxation profile $T(z)$ is computed offline with an RCE model of the equatorial atmospheric column. It is composed of three parts: the upper atmosphere (i.e., stratosphere), the lower atmosphere (i.e., troposphere), and the surface. The governing equations of this model are ($H$ is the tropopause height):

In the stratosphere, where pure radiative equilibrium is satisfied:

$$\frac{\partial F_{net}}{\partial z} = 0 \quad (z > H). \tag{2.18}$$

In the troposphere, where strict convective equilibrium is satisfied:

$$\frac{\partial \theta_e}{\partial z} = 0 \quad (z < H). \tag{2.19}$$

The temperature and radiative fluxes at the tropopause $H$ are continuous:

$$T(H^-) = T(H^+), \quad F_i^{\uparrow\ (\downarrow)}(H^-) = F_i^{\uparrow\ (\downarrow)}(H^+), \tag{2.20}$$

where $i$ represents different spectral bands in the radiation model. The second continuity is automatically guaranteed by the radiation models such as RRTMG.

The surface has to satisfy the energetic balance:

$$F^{\downarrow}_{SW} - F^{\uparrow}_{SW} - F^{\uparrow}_{LW} - Q = LHF + SHF + F^{\uparrow}_{LW}. \tag{2.21}$$

Here $Q$ represents the ocean cooling. With a fixed surface albedo, the three terms on the left hand side are only dependent on the atmospheric column, and the three terms on the right hand side are dependent on surface temperature $T_s$ as:

$$LHF = \rho L_v C_D \|U\|(q_s(T_s) - q_a), \tag{2.22}$$

$$SHF = \rho C_p C_D \|U\|(T_s - T_a), \tag{2.23}$$

where $\rho$ is air density at the surface layer, $L_v$ is the latent heat of evaporation, $C_p$ is the isobaric specific heat of air, $\sigma$ is Stefan-Boltzmann constant, $C_D$ is the bulk drag coefficient, and $\|U\|$ is the surface velocity scale. Here we assume $C_D\|U\| = 5\times10^{-3}$ m s$^{-1}$. The surface upward LW radiation $F^{\uparrow}_{LW}$ is determined by the radiation scheme.

The combined system of atmosphere and the surface also needs to satisfy the energetic balance, i.e., :

$$F^{\downarrow}_{SW}(TOA) - F^{\uparrow}_{SW}(TOA) + F^{\downarrow}_{LW}(TOA) - F^{\uparrow}_{LW}(TOA) = Q + A \tag{2.24}$$

where $A$ represents the atmospheric energy sink by advection. $Q$, $A$, and the surface relative humidity (RH) are all prescribed. Some assumptions that link the specific

humidity profile $q(z)$ to the temperature profile $T(z)$ are also needed to close the system.

### 2.6.2 Solution algorithm

The system can be solved with the radiation scheme coupled to a convection adjustment scheme, e.g., Manabe and Wetheral.Rt (1967), which mimics the real convection process and guarantees the energy conservation throughout this process. For simplicity, we have instead designed a simpler scheme that does not exactly follow this physical process, but numerically guarantees that the solution at convergence satisfies the RCE constraint. The algorithm is as follows:

1. For a given tropopause height $H$, initialize the loop with some arbitrary $T(z)$, $q(z)$, and SST.

2. Calculate radiative tendencies $\dot{T}_{rad}$ for the whole column with the radiation scheme.

3. Adjust stratosphere temperature $T|_{z>=H}$ according to $\dot{T}_{rad}$. This guarantees that $\dot{T}_{rad} = 0$ for $z >= H$ at convergence, i.e., the stratosphere is in pure radiative equilibrium.

4. With the adjusted tropopause temperature $T(H)$, compute the convective equilibrium profile that matches $T(H)$, and update $T|_{z<=H}$ to the computed value. Therefore, the convective equilibrium is strictly enforced, and the continuity of $T$ at $z = H$ is explicitly satisfied.

5. Update moisture profile $q(z)$ with the updated $T(z)$.

6. Adjust SST to explicitly satisfy the energy balance, subject to the constraints of equations (2.21) and (2.24). Either $A$ or $Q$ needs to be prescribed. This explicit SST adjustment guarantees that the whole system is energetically closed at convergence.

7. Loop over steps 2-6 until convergence.

This solution process is repeated for different heights of $H$, so a set of RCE solutions are obtained. The RCE solution that satisfies our requirement (e.g., SST or surface flux $Q$) is obtained by interpolation. Although the interpolation at the end seems inexact, it is actually preferred against the reverse approach, i.e., enforcing the requirement and solving the tropopause. The technical difficulty for the reverse approach is that the tropopause is no longer at full levels. Thus, the temperature continuity cannot be made exact, but is instead subject to one-sided extrapolation of tropospheric and stratospheric profiles to find the intersect. This is also inexact and causes more severe numerical problems, such as the oscillation of tropopause that leads to the failure of convergence. By having $H$ at full levels, the current algorithm is found to guarantee convergence.

### 2.6.3 RRTMG RCE profiles

In the calculation of tropical RCE profile, the equatorial annual mean insolation and mean cosine of solar zenith angle are used. The column is assumed to be cloud-free, but the surface albedo is tuned up from the RRTMG default value of 7% to 30%

to account for the cloud SW effect. This value is close to the prescribed albedo for idealized GCM studies without explicit cloud radiative effects, such as O'Gorman and Schneider (2008). The surface RH used to calculate the moist adiabat and the surface LHF are assumed to be 80%, but in the radiation scheme, the RH is assumed to be 70% throughout the troposphere and 1% in the stratosphere. Only the $CO_2$ concentration is varied among the RRTMG gas species.

Fig. 2.7 shows the tropical RCE solutions of surface air temperature corresponding to different values of atmospheric transport, assuming the ocean heat transport is 0 W $m^{-2}$ and 50 W $m^{-2}$, respectively. As shown in Table 1, the ocean-atmosphere combined loss of energy is around 50 W $m^{-2}$ for both assumptions. If the total energy loss does not change with different $CO_2$ concentrations, multiple solutions would occur for doubling $CO_2$, and the system will jump to a much warmer solution at around $2.5 \times CO_2$. This is a numerical verification that the moist tropical atmosphere may be susceptible to a local runaway greenhouse regime with the strong water vapor feedback. This can be avoided if the heat export increases with warming.

In the current set of climate change experiments, we have instead prescribed the climate sensitivity to $4K$ per doubling $CO_2$. This corresponds to almost no change in the total heat export at lower $CO_2$ concentrations, and about $3 - 5$ W $m^{-2}$ increase of heat export per doubling of $CO_2$ up to $16 \times CO_2$.

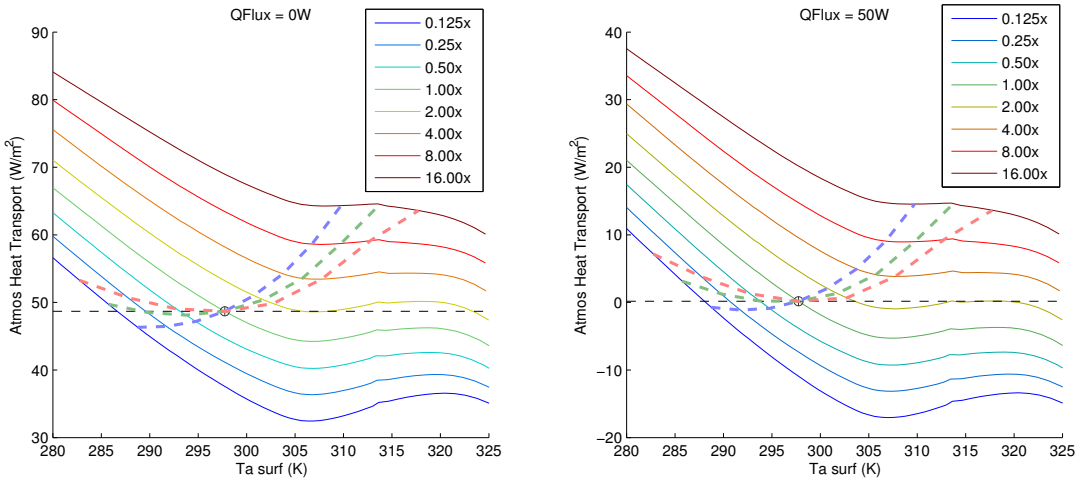


Figure 2.7: The required atmospheric heat transport that maintains the surface layer air temperature, assuming that the ocean heat export is $Q = 0$ W m$^{-2}$ and 50 W m$^{-2}$ respectively. Different solid lines represent different $CO_2$ concentrations, and the dashed lines represent the required atmospheric transport for the equatorial ECS of 3 K (blue), 4 K (green), and 5 K (red). The black dashed line represent the atmospheric transport required for the current climate.

# Chapter 3

# Eddy-diffusivity mass-flux scheme for the unified representation of turbulence-convection processes

## 3.1 Introduction

Low clouds have been identified as the largest uncertainties in climate change projections (Cess et al., 1990, 1996; Bony and Dufresne, 2005; Webb et al., 2006; Dufresne and Bony, 2008; Vial et al., 2013). The cloud dynamics and the related turbulence and convection processes occur at scales much smaller than the resolutions of current-day general circulation models (GCMs). Thus, they must be represented by sub-grid scale (SGS) parameterization schemes. However, these SGS closures in current climate models are usually decomposed into several largely independent parameterization schemes for different cloud and convective processes (c.f. Neale et al., 2010; Donner et al., 2011). For example, a typical climate model contains separate parameterizations for boundary layer turbulence, shallow convection, and deep convection. These separate parameterizations usually do not converge as the resolution is increased or as physical limits are taken, such as the limit of the latent heat of

vaporization approaching zero, in which all SGS closures should represent dry turbulence. Moreover, the parameterization schemes typically only interact through their influence on the grid scale (GS) conditions, and thus the cumulus convection may not be well coupled to the boundary layer processes which it originates from. The closures also may not be adapted to the increasing resolution, with which the assumptions of quasi-equilibrium breaks down. This makes it difficult to represent the interactions and smooth transition among different cloud and convective regimes. It leads to problems such as a proliferation of adjustable parameters in the closures, to biases such as the early diurnal peak of convective rainfall over land, and uncertainties such as that about the response of marine boundary layer clouds to climate change. The increase of resolution has also lead to the grey-zone problem, where the assumption of quasi-equilibrium in the conventional diagnostic convection scheme breaks down. All of these problems require a unified and physically-motivated parameterization scheme that is flexible for the transitions across scales and regimes.

Here we propose an eddy-diffusivity mass-flux (EDMF) closure to represent all SGS turbulent, convective, and cloud processes in a unified parameterization scheme. It follows the work of Siebesma and Teixeira (2000), Soares et al. (2004), and Siebesma et al. (2007), in which the SGS motion is decomposed into two components: the environment and the updrafts. The turbulent motions in the environment are assumed to be isotropic and contribute to downgradient SGS fluxes. They are represented by an eddy-diffusivity (ED) scheme that relates the turbulent fluxes to the GS gradient. The organized upward motion such as dry thermals and cumulus convection are pa-

rameterized as entraining updraft plumes. A single bulk updraft is usually used to represent the ensemble effect of convection, but efforts to include multiple updrafts are also being made (Sušelj et al., 2013). This model can be coupled with a probabilistic cloud scheme (e.g., Sommeria and Deardorff, 1977) to form a complete closure for the SGS processes. An alternative decomposition method by Lappen and Randall (2001) represents the environment and the updraft separately by two assumed Gaussian distributions. Albeit similar in ideology, this approach is beyond the scope of our present work.

In this study, we extend the EDMF framework to include the prognostic term that represents the life cycles of updrafts, and the downdraft term that represents the dynamical effects of evaporating precipitation. The consistent decomposition of environment, updrafts, and downdrafts is deduced theoretically without the conventional approximation of small updraft area, which makes this scheme more flexible for representing convection in models of different scales.

This chapter is organized as follows: Section 3.2 presents the basic equations of the EDMF scheme; Section 3.3 lists the closures for the environment and draft equations; Section 3.4 presents an single-column idealized case study on the EDMF scheme for different low cloud regimes, and discusses the sensitivity of EDMF parameters; Section 3.5 provides a summary for this work and a prospective on future development of this scheme. Section 3.6 (Appendix A) shows the strict theoretical deduction of the EDMF equations and clarifies the underlying assumptions; Section 3.7 (Appendix B) illustrates the numerical implementation of the EDMF equations, and the work-flow

of the EDMF scheme as in the single column model.

## 3.2 Basic configuration of the EDMF scheme

The EDMF approach is essentially a domain decomposition method that separates the regions with organised updrafts and downdrafts, where non-local mass-flux (MF) transport dominates, from the rest of the domain known as the environment, where local turbulent mixing by eddy-diffusivity (ED) dominates. The EDMF equation originates from the conditional average of vertical velocity and scalar equations on the updraft, downdraft, and environment, with parameterized interaction terms such as the fractional entrainment rate $\epsilon$ and detrainment rate $\delta$.

In the current approach, the following simplifications are made:

- Individual updrafts and downdrafts are assumed to be homogeneous; therefore, only the 1st-order moments (i.e., draft-mean values) are parameterized;
- The environment is parameterized with a 1.5-order closure: the environmental TKE is closed in addition to the environment-mean values, which is then used to diagnose the 2nd order moments including the tracer variances and vertical tracer fluxes;
- The horizontal velocity is assumed to be the same for drafts and the environment, i.e., there is no convective momentum transport;
- The density differences between drafts and the environment are neglected except in the calculation of updraft velocity, which makes the EDMF scheme like a

subdomain-filtered anelastic system.

However, the usual simplification of infinitesimal draft areas in the mass-flux formulation is found to be only consistent with the domain decomposition for steady updrafts, and all 2nd order moment equations are inconsistent with this simplification (c.f., the last section of this chapter for the special case of TKE). To improve the representation of evolving updrafts, and to be flexible for future inclusions of 2nd order moment equations, we have retained the prognostic terms ($d/dt$ terms) in all equations.

In the current single column model (SCM), we use moist conserved variables $\phi = \theta_l, q_t$, where $\theta_l$ is the liquid water potential temperature, and $q_t$ is the total water mixing ratio. They can be related to $T, q, q_l$ approximately as:

$$\theta_l = \left(T - \frac{L_v}{c_p} q_l\right) \cdot \left(\frac{p_0}{p}\right)^{\frac{R_d}{c_p}}, \quad q_t = q + q_l. \tag{3.1}$$

The only source terms for $\theta_l$ and $q_t$ in the convective process are precipitation and reevaporation. Schematically, other variables such as horizontal momentum $(u, v)$, turbulent kinetic energy (TKE), and second-order covariance terms $\overline{\theta_l' \theta_l'}$, $\overline{\theta_l' q_t'}$, $\overline{q_t' q_t'}$ can also be convected according to the same set of equation; however, the source terms $S_\phi$ may be more complicated. In the current version of the EDMF scheme, only $\theta_l, q_t$ are carried as tracers for both the drafts and the environment, and additionally TKE, $(u, v)$ are taken as tracers of the environment. The evolution equations of these tracers and their required closures are simply listed below without detailed discussion, while more detailed theoretical deductions and discussions are presented in Appendix

A (i.e., Section 3.6).

The nomenclatures of subscripts and superscripts are defined as follows: $i$ represents the i-th draft; $n$ represents environment; $E_i$ represents the entrained air into the i-th draft; $D_i$ represents the detrained air from the i-th draft; $T$ represents the domain mean. Overlines that represent averaging are all omitted, except for the second-order moments (e.g., the turbulent fluxes) and except in the Appendix A (i.e., Section 3.6).

- Draft velocity $w^i$: (closure for $\epsilon_i$ is required)

$$\frac{\partial w^i}{\partial t} + \frac{1}{2}\frac{\partial (w^i)^2}{\partial z} = aB_u^i + b\epsilon_i w^i (w^n - w^i) \tag{3.2}$$

- Draft fraction $a_i$: (closures for $\delta_i$ and the boundary value of $a_i$ are required)

$$\frac{\partial (\rho a_i)}{\partial t} + \frac{\partial (\rho a_i w^i)}{\partial z} = \rho a_i w^i (\epsilon^i - \delta^i) \tag{3.3}$$

- Draft tracer $\phi^i$: (closures for $\phi^i$ at the draft boundary, and its in-draft source term $S_\phi^i$ are required)

$$\rho a_i \frac{\partial \phi^i}{\partial t} + \rho a_i w^i \frac{\partial \phi^i}{\partial z} = \rho a_i w^i \epsilon^i (\phi^n - \phi^i) + \rho a_i S_\phi^i \tag{3.4}$$

- Grid-mean tendency due to mass flux $(d\phi^T/dt)_{MF}$:

$$M^i = \rho a_i (w^i - w^T), \quad \left.\frac{d\phi^T}{dt}\right|_{MF} = -\frac{1}{\rho}\frac{\partial}{\partial z}\sum_{i \neq n}\Big(M^i(\phi^i - \phi^n)\Big) \tag{3.5}$$

- Grid-mean tendency due to eddy diffusivity $(d\phi^T/dt)_{ED}$: (closure for eddy diffusivity $K$ is required)

$$\left.\frac{d\phi^T}{dt}\right|_{ED} = -\frac{1}{\rho}\frac{\partial}{\partial z}\Big(a_n\rho\overline{w'\phi'}^n\Big) = \frac{1}{\rho}\frac{\partial}{\partial z}\Big((\rho a_n K)\frac{\partial\phi^n}{\partial z}\Big) \tag{3.6}$$

- Sum of grid-mean tendencies: (cloud scheme and closure for environmental precipitation $S^n_\phi$ are required)

$$\left.\frac{d\phi^T}{dt}\right|_{EDMF} = \left.\frac{d\phi^T}{dt}\right|_{MF} + \left.\frac{d\phi^T}{dt}\right|_{ED} + \left.\frac{d\phi^T}{dt}\right|_{S}, \quad \left.\frac{d\phi^T}{dt}\right|_{S} = S^T_\phi = \sum_{i\neq n}(a_i S^i_\phi) + a_n S^n_\phi \tag{3.7}$$

- TKE prognostic equation: ($E^T = a_n E^n$, $m_i = a_i w^i$; TKE source terms need to be parameterized)

$$\left.\frac{dE^T}{dt}\right|_{EDMF} = \left.\frac{dE^T}{dt}\right|_{MF} + \left.\frac{dE^T}{dt}\right|_{ED} + \left.\frac{dE^T}{dt}\right|_{S} \tag{3.8}$$

$$\begin{aligned}\left.\frac{dE^T}{dt}\right|_{MF} = &-\frac{1}{\rho}\frac{\partial}{\partial z}\sum_{i\neq n}\Big((m_i - \rho a_i w^T)(-E^n)\Big) \\ &+ \frac{1}{\rho}\sum_{i\neq n}\Big(m_i\delta_i\big(\frac{1}{2}(w^i - w^n)^2\big) - m_i\epsilon_i E^n\Big)\end{aligned} \tag{3.9}$$

$$\left.\frac{dE^T}{dt}\right|_{ED} = -\frac{1}{\rho}\frac{\partial}{\partial z}\Big(a_n\rho\overline{w'E'}^n\Big) = \frac{1}{\rho}\frac{\partial}{\partial z}\Big((\rho a_n K)\frac{\partial E^n}{\partial z}\Big) \tag{3.10}$$

$$\left.\frac{dE^T}{dt}\right|_{S} = a_n(P^n_E + B^n_E + D^n_E) \tag{3.11}$$

## 3.3 Closures

### 3.3.1 Drafts

The draft areas $A_1, \ldots, A_{n-1}$ can either be updrafts or downdrafts, depending on the sign of velocity $w^i$. For the aim of representing shallow convection, we currently only include updrafts in our schemes and only consider the closures for updrafts, but the equations and numerical discretization for downdrafts will be of the same form of updraft, except for the closure assumptions.

According to equations (3.2), (3.3), and (3.4), we need to parametrize for the vertical velocity $w^i$, fractional entrainment/detrainment rates $\epsilon_i$, $\delta_i$, the tracer concentration $\phi^i$, the turbulent transport in the updraft $\overline{w'\phi'}^i$, and the tracer source term $S^i_\phi$. Additionally, we need to know about the initial boundary condition for $m_i$ and $\phi^i$. Then the set of equations is locally a first-order convection equation, and can be solved numerically. The parameterizations will be described in the following parts.

#### 3.3.1.1 Boundary conditions

The updraft equations are essentially transport equations, for which the inflow conditions, i.e., the bottom conditions need to be provided. In our current model, mid-level convections are not considered yet, and thus it is assumed that all updrafts originate from the lowest level of the column (i.e., near the surface), and we only need to prescribe the initial velocity and physical parameters of the updraft.

There are two ways to prescribe the initial condition. Practically, it can be taken effectively as the flux into the bottom of the updraft column. Or more physically,

we can alternatively assume zero-flux at surface, but prescribe the entrainment in the lowest level in a different way from the interior levels. These two views will be discussed in Appendix B. For both representations, the bottom vertical velocity and the tracer properties are prescribed as in the following equations:

$$w^i_{bot} = 0, \quad \phi^i_{bot} = \phi^n_{bot} + \beta \frac{\overline{w'\phi'}^n}{\sqrt{E^n_{surf}}}. \tag{3.12}$$

It is assumed that the standard deviation of the environment variable $\phi^n$ is just $\overline{w'\phi'}^n (E^n_{surf})^{-0.5}$, where $E^n_{surf}$ is the surface environmental TKE. Factor $\beta$ represents the normalized anomaly of the entrained air compared with environmental mean. It is always assumed that the entrained air represents the most buoyant tail of the environment distribution, and the amount of entrained air depends on the bottom mass flux. Explicitly, if there is only one bulk updraft, the relation between $\beta$ and $m^i_{bot} = \rho_{bot} a^i_{bot} w^i_{bot}$ is as follows:

$$\beta = \frac{1}{\sqrt{2\pi}\gamma} \exp\Big[ - \frac{\big[\Phi^{-1}(1-\gamma)\big]^2}{2} \Big], \tag{3.13}$$

where $\gamma = \min\big(1, (a^i w^i \Delta t)/(a^n \Delta z)\big)$ is the fraction of bottom-level environmental air entrained into the updraft within a single time step $\Delta t$, and $\Phi^{-1}$ is the inverse of the cumulative distribution function of the standard Gaussian distribution. For the boundary mass-flux, it is currently assumed that the updraft fraction $a_i$ is constant at the lowest level. Effectively, the mass-flux into the lowest level of the updraft is the same as the mass-flux through the top of this level. Physically, when the environment

favors updraft (e.g., the surface is very buoyant so the updraft accelerates quickly), the mass-flux through the lowest level would also be stronger.

The bottom mass-flux in our closure is not explicitly related to convective available potential energy (CAPE), which differs from quasi-equilibrium (QE) convective schemes where the bottom mass-flux is set explicitly proportional to CAPE. However, the mass-flux at the level of free convection (LFC) implicitly depends on the convective inhibition (CIN), which is defined as the integrated negative buoyancy of an air parcel lifted from the surface to its LFC. If CIN is sufficiently large, the updraft (as lifted air mass) decelerates rapidly due to negative buoyancy and terminates before reaching LFC. In this case, the updraft only contributes to the boundary layer mixing without growing into active cumulus. As CIN decreases, the updraft decelerates less and the mass-flux reaching LFC increases, which is similar to the formulations of CIN-based closures. Thus, it would be interesting to compare our model to the explicit CIN-based closures, such as Bretherton et al. (2004).

#### 3.3.1.2 Vertical velocity

The vertical velocity can be advected as a tracer according to equation (3.71), i.e.,

$$\frac{1}{w^i}\frac{\partial w^i}{\partial t} + \frac{\partial w^i}{\partial z} = \epsilon_i(w^{E_i} - w^i) - \delta_i(w^{D_i} - w^i) - \frac{1}{m_i}\frac{\partial}{\partial z}(\frac{m_i}{w^i}\overline{w'w'}^i) + \frac{S^i_\phi}{w^i}. \qquad (3.14)$$

Following previous approaches such as by Bretherton et al. (2004), the source term and the turbulent advection term are then combined into two terms: $B^i_u$ represents the buoyant acceleration, and $P^i$ represents the pressure effect. Assuming further

that $w^{D_i} = w^i$, $w^{E_i} = w^n$, we can obtain the following form of equation:

$$\frac{\partial w^i}{\partial t} + \frac{1}{2}\frac{\partial (w^i)^2}{\partial z} = \epsilon_i w^i (w^n - w^i) + (B_u^i - P^i). \tag{3.15}$$

The pressure term $P^i$ can be parametrized as a linear combination of two terms respectively proportional to $B_u$ and the entrainment term, i.e.

$$\frac{\partial w^i}{\partial t} + \frac{1}{2}\frac{\partial (w^i)^2}{\partial z} = aB_u^i + b\epsilon_i w^i (w^n - w^i). \tag{3.16}$$

The coefficients are chosen as in Bretherton et al. (2004), such that $a = 1, b = 2$.

#### 3.3.1.3 Entrainment and detrainment

For a single updraft, the lateral entrainment is assumed to be simply inverse-proportional to the height, i.e.

$$\epsilon_i = \frac{\kappa}{z}, \tag{3.17}$$

where $\kappa = 0.41$ is the von Karman's constant. The bottom entrainment is prescribed to satisfy the assumption for fixed updraft fraction at surface.

For a single updraft, the lateral detrainment is by default set to zero. Alternatively, we may also use a height-dependent formulation ($\delta \sim 1/z$), or incorporate a relative humidity (RH) dependent factor, such as Kain and Fritsch (1990), or Bechtold et al. (2014). The top detrainment is simply prescribed (according to the mass-flux prognostic equation) to limit the updraft area fraction below some threshold (currently assumed to be twice of the bottom area fraction), and the updraft is assumed

to detrain completely at the level where its vertical velocity becomes 0. For a bulk updraft, the total detrainment should schematically be the mass-flux weighted mean of top detrainment of various updrafts that detrain at different levels. Thus the detrainment rate profile would be more smooth throughout the column. We have not included this effect at present, on the basis that detrainment is more important at higher levels where the single-updraft formulation is able to detrain efficiently.

In our current model, there are no stochastic effects in both entrainment and detrainment rates, but these effects can be included in a similar way to Sušelj et al. (2013). It should be noted that, since the synoptic fluctuations are strong in the GCM, the mean updraft effect can mimic some stochastic effects by sampling over time, and the importance of representing SGS fluctuation may not be as strong as for the fixed-forcing single column experiments.

#### 3.3.1.4 Source terms

The updraft source term currently only includes liquid-phase precipitation, which increases $\theta_l$ and decreases $q_t$.

The liquid water $q_l$ at each level is diagnosed with

$$q_l^i = \max(0, q_t^i - q_s^i), \tag{3.18}$$

where $q_s^i = q_s\Big(T(\theta_l^i, q_l^i, p), p\Big)$ is the saturation specific humidity in the updraft.

The current updraft precipitation scheme is a simple threshold scheme: the portion of liquid water $q_l$ that exceeds some fixed ratio $f_{\text{prec}}$ of the saturation specific humidity

$q_s^i$ is instantaneous converted to rain and precipitate out, i.e., the precipitation sink of $q_t^i$ (denoted as $P_r^i$) is as follows:

$$P_r^i = \max(0, q_l^i - f_{\text{prec}} q_s^i), \tag{3.19}$$

where for now we choose $f_{\text{prec}} = 0.02$. The resulted change of $\theta_l^i$ and $q_t^i$ can be computed from $P_r^i$ with the following equations:

$$\Delta\theta_l^i\Big|_{\text{prec}} = \frac{\theta_l^i}{T_l^i}\frac{L_v}{c_p}P_r^i = \left(\frac{p}{p_0}\right)^{-\frac{R_d}{c_p}}\frac{L_v}{c_p}P_r^i, \tag{3.20}$$

$$\Delta q_t^i\Big|_{\text{prec}} = -P_r^i. \tag{3.21}$$

Alternatively, we may compute $P_r^i$ with more sophisticated microphysics, such as the scheme of Tiedtke (1993) which assumes a fixed conversion rate from cloud water to precipitation, or the Grabowski (1998) mixed-phase microphysics closure.

$\Delta\theta_l^i\Big|_{\text{prec}}$ and $\Delta q_t^i\Big|_{\text{prec}}$ are added to $\theta_l^i$ and $q_t^i$ immediately after the upward integration for each level, so that the upper level feels instantaneously the precipitative effect at lower levels. It remains to be tested whether this is preferable over doing the precipitative adjustment after the column integration is completed.

## 3.3.2 Environment

### 3.3.2.1 Boundary conditions

In the model, only the lower boundary of the environmental mixing is parameterized (i.e., the surface fluxes), and the upper boundary is assumed to be natural

(i.e., turbulent fluxes are zero). There is currently no separate parameterization for boundary-layer top entrainment mixing.

The surface fluxes of $T, q, u, v$ are computed with the Monin-Obukhov scheme as in the FMS model. They are assumed to affect only the environment part of the domain, but the entrainment into the updraft at the lowest level would effectively provide a partitioning between updraft and environment.

The surface value of environmental turbulent kinetic energy (TKE) is diagnosed with the following equation, based on Potty et al. (1997) and Witek et al. (2011):

$$E^n_{surf} = k_u u_*^2 + k_w w_*^2, \tag{3.22}$$

where $k_u = 3.75, k_w = 0.2$ are constants, $u_*$ is the surface turbulent velocity scale computed in the Monin-Obukhov scheme, and $w_*$ is the vertical velocity scale defined as follows:

$$w_* = \Big( \frac{g z_* \overline{w'\theta'_v}|_s}{\theta_v(z_s)} \Big)^{\frac{1}{3}}, \tag{3.23}$$

where $z_*$ is the depth of the sub-cloud mixed layer (defined as 'boundary layer depth' in previous versions of the model), and $\theta_v(z_s)$ is the virtual potential temperature at surface.

Note that the surface fluxes can be written in energetic form or covariance form,

and they are related as the following equations:

$$F_T = \rho_s c_p \overline{w'T'}\Big|_s, \tag{3.24}$$

$$F_q = \rho_s \overline{w'q'}\Big|_s, \tag{3.25}$$

where $\rho_s$ is the density of air at surface. Assuming that $q_l = 0$ at surface, and neglecting the fluctuation in surface pressure in the computation of $\theta$ at surface, these equations can be rewritten as:

$$F_{SHF} = \rho_s c_p \overline{w'T'}\Big|_s \approx \rho_s c_p \overline{w'\theta_l'}\Big|_s, \tag{3.26}$$

$$F_{LHF} = \rho_s L_v \overline{w'q'}\Big|_s \approx \rho_s L_v \overline{w'q_t'}\Big|_s, \tag{3.27}$$

$$\begin{aligned} F_{BF} &= \rho_s c_p \overline{w'T_v'}\Big|_s \approx \rho_s c_p \overline{w'\theta_v'}\Big|_s \\ &\approx \rho_s c_p \Big( \overline{w'\theta_l'}\Big|_s \big(1 + (\epsilon^{-1} - 1) q_t\big) + \overline{w'q_t'}\Big|_s (\epsilon^{-1} - 1)\theta_l \Big), \end{aligned} \tag{3.28}$$

where $F_{SHF}, F_{LHF}, F_{BF}$ are surface sensible heat flux, surface latent heat flux, and surface buoyancy flux (in energetic form), respectively. $\epsilon = c_{p,d}/c_{p,wv} \approx 0.622$ is the ratio of heat capacity between dry air and water vapor.

#### 3.3.2.2 Turbulent kinetic energy

The prognostic equation of turbulent kinetic energy (TKE) in the environment can also be written in a form similar with the form in equation (3.91):

$$\rho\frac{\partial}{\partial t}(a_n E^n) + (a_n E^n - E^T)\frac{\partial \rho}{\partial t} + \rho \mathbf{u}_h^T \cdot \nabla_h E^T + \rho w^T \frac{\partial E^n}{\partial z} + (E^n - E^T)\frac{\partial(\rho \overline{w}^T)}{\partial z}$$
$$= \sum_{i \neq n}(m_i \delta_i E^i - m_i \epsilon_i E^n + \frac{\partial(m_i E^n)}{\partial z}) - \frac{\partial}{\partial z}(\rho a_n \overline{w' E'}^n) + \rho a_n S_E^n, \tag{3.29}$$

where $E^n$ is the environmental TKE. $E^i$ is the updraft 'TKE' computed with environmental mean velocity. By assuming that the velocity difference between updraft and environment is mostly contributed by the vertical component, $E_i$ can be approximated as

$$E^i \approx \frac{1}{2}(w^i - w^n)^2. \tag{3.30}$$

The left hand side of equation (3.29) represents the large-scale advective tendencies. On the right hand side, the first term contains three terms in the summation, which represent the detrainment of updraft TKE into environment, entrainment of environmental TKE into updraft, and transport of environmental TKE by compensating subsidence, respectively. The second term represents the eddy-diffusive transport of TKE. The third term represents the sources and sinks of TKE, including buoyancy production $B_E^n$, shear production $P_E^n$, and dissipation $D_E^n$. They are defined as

follows:

$$S_E^n = P_E^n + B_E^n + D_E^n, \tag{3.31}$$

$$P_E^n = K_m\Big((\frac{\partial u^n}{\partial z})^2 + (\frac{\partial v^n}{\partial z})^2\Big), \tag{3.32}$$

$$D_E^n = -c_e\frac{(E^n)^{3/2}}{l_d}, \tag{3.33}$$

where $K_m$ is the eddy diffusivity, and $l_d$ is the diffusion length, defined as $l_d = l/c_{l_d}$, where $l$ is the mixing length which will be parametrized later. The constants are chosen as: $c_e = 0.16$, $c_{l_d} = 2.5$.

The buoyancy term $B_E^n$ is defined as

$$B_E^n = g\frac{\overline{w'\theta_v'}^n}{\theta_v^n}, \tag{3.34}$$

where the buoyancy flux $\overline{w'\theta_v'}^n$ needs to be computed separately for unsaturated (clear-sky) and saturated (cloudy) parts of the environmental area, i.e.,

$$\overline{w'\theta_v'}^n = (1-CC)(\alpha_D\overline{w'\theta_l'}^n + \beta_D\overline{w'q_t'}^n) + (CC)(\alpha_W\overline{w'\theta_l'}^n + \beta_W\overline{w'q_t'}^n), \tag{3.35}$$

$$\alpha_D = 1 + (\frac{1}{\epsilon} - 1)q_t, \quad \alpha_W = \Big(1 - q_t + \frac{q_s}{\epsilon}(1 + \frac{\epsilon L_v}{R_dT})\Big)\Big(1 + \frac{\epsilon L_v^2 q_s}{R_d c_p T^2}\Big)^{-1}, \tag{3.36}$$

$$\beta_D = (\frac{1}{\epsilon} - 1)\theta, \quad \beta_W = \theta\Big(\frac{L_v}{c_pT}\alpha_W - 1\Big). \tag{3.37}$$

#### 3.3.2.3 Eddy diffusivity: k-diffusivity approach

The turbulent transport terms in the form $(\partial/\partial z)(a_n \rho \overline{w'\phi'}^n)$ need to be parametrized with an eddy diffusivity $K_m$ as follows:

$$\overline{w'\phi'}^n = -K_m \frac{\partial \phi^n}{\partial z}. \tag{3.38}$$

One simple formulation for $K_m$ uses a k-diffusivity approach, i.e., a diffusivity profile that depends on both the surface buoyancy flux and boundary layer depth. This represents the surface-driven boundary layer. The formulation is as follows:

$$K_m = \kappa \Big( \big(\frac{u_*}{w_*}\big)^3 + c_{K_1} \kappa \frac{z}{z_*} \Big)^{\frac{1}{3}} \frac{z}{z_*} \Big(1 - \frac{z}{z_*}\Big)^2 z_* w_*, \tag{3.39}$$

where $\kappa = 0.41$ is the von Karman's constant, and $c_{K_1} = 39$ as in Mailhot and Benoit (1982), Siebesma et al. (2007), and Witek et al. (2011). $w_*$ is the vertical velocity scale as in equation (3.23). Note that at the limit of neutrally buoyant surface layer ($w_* \to 0^+$), the formulation takes the following form:

$$\lim_{w_* \to 0^+} K_m = \kappa u_* \frac{z}{z_*} \Big(1 - \frac{z}{z_*}\Big)^2 z_*. \tag{3.40}$$

For stably stratified surface layer ($w_* < 0$), we also formulate $K_m$ to be the limit value $\lim_{w_* \to 0^+} K_m$ in the above equation. This maintains some shear-driven mixing even in the stably-stratified boundary layer. The mixed-layer depth $z_*$ is formulated

with Richardson number for neutral or stable surface layers:

$$Ri(z) = gz\frac{(s_v(z) - s_v(z_s))/s_v(z_s)}{u(z)^2 + v(z)^2}, \tag{3.41}$$

where $s_v$ is the virtual dry static energy defined as

$$s_v = c_p T(1 + (\frac{1}{\epsilon} - 1)q - q_l) + gz. \tag{3.42}$$

$z_*$ is defined to be the level where Richardson number is 1 (i.e., $Ri(z_*) = 1$). And for unstable conditions, $z_*$ is computed by lifting a parcel with virtual dry static energy of $s_{v,p}$ from the surface and compute the level of neutral buoyancy of this parcel, without any condensation effect. This effectively determines the top of dry convective boundary layer, or the top of sub-cloud mixed layer. The detailed formulation for $s_{v,p}$ is

$$s_{v,p} = s_v(z_s) + \Delta s_v = s_v(z_s) + \frac{2\overline{w's'_v}|_s}{w_s}, \tag{3.43}$$

where $w_s$ is computed from Monin-Obukhov scheme as

$$w_s = \frac{k_m}{\kappa h_i}. \tag{3.44}$$

The major drawback of the k-profile diffusivity is the lack of representation of enhanced turbulent mixing by cloud top cooling, e.g., when stratus or stratocumulus occurs. The TKE-closure for eddy diffusivity is preferred over this method in such circumstances.

#### 3.3.2.4 Eddy diffusivity: TKE-based approach

The TKE-based eddy diffusivity takes the simple form as follows:

$$K_m = c_{K_2} l \sqrt{E^n}, \tag{3.45}$$

where $c_{K_2} = 0.25$ is a scaling constant as in Witek et al. (2011), $E^n$ is the environmental TKE, and $l$ is the mixing length. The formulation of the mixing length $l$ is a difficult problem, although from physical grounds it should depend on the following length scales, as given in Witek et al. (2011):

$$l_0 = \kappa z, \quad l_1 = \kappa z \Big(1 + a_l \frac{z}{L}\Big)^{b_l}, \quad l_2 = \tau \sqrt{E^n}, \quad l_3 = \frac{\sqrt{E^n}}{N}, \tag{3.46}$$

where each $l_i$ represents one factor that limits the vertical extent of turbulent eddies. $l_0$ is the height from the surface, and $l_1$ is similar to $l_0$ but includes the surface stability; $l_2$ assumes that the eddy size is proportional to eddy velocity with some given turnover time-scale; $l_3$ represents the limitation by stratification. $L$ is the Monin-Obukhov length defined as

$$L = -\frac{u_*^3 \theta_{v_s}}{\kappa g \overline{w' \theta_v'}|_s}, \tag{3.47}$$

and $N$ is the Brunt-Väisälä frequency defined as

$$N^2 = \frac{g}{\theta_v^n} \frac{\partial \theta_v^n}{\partial z}, \tag{3.48}$$

and $a_l, b_l$ are some constants. As in Witek et al. (2011), we use $a_l = -100, b_l = 0.2$ for unstable conditions, and $a_l = 2.7, b_l = -1.0$ for stable conditions.

The mixing length $l$ should be some combination of these length scales $l_i$. Currently we have chosen a simple formulation that is a combination of $l_1$ and $l_2$, following Witek et al. (2011).

#### 3.3.2.5 Source terms

There are two kinds of source terms in the environment. The source terms due to environmental precipitation are closely related to the turbulence and convection processes, and they are computed along with the EDMF scheme in the sub-grid closure. The source terms related to other processes, such as radiation and large-scale advection, are computed in other parameterization schemes or in the dynamical core, so they are imposed onto the sub-grid closure without direct interaction.

The precipitation scheme and the cloud scheme are closely coupled. After the physical variables $\theta_l, q_t$ in the whole column are computed for the new time-step, the cloud scheme is called to compute for the cloud fraction $CC$ and the liquid water $q_l$ at each layer. Then similar equation as (3.18) to (3.21) are used to compute the precipitation $P_r^n$, as well as tendencies for $\theta_l^n$ and $q_t^n$ due to precipitation.

$$q_l^n = \max\left[0, q_t^n - q_s\Big(T(\theta_l^n, q_l^n, p), p\Big)\right] \tag{3.18*}$$

$$P_r^n = \max(0, q_l^n - f_{\text{prec}} q_s^n) \tag{3.19*}$$

$$\Delta\theta_l^n\Big|_{\text{prec}} = \frac{\theta_l^n}{T_l^n}\frac{L_v}{c_p}P_r^n = \Big(\frac{p}{p_0}\Big)^{-\frac{R_d}{c_p}}\frac{L_v}{c_p}P_r^n \tag{3.20*}$$

$$\Delta q_t^n\Big|_{\text{prec}} = -P_r^n \tag{3.21*}$$

In the same way as described in Section 3.3.1.4, we may also use more sophisticated precipitation schemes that parametrize explicitly the autoconversion and accretion processes, as well as the partitioning between liquid and ice phases. For now the reevaporation is not included, but it can also be included by adding tendency terms similar to equations (3.20*) and (3.21*), but with reevaporation $E_r^n$ instead of $P_r^n$.

## 3.4 Case Study

The EDMF closure is incorporated into a single column model (SCM) based on the GFDL idealized GCM, similar to the one used by O'Gorman and Schneider (2008). Three cases are simulated and compared to LES results to evaluate the performance of the current formulation of EDMF closure and its sensitivity to the parameters. These cases are: (1) the dry convective boundary layer (DCBL) case following Soares et al. (2004), (2) the BOMEX shallow cumulus case following Siebesma and Cuijpers (1995), and (3) CGILS-like stratocumulus (S12) and cumulus (S6) cases that roughly follows Zhang et al. (2013) and Blossey et al. (2013), but with a simple two-stream

grey radiation scheme with idealized LW effects by water vapor (Merlis and Schneider, 2010) and water clouds (Stephens, 1978). It is coupled to an interactive 1m-depth mixed-layer ocean instead of fixing SST.

The SCM is configured to contain 60 vertical levels with stretched grid, and the vertical resolution in the lower troposphere is $\Delta z \approx 60$ m. It uses the leapfrog timestepping with the Robert-Assylin filter (Robert, 1966; Asselin, 1972), and the time step is fixed at $\Delta t = 150$ s. The DCBL and BOMEX are transient cases and are run for 12 hours, for which the output from hours 6-8 are compared to LES simulations under the same initial condition and forcings. The CGILS-like cases run for 10 days, and the conditions on days 8-10 are compared to the LES.

The EDMF scheme is set up as described, and the control simulation uses the TKE-based diffusivity and entrainment rate of $\epsilon = 0.8/z$ for the DCBL case, and $\epsilon = 1.6/z$ for the cloudy cases. Sensitivity tests are done on varying the entrainment rate (doubling or halving), using the k-profile diffusivity instead of TKE-based diffusivity, and using diagnostic updraft (i.e., disabling the prognostic terms in the updraft formulation).

Fig. 3.1 and Fig. 3.2 show the comparison between the SCM and LES results and between the different SCM sensitivity cases for the DCBL and BOMEX experiments, respectively. Although they represent different turbulence-convection regimes, some robust results are shared between these two tests. The control SCM experiments in both cases show good agreement with the LES for the mean profiles of $\theta_l$ and $q_t$, and this agreement is also shared by the k-profile diffusivity and the diagnostic

updraft cases. The relative contribution of ED and MF fluxes to the vertical turbulent transport is dependent on the choice of ED closure, but the total upward flux is relatively insensitive. However, the simulations show significant sensitivity to the entrainment rate: updraft with a smaller entrainment rate dilutes less and is relatively more buoyant, and therefore it can overshoot to a higher level and contributes to a deeper boundary layer. It is also found that the required entrainment rates are different for DCBL and BOMEX cases. This case dependence may imply the need for a regime-aware entrainment rate formulation. The agreement between SCM and LES on the BOMEX cloud fraction and liquid water profiles is also modest. The shape of cloud profile is similar between SCM and LES, but the inversion layer is too sharp in the SCM simulations, and the liquid water is overestimated by $\sim 50\%$. Incorporating multiple updrafts with different entrainment rates may help to spread out the detrainment across over some height and reduce the sharpness of the cloud top, making SCM results more realistic.

Fig. 3.3 shows the comparison between SCM and LES results on the CGILS-like cases with interactive radiation and mixed-layer ocean. These interactive components as well as the length of run which enables significant drift from the initial condition lead to a much larger spread among models, especially for the S12-like case where the cloud-top cooling is not sufficient for the SCM to maintain a stratocumulus layer. This is even more significant with the k-profile diffusivity simulation, where the cloud-top driven turbulence is totally missing from the prescribed k-profile, and thus the ED mixing is limited to very low levels (i.e., below the cloud bottom), and the MF

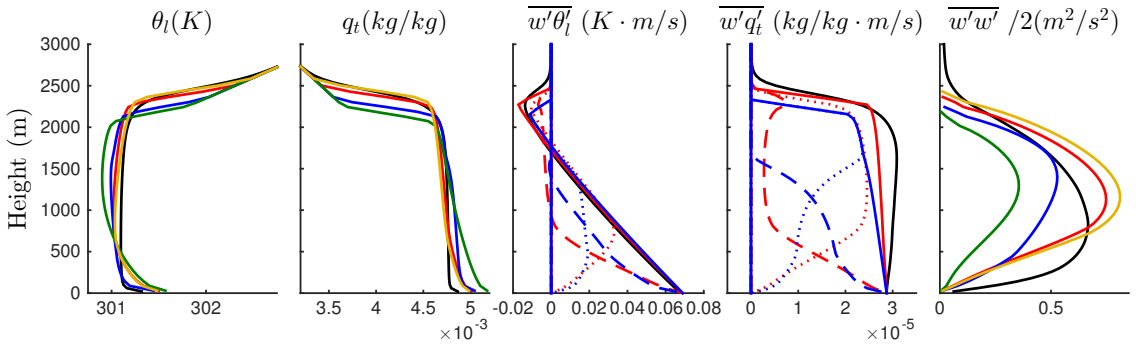


Figure 3.1: The hours 6-8 mean profiles of the dry-convective boundary layer test case. The fields of liquid water potential temperature $\theta_l$, total water specific humidity $q_t$, vertical turbulent fluxes of $\theta_l$ and $q_t$, and the variance of vertical velocity $\overline{w'w'}$ are shown. The SCM value of $\overline{w'w'}$ is reconstructed with parameterized updraft fraction and mass flux, assuming that the updraft is at the tail of the Gaussian distribution of vertical velocity. This is a fair assumption for dry convection. The default entrainment rate is $\epsilon = 0.8/z$. The colors correspond to different cases, i.e., LES (black), SCM control (red), K-profile diffusivity (blue), doubling entrainment rate $\epsilon = 1.6/z$ (green), and disabling the prognostic term (orange). The dashed and dotted lines represent fluxes by ED and MF, respectively.

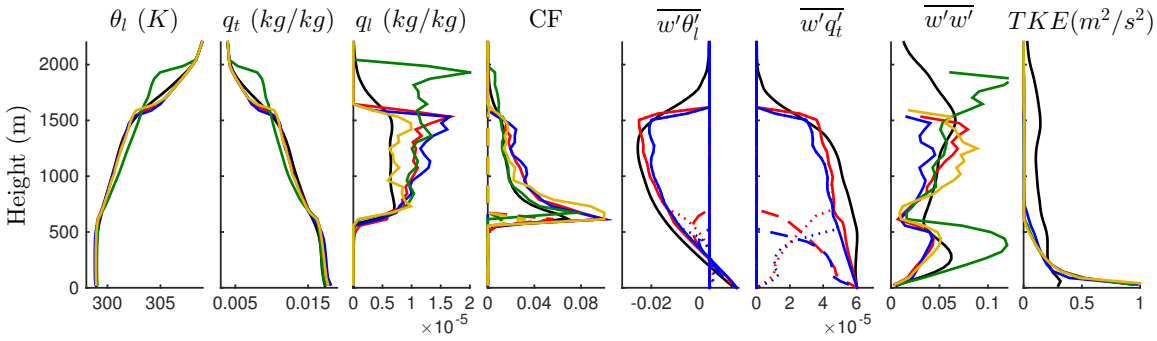


Figure 3.2: The hours 6-8 mean profiles of the BOMEX test case. Additional fields are shown for liquid water specific humidity $q_l$, cloud fraction (CF), and turbulent kinetic energy (TKE). The line colors and styles represent the corresponding sensitivity tests as Fig. 3.1, except that the default entrainment rate is $\epsilon = 1.6/z$, and the green lines represent the results with reduced entrainment rate of $\epsilon = 0.8/z$.

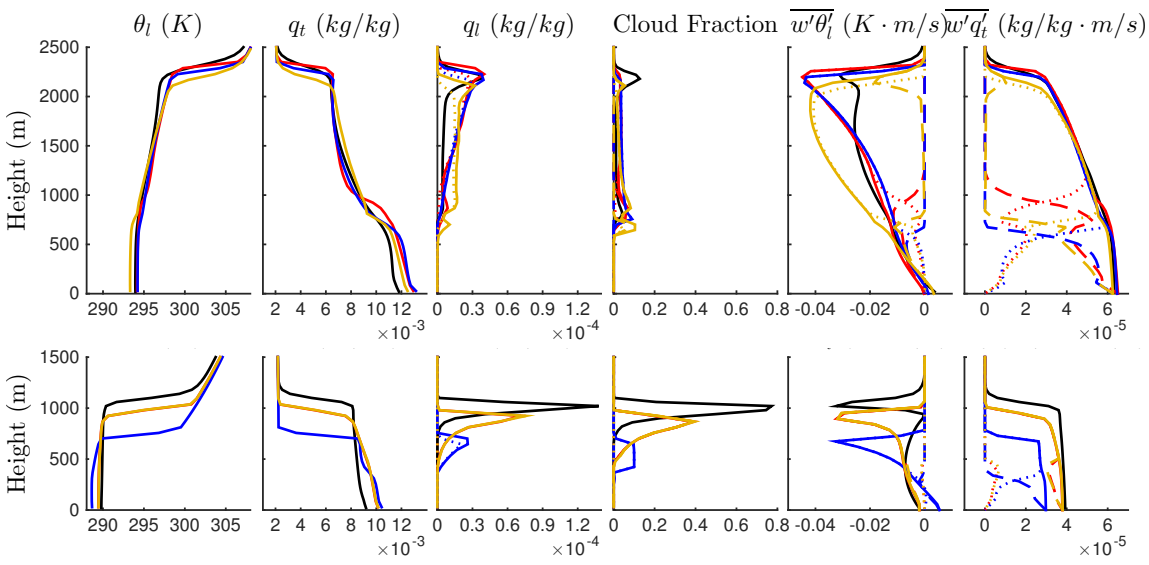


Figure 3.3: The days 8-10 profiles of the CGILS-like experiments of S12 (stratocumulus-like) case on the bottom and S6 (cumulus-like) case on the top. The line color and styles represent the corresponding sensitivity tests as in Fig. 3.2, except that the sensitivity test on entrainment rate is not performed. The x scales are set to be the same for both cases. Note that the profiles of S12 diagnostic updraft (orange) and prognostic updraft (red) cases overlap completely.

mixing produces a partially-cloudy layer that is also low and with only 10% cloud cover. The TKE-based diffusivity is able to maintain the vertical mixing by ED that dominates over the MF scheme, although it's still not strong enough compared to the LES, and the cloud top and cloud fraction are still too low. It should be noted that the MF-dominated regime is not completely unphysical, and it has been reported by Bretherton et al. (2010) that, under some conditions, multiple solutions may occur corresponding to either the Sc-regime or the low scattered cloud regime. The latter may be similar to the SCM result with k-profile diffusivity. Representing this transitional regime is actually a very challenging task for the EDMF scheme, and it will be interesting to investigate further whether the ED and MF component can interact sufficiently and self-adjust to simulate the complicated dynamics of multiple

equilibrium and hysteresis.

## 3.5 Discussion and Conclusion

In this chapter, an EDMF closure for the SGS turbulent and convective processes is presented, including both the EDMF framework of draft-environment decomposition and the closures for the key parameters in the EDMF scheme, such as eddy diffusivity and draft entrainment rate. The current formulation of EDMF scheme does not require the assumption of infinitesimal updraft fraction, and it retains the prognostic term which makes it applicable to the simulation at relatively high resolution and in non-equilibrium conditions. With applicable closures, it is also possible to close for the second-order moment equations consistently within the same framework.

SCM tests of the EDMF closure on various convection regimes are performed, and the results are compared to the LES. Most cases show reasonable agreement with the LES results, validating the potential for this scheme to represent the different cloud regimes. There are still, however, unresolved problems that requires further investigation, such as:

1. The MF component is too strongly dependent on the entrainment rate formulation, and its value seems to be regime-dependent. Improvements with regime-aware entrainment rate or multiple competing updrafts with different entrainment rates may help to resolve this problem.

2. The variance within the bulk updraft is not formulated in the current simplified

EDMF formulations. A relatively simple improvement will be to assume Gaussian distributions for draft variables, and predict the evolution of variances with the second-order moment equations.

3. The partition and transfer of TKE between environment and drafts are not well formulated. A better representation of variance exchange will help to improve the simulations of environmental TKE and scalar variances, as well as other variables that are linked to the probabilistic distributions, such as the cloud fraction and the liquid water content.

4. The downdrafts are not yet formulated. They are found in previous studies to be essential for deep convection, and they may also be important for the detrainment layer of shallow cumulus. Closures for downdraft initialization and evolution will be required for the parameterization of downdrafts.

The future development of the EDMF closure will go together with the experiments with the newly-developed PyCLES model. By exploring a large range of possible climate with PyCLES, the turbulence-convection processes can be better constrained and quantified. This is essential for the further development of the EDMF scheme and improvement of its closures. The EDMF scheme will also be implemented in an idealized GCM to investigate the robust mechanism for the cloud-circulation interaction and its response to the changing climate.

## 3.6 Appendix A: Theoretical deduction of the EDMF domain decomposition

### 3.6.1 Basic local equations

The *flux form* of the prognostic equation for a tracer $\phi$ is

$$\frac{\partial(\rho\phi)}{\partial t} + \nabla_h \cdot (\rho\phi \mathbf{u}_h) + \frac{\partial(\rho\phi w)}{\partial z} = \rho S_\phi, \tag{3.49}$$

where $\nabla_h = (\partial_x, \partial_y)$ is the gradient operator in the horizontal plane, $\mathbf{u}_h = (u, v)$ is the velocity vector in the horizontal plane, and $S_\phi$ represents additional source/sink terms of $\phi$ per unit time.

With $\phi \equiv 1$, we can deduce the *continuity equation* as:

$$\frac{\partial\rho}{\partial t} + \nabla_h \cdot (\rho \mathbf{u}_h) + \frac{\partial(\rho w)}{\partial z} = 0. \tag{3.50}$$

Combining these equations, we can deduce the *advection form* of this equation as

$$\frac{\partial\phi}{\partial t} + \mathbf{u}_h \cdot \nabla_h \phi + w \cdot \frac{\partial\phi}{\partial z} = S_\phi. \tag{3.51}$$

### 3.6.2 Area integral

Now we can integrate the flux form equation on an arbitrary area $A(z,t)$ at any given height $z$ and time $t$. The integrated flux form equation is:

$$\int_{A(z,t)} \frac{\partial(\rho\phi)}{\partial t} dA + \int_{A(z,t)} \nabla_h \cdot (\rho\phi \mathbf{u}_h) dA + \int_{A(z,t)} \frac{\partial(\rho\phi w)}{\partial z} dA = \int_{A(z,t)} \rho S_\phi dA. \quad (3.52)$$

The following notations are introduced:

$$\text{Area-weighted average: } \overline{\chi}_u = \frac{\int_A \chi dA}{\int_A dA}; \quad (3.53)$$

$$\text{Mass-weighted average: } \overline{\chi}^u = \frac{\int_A \rho\chi dA}{\int_A \rho dA}. \quad (3.54)$$

Using the divergence theorem, the second term of equation (3.52) can be rewritten as

$$\int_A \nabla_h \cdot (\rho\phi \mathbf{u}_h) dA = \oint_{\partial A} \rho\phi \mathbf{u}_h \cdot \mathbf{n} dl, \quad (3.55)$$

where $\mathbf{n}$ is the outward-pointing unit normal vector of the boundary $\partial A$.

The first term can be rewritten with the Reynolds' Transport Theorem:

$$\frac{\partial}{\partial t} \int_{A(z,t)} \rho\phi dA = \int_{A(z,t)} \frac{\partial(\rho\phi)}{\partial t} dA + \int_{\partial A} \rho\phi \mathbf{u}_b \cdot \mathbf{n} dA, \quad (3.56)$$

where $\mathbf{u}_b$ is a vector in the horizontal plane representing the change of the boundary per unit time (i.e., velocity of the boundary) for a fixed height $z$.

The third term can be rewritten in a similar way as

$$\frac{\partial}{\partial z}\int_{A(z,t)}\rho\phi w dA = \int_{A(z,t)}\frac{\partial(\rho\phi w)}{\partial z}dA + \int_{\partial A}\rho\phi w\mathbf{u}_z\cdot\mathbf{n}dA, \tag{3.57}$$

where $\mathbf{u}_z$ is a vector in the horizontal plane, representing the change of the boundary per unit height at the fixed time $t$.

Therefore, equation (3.52) can be written as

$$\frac{\partial}{\partial t}\int_{A(z,t)}\rho\phi dA+\frac{\partial}{\partial z}\int_{A(z,t)}\rho\phi w dA+\oint_{\partial A}\rho\phi(\mathbf{u}_h-\mathbf{u}_b-w\mathbf{u}_z)\cdot\mathbf{n}dl = \int_{A(z,t)}\rho S_\phi dA. \tag{3.58}$$

Using notations (3.53) (3.54), this can be rewritten as

$$\frac{\partial}{\partial t}(A\overline{\rho}_u\overline{\phi}^u) + \frac{\partial}{\partial z}(A\overline{\rho}_u\overline{w\phi}^u) + \oint_{\partial A}\rho\phi(\mathbf{u}_h-\mathbf{u}_b-w\mathbf{u}_z)\cdot\mathbf{n}dl = A\overline{\rho}_u\overline{S}^u_\phi. \tag{3.59}$$

Now let's focus on the third term of this equation. Note that for a boundary point within a short period of time $dt$, its horizontal displacement is $\mathbf{u}_h dt$, the horizontal displacement for the boundary at fixed height $z$ is $\mathbf{u}_b dt$, and the horizontal difference of the boundary related to vertical motion is $(wdt)\mathbf{u}_z$. The requirement that the boundary point remains at the boundary is as follows:

$$(\mathbf{u}_h dt - wdt\mathbf{u}_z - \mathbf{u}_b dt)\perp\mathbf{n}, \quad \text{i.e., } (\mathbf{u}_h - w\mathbf{u}_z - \mathbf{u}_b)\cdot\mathbf{n} = 0. \tag{3.60}$$

Thus, the third term physically represents the entrainment and detrainment processes. If the boundary evolves with the flow, i.e., there is neither entrainment nor

detrainment, the third term is always 0. We can denote the flow velocity relative to the boundary as $\mathbf{u}_r$, i.e,

$$\mathbf{u}_r = \mathbf{u}_h - w\mathbf{u}_z - \mathbf{u}_b.$$

When $\mathbf{u}_r \cdot \mathbf{n} > 0$, there is flow out of the boundary, i.e., detrainment; when $\mathbf{u}_r \cdot \mathbf{n} < 0$, there is flow out of the boundary, i.e., entrainment.

This form is equivalent to Siebesma (1998),

$$\frac{\partial}{\partial t}(A\overline{\rho}_u\overline{\phi}^u) + \frac{\partial}{\partial z}(A\overline{\rho}_u\overline{w\phi}^u) + \oint_{\partial A}\rho\phi(\mathbf{u}-\mathbf{u}_b)\cdot\hat{\mathbf{n}}dl = A\overline{\rho}_u\overline{S}^u_\phi, \tag{3.61}$$

where $\mathbf{u}$ is the full 3D velocity vector, and $\hat{\mathbf{n}}$ is the normal vector of $\partial A$ in the 3D space. $\hat{\mathbf{n}}$ may not lie in the horizontal plane or be of unit length, but its horizontal component should be of unit length.

Taking $\phi \equiv 1$ again, we can deduce the *mass-flux continuity equation* as:

$$\frac{\partial}{\partial t}(A\overline{\rho}_u) + \frac{\partial}{\partial z}(A\overline{\rho}_u\overline{w}^u) - \overline{\rho}_E E + \overline{\rho}_D D = 0, \tag{3.62}$$

where the entrainment $E$ and detrainment $D$ are defined as

$$E = -\oint_{\partial A:\mathbf{u}_r\cdot\mathbf{n}<0}\mathbf{u}_r\cdot\mathbf{n}dl, \quad D = \oint_{\partial A:\mathbf{u}_r\cdot\mathbf{n}>0}\mathbf{u}_r\cdot\mathbf{n}dl. \tag{3.63}$$

$\overline{\chi}_E$, $\overline{\chi}_D$ are length-weighted averages of $\chi$ at the entraining/detraining boundaries; $\overline{\chi}^E$, $\overline{\chi}^D$ are corresponding mass-weighted averages.

Equation (3.59) can be rewritten as (*flux form of mass-flux tracer equation*)

$$\frac{\partial}{\partial t}(A\overline{\rho}_u\overline{\phi}^u) + \frac{\partial}{\partial z}(A\overline{\rho}_u\overline{w\phi}^u) - \overline{\rho}_E\overline{\phi}^E E + \overline{\rho}_D\overline{\phi}^D D = A\overline{\rho}_u\overline{S}^u_\phi. \tag{3.64}$$

Combining equations (3.59) and (3.64), we can deduce the *advection form of mass-flux tracer equation* as:

$$A\overline{\rho}_u\frac{\partial\overline{\phi}^u}{\partial t} + A\overline{\rho}_u\overline{w}^u\frac{\partial\overline{\phi}^u}{\partial z} + \frac{\partial}{\partial z}(A\rho_u\overline{w'\phi'}^u) - \overline{\rho}_E E(\overline{\phi}^E - \overline{\phi}^u) + \overline{\rho}_D D(\overline{\phi}^D - \overline{\phi}^u) = A\overline{\rho}_u\overline{S}^u_\phi, \tag{3.65}$$

i.e.,

$$\frac{\partial\overline{\phi}^u}{\partial t} + \overline{w}^u\frac{\partial\overline{\phi}^u}{\partial z} + \frac{1}{A\overline{\rho}_u}\frac{\partial}{\partial z}(A\overline{\rho}_u\overline{w'\phi'}^u) - \frac{E\overline{\rho}_E}{A\overline{\rho}_u}(\overline{\phi}^E - \overline{\phi}^u) + \frac{D\overline{\rho}_D}{A\overline{\rho}_u}(\overline{\phi}^D - \overline{\phi}^u) = \overline{S}^u_\phi, \tag{3.66}$$

where $\overline{w'\phi'}^u = \overline{w\phi}^u - \overline{w}^u\overline{\phi}^u$.

Normally, we ignore the horizontal density fluctuation, i.e., $\overline{\rho}_E = \overline{\rho}_D = \overline{\rho}_u = \overline{\rho}$, which effectively makes the anelastic approximation, and thus the area weighted average is the same as mass-weighted average ($\overline{\chi}_X = \overline{\chi}^X$). Thus equations (3.62) and (3.66) can be simplified as

$$\frac{\partial}{\partial t}(A\overline{\rho}) + \frac{\partial}{\partial z}(A\overline{\rho}\ \overline{w}^u) = \overline{\rho}(E - D), \tag{3.67}$$

$$\frac{\partial\overline{\phi}^u}{\partial t} + \overline{w}^u\frac{\partial\overline{\phi}^u}{\partial z} + \frac{1}{A\overline{\rho}}\frac{\partial}{\partial z}(A\rho\overline{w'\phi'}^u) = \frac{E}{A}(\overline{\phi}^E - \overline{\phi}^u) - \frac{D}{A}(\overline{\phi}^D - \overline{\phi}^u) + \overline{S}^u_\phi. \tag{3.68}$$

We may further define mass flux $M$, entrainment rate $\epsilon$, and detrainment rate $\delta$

as follows:

$$M = \overline{\rho} A \overline{w}^u, \quad \epsilon = \frac{E}{A\overline{w}^u}, \quad \delta = \frac{D}{A\overline{w}^u}. \tag{3.69}$$

Thus the above equations can be written in the more familiar forms:

$$\frac{\partial}{\partial t}\Big(\frac{M}{\overline{w}^u}\Big) + \frac{\partial M}{\partial z} = M(\epsilon - \delta), \tag{3.70}$$

$$\frac{1}{\overline{w}^u}\frac{\partial \overline{\phi}^u}{\partial t} + \frac{\partial \overline{\phi}^u}{\partial z} = \epsilon(\overline{\phi}^E - \overline{\phi}^u) - \delta(\overline{\phi}^D - \overline{\phi}^u) - \frac{1}{M}\frac{\partial}{\partial z}(\frac{M}{\overline{w}^u}\overline{w'\phi'}^u) + \frac{\overline{S}^u_\phi}{\overline{w}^u}. \tag{3.71}$$

*Remark:* The classical forms of these updraft equations are obtained with further assumptions of time-invariance ($\partial/\partial t = 0$) and homogeneity of updraft ($\overline{\phi}^D = \overline{\phi}^u$, and $\overline{w'\phi'}^u = 0$). The corresponding equations are

$$\frac{\partial M}{\partial z} = M(\epsilon - \delta), \tag{3.72}$$

$$\frac{\partial \overline{\phi}^u}{\partial z} = \epsilon(\overline{\phi}^E - \overline{\phi}^u) + \frac{\overline{S}^u_\phi}{\overline{w}^u}. \tag{3.73}$$

### 3.6.3 Ensemble of areas

For a given area $A_T$ (e.g., a grid box in the GCM), we can do an arbitrary division $\{A_1, A_2, \cdots, A_n\}$, such that $\bigcup_i A_i = A_T$. The equation (3.64) for an area $A_i$ is

$$\frac{\partial}{\partial t}(A_i\overline{\rho}_i\overline{\phi}^i) + \frac{\partial}{\partial z}(A_i\overline{\rho}_i\overline{w\phi}^i) - \overline{\rho}_{E_i}\overline{\phi}^{E_i}E_i + \overline{\rho}_{D_i}\overline{\phi}^{D_i}D_i = A_i\overline{\rho}_i\overline{S}^i_\phi \tag{3.74}$$

The entrainment and detrainment terms can be further decomposed as follows:

$$\overline{\rho}_{E_i}\overline{\phi}^{E_i}E_i = \sum_{i\neq j}\overline{\rho}_{E_{ij}}\overline{\phi}^{E_{ij}}E_{ij} + \overline{\rho}_{E_{io}}\overline{\phi}^{E_{io}}E_{io}, \tag{3.75}$$

$$\overline{\rho}_{D_i}\overline{\phi}^{D_i}D_i = \sum_{i\neq j}\overline{\rho}_{D_{ij}}\overline{\phi}^{D_{ij}}D_{ij} + \overline{\rho}_{D_{io}}\overline{\phi}^{D_{io}}D_{io}, \tag{3.76}$$

where $E_{ij}$ and $D_{ij}$ represent the entrainment and detrainment between $A_i$ and $A_j$, and $E_{io}$ and $D_{io}$ represent the entrainment and detrainment between $A_i$ and the external area (e.g., the neighbouring grid boxes). Note that the normal vector $\mathbf{n}$ (or $\hat{\mathbf{n}}$) is opposite for the neighbouring areas $A_i$ and $A_j$, while the vectors $\mathbf{u}_h$, $\mathbf{u}_b$, $\mathbf{u}_z$, $\mathbf{u}$ are the same. Thus it is natural that

$$\overline{\rho}_{E_{ij}}\overline{\phi}^{E_{ij}}E_{ij} = \overline{\rho}_{D_{ji}}\overline{\phi}^{D_{ji}}D_{ji}. \tag{3.77}$$

Therefore, we get naturally the tracer equation for the total area $A_T$ by summing equation (3.74) over all $i$,

$$\frac{\partial}{\partial t}(A_T\overline{\rho}_T\overline{\phi}^T) + \frac{\partial}{\partial z}(A_T\overline{\rho}_T\overline{w\phi}^T) - \overline{\rho}_{E_T}\overline{\phi}^{E_T}E_T + \overline{\rho}_{D_T}\overline{\phi}^{D_T}D_T = A_T\overline{\rho}_T\overline{S}_\phi^T, \tag{3.78}$$

in which we have used

$$A_T\overline{\rho}_T\overline{\chi}^T = \int_{A_T}\rho\chi dA = \sum_i\int_{A_i}\rho\chi dA = \sum_i(A_i\overline{\rho}_i\overline{\chi}^i), \tag{3.79}$$

and similarly,

$$\overline{\rho}_{E_T}\overline{\phi}^{E_T}E_T = \sum_i(\overline{\rho}_{E_{io}}\overline{\phi}^{E_{io}}E_{io}), \quad \overline{\rho}_{D_T}\overline{\phi}^{D_T}D_T = \sum_i(\overline{\rho}_{D_{io}}\overline{\phi}^{D_{io}}D_{io}). \tag{3.80}$$

Note that if $A_T$ is a constant vertical column (e.g., GCM grid-box), $\mathbf{u}_b = 0, \mathbf{u}_z = 0$, and thus

$$-\overline{\rho}_{E_T}\overline{\phi}^{E_T}E_T + \overline{\rho}_{D_T}\overline{\phi}^{D_T}D_T = \oint_{\partial A_T}\rho\phi\mathbf{u}_h\cdot\mathbf{n}dl = \int_{A_T}\nabla_h\cdot(\rho\phi\mathbf{u}_h)dA. \tag{3.81}$$

This is consistent with the common form of the tracer equation for $A_T$, where the horizontal advection term corresponds to the total net entrainment/detrainment terms.

### 3.6.4 Environment, drafts, and grid-box mean

Taking $\chi = w$ in equation (3.79), and using notation $M_i = \overline{\rho}_i A_i \overline{w}^i$, we have

$$M_T = A_T\overline{\rho}_T\overline{w}^T = \sum_i(A_i\overline{\rho}_i\overline{w}^i) = \sum_i M_i. \tag{3.82}$$

And further assuming that $A_T$ is a constant vertical column, so equation (3.81) applies. By decomposing $\overline{w\phi}^i = \overline{w}^i\overline{\phi}^i + \overline{w'\phi'}^i$, we can rewrite equation (3.78) as

$$A_T\frac{\partial}{\partial t}(\overline{\rho}_T\overline{\phi}^T) + \frac{\partial}{\partial z}\sum_i(M_i\overline{\phi}^i + A_i\overline{\rho}_i\overline{w'\phi'}^i) + A_T\overline{[\nabla_h\cdot(\rho\phi\mathbf{u}_h)]}_T = A_T\overline{\rho}_T\overline{S}_\phi^T. \tag{3.83}$$

Denoting $a_i = A_i/A_T$ representing the area fraction of each $A_i$, and denoting

$m_i = M_i/A_T = \overline{\rho}_i a_i \overline{w}^i$, $m_T = M_T/A_T = \overline{\rho}_T \overline{w}^T$, we have

$$\frac{\partial}{\partial t}(\overline{\rho}_T \overline{\phi}^T) + \frac{\partial}{\partial z}(\overline{\rho}_T \overline{w}^T \overline{\phi}^T) + \overline{[\nabla_h \cdot (\rho\phi \mathbf{u}_h)]}_T = -\frac{\partial}{\partial z} \sum_i \left( m_i(\overline{\phi}^i - \overline{\phi}^T) + a_i \overline{\rho}_i \overline{w'\phi'}^i \right) + \overline{\rho}_T \overline{S}^T_\phi. \tag{3.84}$$

Here, the three terms on the left represent time-tendency, grid-scale vertical flux, and grid-scale horizontal flux. On the right, the two terms of the summation are respectively mean and turbulent flux in the sub-area $A_i$, usually interpreted as *'mass-flux'* term and *'eddy-diffusion'* term; the last term represents all additional sources and sinks of $\phi$.

Equations (3.84) is the *flux form of the grid-box mean tracer equations.* Now we can also deduce the *advection form of the grid-box mean tracer equations* by combining these equations with the mass-flux continuity equation

$$\frac{\partial}{\partial t}(\overline{\rho}_T) + \frac{\partial}{\partial z}(\overline{\rho}_T \overline{w}^T) + \overline{[\nabla_h \cdot (\rho \mathbf{u}_h)]}_T = 0, \tag{3.85}$$

and the results are:

$$\frac{\partial \overline{\phi}^T}{\partial t} + \overline{w}^T \frac{\partial \overline{\phi}^T}{\partial z} + \frac{1}{\overline{\rho}_T} \overline{\left[\nabla_h \cdot (\rho(\phi - \overline{\phi}^T)\mathbf{u}_h)\right]}_T = -\frac{1}{\overline{\rho}_T} \frac{\partial}{\partial z} \sum_i \left( m_i(\overline{\phi}^i - \overline{\phi}^T) + a_i \overline{\rho}_i \overline{w'\phi'}^i \right) + \overline{S}^T_\phi. \tag{3.86}$$

The third term on the left can be rewritten as

$$\begin{aligned}
&\frac{1}{\overline{\rho}_T}\overline{\Big[\nabla_h\cdot(\rho(\phi-\overline{\phi}^T)\mathbf{u}_h)\Big]}_T \\
&=\frac{1}{\overline{\rho}_T}\int_{a_T}\nabla_h\cdot(\rho(\phi-\overline{\phi}^T)\mathbf{u}_h)da \\
&=\frac{1}{\overline{\rho}_T}\int_{a_T}\Big[\rho\Big((\phi-\overline{\phi}^T)\nabla_h\cdot\mathbf{u}_h+\mathbf{u}_h\cdot\nabla_h\phi\Big)+(\phi-\overline{\phi}^T)\mathbf{u}_h\cdot\nabla_h\rho\Big]da \\
&=\overline{\mathbf{u}_h}^T\cdot\overline{\nabla_h\phi}^T+\overline{\nabla_h\cdot(\phi'\mathbf{u}_h')}^T+\frac{1}{\overline{\rho}_T}\int_{a_T}(\phi-\overline{\phi}^T)\mathbf{u}_h\cdot\nabla_h\rho da, \qquad (3.87)
\end{aligned}$$

where the first term represents the mean horizontal advection (mean velocity multiplying mean gradient), the second term represents turbulent horizontal advection, and the third term represents additional advective tendency due to inhomogeneous density.

Normally, we ignore the horizontal eddy transport across the boundary of the grid box, and the third term is much smaller than the first term since $\rho'/\overline{\rho}\ll 1$, thus only the first term in the equation (3.87) is kept. Thus the grid-box mean tendency equation (3.86) can be simplified as

$$\frac{\partial\overline{\phi}^T}{\partial t}+\overline{w}^T\frac{\partial\overline{\phi}^T}{\partial z}+\overline{\mathbf{u}_h}^T\cdot\overline{\nabla_h\phi}^T=-\frac{1}{\overline{\rho}_T}\frac{\partial}{\partial z}\sum_i\Big(m_i(\overline{\phi}^i-\overline{\phi}^T)+a_i\overline{\rho}_i\overline{w'\phi'}^i\Big)+\overline{S}_\phi^T. \quad (3.88)$$

Further ignoring the horizontal density fluctuation in the grid-box, i.e., $\overline{\rho}_T=\overline{\rho}_i$, we have

$$\frac{\partial\overline{\phi}^T}{\partial t}+\overline{w}^T\frac{\partial\overline{\phi}^T}{\partial z}+\overline{\mathbf{u}_h}^T\cdot\overline{\nabla_h\phi}^T=-\frac{1}{\overline{\rho}}\frac{\partial}{\partial z}\sum_i\Big(m_i(\overline{\phi}^i-\overline{\phi}^T)+a_i\overline{\rho}\overline{w'\phi'}^i\Big)+\overline{S}_\phi^T. \quad (3.89)$$

Another commonly used equation is derived from the time-averaged flux-form environmental tracer equation:

$$\frac{\partial}{\partial t}(A_n\overline{\rho}_n\overline{\phi}^n) + \frac{\partial}{\partial z}(A_n\overline{\rho}_n\overline{w\phi}^n) - \overline{\rho}_{E_n}\overline{\phi}^{E_n}E_n + \overline{\rho}_{D_n}\overline{\phi}^{D_n}D_n = A_n\overline{\rho}_n\overline{S}^n_\phi. \tag{3.90}$$

Using equations (3.80) (3.81), and assuming that (1) $\rho$ is horizontally uniform, (2) $\phi^{D_i} = \phi^i$, and (3) no direct mass exchange between updrafts, or between updrafts and the neighbouring grid-boxes ($\phi^{E_i} = \phi^n$ when $i \neq n$), the above equation can be rewritten as (divided over $A_T$):

$$\begin{aligned}&\frac{\partial}{\partial t}(a_n\overline{\rho}\overline{\phi}^n) + \overline{\nabla_h\cdot(\rho\phi\mathbf{u}_h)}^T + \frac{\partial}{\partial z}\Big(\overline{\rho}(\overline{w}^T - \sum_{i\neq n}a_i\overline{w}^i)\overline{\phi}^n\Big)\\ &= \sum_{i\neq n}\Big(m_i\delta_i\overline{\phi}^i - m_i\epsilon_i\overline{\phi}^n\Big) - \frac{\partial}{\partial z}(a_n\overline{\rho}\overline{w'\phi'}^n) + \overline{\rho}a_n\overline{S}^n_\phi.\end{aligned} \tag{3.91}$$

Using Equation (41) and the approximation that $\rho'/\overline{\rho} \ll 1$ and horizontal eddy transport is negligible, we have

$$\overline{\nabla_h\cdot(\rho\phi\mathbf{u}_h)}^T \approx \overline{\rho}\ \overline{\mathbf{u}_h}^T\cdot\overline{\nabla_h\phi}^T + \overline{\phi}^T\overline{\nabla_h\cdot(\rho\mathbf{u}_h)}^T. \tag{3.92}$$

Along with equation (3.85), equation (3.91) is thus

$$\begin{aligned}&\overline{\rho}\frac{\partial\overline{\phi}^T}{\partial t} + \frac{\partial}{\partial t}\Big(\overline{\rho}(a_n\overline{\phi}^n - \overline{\phi}^T)\Big) + \overline{\rho}\ \overline{\mathbf{u}_h}^T\cdot\overline{\nabla_h\phi}^T + \overline{\rho}\ \overline{w}^T\frac{\partial\phi^T}{\partial z} + \frac{\partial}{\partial z}\Big(\overline{\rho}\ \overline{w}^T(\overline{\phi}^n - \overline{\phi}^T)\Big)\\ &= \sum_{i\neq n}\Big(m_i\delta_i\overline{\phi}^i - m_i\epsilon_i\overline{\phi}^n + \frac{\partial}{\partial z}m_i\overline{\phi}^n\Big) - \frac{\partial}{\partial z}(a_n\overline{\rho}\overline{w'\phi'}^n) + \overline{\rho}a_n\overline{S}^n_\phi.\end{aligned} \tag{3.93}$$

The above assumption (3) is satisfied if $a_n \approx 1$, but not necessarily so. If we further explicitly assume that $a_n \approx 1$ (i.e., updraft fractions are small), thus $\overline{\chi}^n \approx \overline{\chi}^T$ (except for the source term $S_\phi$). Thus the second and fifth terms on the left hand side are neglected, and equation (3.91) becomes

$$\frac{\partial \overline{\phi}^T}{\partial t}+\overline{w}^T\frac{\partial \overline{\phi}^T}{\partial z}+\overline{\mathbf{u}_h}^T\cdot\overline{\nabla_h\phi}^T = -\frac{1}{\overline{\rho}}\frac{\partial}{\partial z}\Big(-\sum_{i\neq n}(m_i\overline{\phi}^T)+\overline{\rho}\overline{w'\phi'}^n\Big)+\frac{1}{\overline{\rho}}\sum_{i\neq n}\Big(m_i\delta_i\overline{\phi}^i-m_i\epsilon_i\overline{\phi}^T\Big)+\overline{S}^n_\phi. \tag{3.94}$$

Note that due to the assumptions of $a_n \approx 1$ and $\overline{\phi}_n \approx \overline{\phi}^T$, the tracer conservation does not hold strictly. Therefore, the equation (3.89) is preferred and used in the following parts.

### 3.6.5 Summary of equations

The equations (3.62, 3.66) are the exact equations of a single updraft, and the equations (3.85, 3.86) are the exact equations of a fixed area (grid-box). We can further make two common assumptions: (1) horizontal density fluctuation and gradient are negligible, and (2) horizontal turbulent fluxes can be neglected. Thus we can get equations (3.70, 3.71, 3.89), i.e.,

$$\frac{\partial}{\partial t}\Big(\frac{m_i}{\overline{w}^i}\Big)+\frac{\partial m_i}{\partial z} = m_i(\epsilon_i-\delta_i), \tag{3.70}$$

$$\frac{1}{\overline{w}^i}\frac{\partial \overline{\phi}^i}{\partial t}+\frac{\partial \overline{\phi}^i}{\partial z} = \epsilon_i(\overline{\phi}^{E_i}-\overline{\phi}^i)-\delta_i(\overline{\phi}^{D_i}-\overline{\phi}^i)-\frac{1}{m_i}\frac{\partial}{\partial z}(\frac{m_i}{\overline{w}^i}\overline{w'\phi'}^i)+\frac{\overline{S}^i_\phi}{\overline{w}^i}, \tag{3.71}$$

$$\frac{\partial \overline{\phi}^T}{\partial t}+\overline{w}^T\frac{\partial \overline{\phi}^T}{\partial z}+\overline{\mathbf{u}_h}^T\cdot\overline{\nabla_h\phi}^T = -\frac{1}{\overline{\rho}}\frac{\partial}{\partial z}\sum_i\Big(m_i(\overline{\phi}^i-\overline{\phi}^T)+a_i\overline{\rho}\overline{w'\phi'}^i\Big)+\overline{S}^T_\phi. \tag{3.89}$$

Note that the updraft equations have been rewritten specifically for area $A_i$. In order to solve the updraft equations, we need initial and boundary conditions for $m_i and \overline{w}^i$, as well as closures for $\overline{w}^i$, $\epsilon_i$, $\delta_i$, $\overline{\phi}^{E_i}$, $\overline{\phi}^{D_i}$, $\overline{w'\phi'}^i$, and $\overline{S}^i_\phi$. After solving $m_i$, $\overline{w}^i$, $\overline{w'\phi'}^i$, and $\overline{\phi}^i$, we can compute the first term on the right-hand side of equation (3.89), which is exactly the forcing due to convective and turbulent processes. The second term $S^T_\phi$ can also be computed by summing $\overline{S}^i_\phi$. The large-scale advection terms on the left-hand side of equation (3.89) is solved by the dynamical core of the GCM.

Equation (3.89) can be averaged over an arbitrary time interval (denoted by $\langle\cdot\rangle$). And in models, the variation of density within a time step is often neglected. If we also neglect the fluctuating components of large-scale advection and the $\overline{\phi}^i - \overline{\phi}^T$ term, the equation can be simplified as

$$\frac{\partial\langle\overline{\phi}^T\rangle}{\partial t} + \langle\overline{w}^T\rangle\left\langle\frac{\partial\overline{\phi}^T}{\partial z}\right\rangle + \langle\overline{\mathbf{u}_h}^T\rangle\cdot\langle\overline{\nabla_h\phi}^T\rangle = -\frac{1}{\overline{\rho}}\frac{\partial}{\partial z}\sum_i\left(\langle m_i\rangle\langle\overline{\phi}^i - \overline{\phi}^T\rangle + \overline{\rho}\langle a_i\overline{w'\phi'}^i\rangle\right) + \langle\overline{S}^T_\phi\rangle. \tag{3.95}$$

With this assumption, it suffices to know the time-averaged mass-flux and tracer anomaly within updrafts. This assumption holds when the convection is in quasi-equilibrium with the environment, i.e., the convective tendencies are mostly balancing the large-scale advective and the diabatic tendencies, so the environmental conditions are only evolving slowly and the time-variations of updraft parameters are small. This is often used in models along with assumptions that the time-dependent terms in equations (3.70) and (3.71) can also be neglected. As is shown in Section 3.3, this diagnostic mass-flux may not be consistent with the mass-flux required to alter the

updraft conditions, especially when the updraft is slow but occupies a non-negligible area fraction.

## 3.7 Appendix B: Numerical implementation

### 3.7.1 Discretization of the updraft equations

For each of the updrafts, the governing equations are the updraft velocity equation (3.16), the updraft continuity equation (3.70), and the tracer equations (3.71). The updraft velocity equation is written in advection form, so it is decoupled from the other equations and solved in the first place. The updraft continuity and tracer equations are then solved in flux form, which ensures the numerical conservation of mass and tracers. The equations are listed as follows:

$$\frac{\partial w^i}{\partial t} + \frac{1}{2}\frac{\partial (w^i)^2}{\partial z} = aB_u^i + b\epsilon_i w^i (w^n - w^i), \tag{3.96}$$

$$\frac{\partial}{\partial t}(\rho a_i) + \frac{\partial}{\partial z}(\rho a_i w^i) = \rho a_i w^i (\epsilon_i - \delta_i), \tag{3.97}$$

$$\frac{\partial}{\partial t}(\rho a_i \phi^i) + \frac{\partial}{\partial z}(\rho a_i w^i \phi^i) = \rho a_i w^i (\epsilon_i \phi^n - \delta_i \phi^i) + \rho a_i S_\phi^i. \tag{3.98}$$

These equations are integrated with the upwind-flux discretization in the vertical direction to ensure numerical stability. All values are defined at the full model levels, so there is no grid-staggering. In the time-discretization, the density $\rho$, the environmental mean variables $w^n, \phi^n$ and the entrainment/detrainment rates $\epsilon_i, \delta_i$ are computed explicitly (i.e., taken directly from the input), but the updraft variables as $w^i$, $a_i$, and $a_i\phi^i$ are computed implicitly. The source terms $S_\phi^i$ are not computed

concurrently with the integration, but are diagnosed after the computation for each level is done.

Note that the input for the scheme includes the grid-mean variables $\phi^T$ and the updraft variables $\phi^i$ and $a_i$ from the previous time step ($t = t_0$), so we need to compute for the environmental variables with the following equations:

$$a_n = 1 - \sum_{i \neq n} a_i, \quad \phi^n = \frac{1}{a_n}\Big(\phi^T - a_i \phi^i\Big). \tag{3.99}$$

This can be numerically unstable if the updraft fractions are not small, i.e., $a_n \to 0$. Especially, in the GCM, the updraft is only advected vertically by the following scheme, without feeling the other effects like horizontal advection and radiation; the grid-box mean is handled by the GCM dynamical core, which has a different vertical advection scheme and also spatial and time filters. Thus the discretized form of equations for $\phi^i$ and $\phi^T$ may not be consistent, which may result in errors or even instabilities of $\phi^n$. If the updrafts are actively interacting with the environment, the entrainment/detrainment mixing may reduce the discrepancies between the numerical integration methods for the updraft and the environment. The validity of this assumption needs to be further tested.

The details of discretization scheme for updrafts are as follows.

#### 3.7.1.1 Velocity equation

The equation is integrated from bottom to top. The vertical velocities $W^i$ and $W^n$ are evaluated at half-levels ($\ldots, z_{-/2}, z_{+/2}, z_{+3/2}, \ldots$), and all other variables are evaluated

at full levels $(\ldots, z_-, z_o, z_+, \ldots)$.

Knowing all values at the last time step $(t_o)$ or at lower levels of the current time step $(t_N, z_{+/2})$, the equation can be discretized as follows, with the values at $(t_N, z_{+3/2})$ unknown:

$$\frac{W^i(z_{+3/2}, t_N) - W^i(z_{+3/2}, t_o)}{\Delta t} + \frac{(W^i(z_{+3/2}, t_N))^2 - (W^i(z_{+/2}, t_N))^2}{2\Delta z_{++}}$$
$$= aB_u^i(z_+, t_o) + b\epsilon_i(z_+, t_o)W^i(z_{+3/2}, t_N)\big(W^n(z_{+3/2}, t_o) - W^i(z_{+3/2}, t_N)\big), \quad (3.100)$$

where $\Delta t = t_N - t_o, \Delta z = z_{+3/2} - z_{+/2}$. Note the implicit formulation (using $t_N$ values for $W^i$ except for the first term) and upwind discretization (using fluxes evaluated at $z_+$ and $z_o$ in the second term). The buoyancy term $B_u^i$ is evaluated at the old time step, which is not ideal, but doing it implicitly would require values of updraft tracers at the new time step, which re-couples the velocity equation to the other equations and greatly increase the numerical complexity. Alternatively we may include a correction term related to $B_u^i(z_o, t_N)$ to make it semi-implicit. The exact formulation is left for future development.

For simplicity, let's denote $(z_{+3/2}, t_N)$ for $W$, and $(z_+, t_N)$ for other variables simply as subscript $+, N$; and similarly for other values. We also omit the subscript $(+, o)$ for $B_u^i$ and $\epsilon_i$. This equation is then written as

$$\frac{W^i_{+,N} - W^i_{+,o}}{\Delta t} + \frac{(W^i_{+,N})^2 - (W^i_{o,N})^2}{2\Delta z} = aB_u^i + b\epsilon_i W^i_{+,N}\big(W^n_{+,o} - W^i_{+,N}\big). \quad (3.101)$$

This is a quadratic equation of $W^i_{+,N}$ and can be solved as

$$W^i_{+,N} = \frac{-W_\alpha + \sqrt{W_\alpha^2 + W_\beta^2}}{1 + 2b\epsilon_i \Delta z}, \tag{3.102}$$

where

$$W_\alpha = \frac{\Delta z}{\Delta t} - bW^n_{+,o} \cdot \epsilon_i \Delta z, \tag{3.103}$$

$$W_\beta^2 = (1 + 2b\epsilon_i \Delta z)\Big((W^i_{o,N})^2 + \frac{2\Delta z}{\Delta t} W^i_{+,o} + 2aB^i_u \Delta z\Big). \tag{3.104}$$

Note that generally $W_\alpha > 0$ if there are only updrafts, since $\epsilon \Delta z \sim O(1)$, the grid-mean vertical velocity should be small compared to $\Delta z/\Delta t$, and any compensating subsidence would make $W_\alpha$ more positive. With $W_\alpha > 0$, $W^i_{+,N} > 0$ holds if and only if $W_\beta^2 > 0$, i.e.,

$$\Big[W^i_{+,o} + \Big(\frac{1}{2}\frac{(W^i_{o,N})^2}{\Delta z} + aB^i_u\Big)\Delta t\Big] > 0. \tag{3.105}$$

Physically, the three terms represent the previous vertical velocity, the tendency due to influx of vertical momentum from the bottom, and the tendency due to buoyant acceleration. Numerically, for each level, we first test whether condition (3.105) holds. If it does hold, then the velocity $W^i_{+,N}$ is compute with equation (3.102); if it doesn't hold, then the velocity $W^i_{+,N}$ is simply set as 0, meaning that the updraft stops at this level. However, there may still be residual updraft at higher levels.

Note that due to the implicit and upwind discretization, the entrainment tendency term (the last term in equation (3.101)) may be overestimated in accelerating parts of the updraft. Since the entrainment term tends to decelerate the updraft, this means

that the peak updraft velocity may be underestimated. How this would affect the numerical results needs to be tested, but it doesn't seem to affect the stability of the scheme. Also, the entrainment deceleration is underestimated in decelerating parts of the updraft (especially the convective overshoot), but this effect would be minor, since the tendency there is mostly dominated by the negative buoyancy term than by entrainment.

Alternatively, we can first do an integration in the vertical direction just as in Bretherton et al. (2004), but in our formulation there is an extra environmental term $W^n_{+,o}$, which makes it impossible to obtain an explicit form of integrated formula. If this term is neglected, then the continuous form of the equation looks as follows:

$$\frac{\partial w^i}{\partial t} + \frac{1}{2}\frac{\partial (w^i)^2}{\partial z} - aB^i_u + b\epsilon_i (w^i)^2 = 0. \tag{3.106}$$

The second to fourth terms can be written as a single derivative as:

$$\frac{\partial w^i}{\partial t} + \frac{1}{2} e^{-2b\epsilon_i (z-z_c)} \frac{\partial}{\partial z}\Big( (w^i)^2 e^{2b\epsilon_i (z-z_c)} + \frac{aB^i_u}{b\epsilon_i}(1 - e^{2b\epsilon_i (z-z_c)})\Big) = 0. \tag{3.107}$$

In the discretization, we use $z_c = z_o$, thus at $z = z_+$, we have $z - z_c = \Delta z$. The coefficient $\frac{1}{2} e^{-2b\epsilon_i (z-z_c)}$ is also evaluated at $z = z_+$, and the discretized equation is:

$$\frac{W^i_{+,N} - W^i_{+,o}}{\Delta t} + \frac{1}{2} e^{-2b\epsilon_i \Delta z} \frac{(W^i_{+,N})^2 e^{2b\epsilon_i \Delta z} + \frac{aB^i_u}{b\epsilon_i}(1 - e^{2b\epsilon_i \Delta z}) - (W^i_{o,N})^2}{\Delta z} = 0. \tag{3.108}$$

And we can compute the solution of this quadratic equation for $W^i_{+,N}$. The result

is:

$$W^i_{+,N} = -\tilde{W}_\alpha + \sqrt{\tilde{W}^2_\alpha + \tilde{W}^2_\beta}, \tag{3.109}$$

where

$$\tilde{W}_\alpha = \frac{\Delta z}{\Delta t}, \quad \tilde{W}^2_\beta = (W^i_{o,N})^2 e^{-2b\epsilon_i \Delta z} + \frac{2\Delta z}{\Delta t} W^i_{+,o} + \frac{aB^i_u}{b(\epsilon_i)_{+,o}}(1 - e^{-2b\epsilon_i \Delta z}). \tag{3.110}$$

At the non-entraining limit of $\epsilon_i \cdot \Delta z = 0$, the natural limit of $\tilde{W}^2_\beta$ is:

$$\lim_{\epsilon_i \cdot \Delta z \to 0} \tilde{W}^2_\beta = (W^i_{o,N})^2 + \frac{2\Delta z}{\Delta t} W^i_{+,o} + 2aB^i_u \Delta z. \tag{3.111}$$

Not surprisingly, the value of $W^i_{+,N}$ from this discretization is exactly equal to the value from equation (3.102) at this non-entraining limit.

Similar to the previous discretization, we set $W^i_{+,N} = 0$ whenever $\tilde{W}^2_\beta < 0$, and otherwise use directly the equation (3.109).

In summary, the methods (3.102) and (3.109) give two discretized solutions for the updraft velocity equation. The updraft vertical velocity at the surface $w^i_{bot}$ enters the equations as the $W^i_{o,N}$ term of the lowest level. In our current formulation, $w^i_{bot} = 0$.

#### 3.7.1.2 Continuity equation

Using implicit and upwind methods, equation (3.97) is discretized as follows (using simplified notations as for the updraft velocity equation):

$$\frac{\rho_+ a^i_{+,N} - \rho_+ a^i_{+,o}}{\Delta t} + \frac{\rho_+ a^i_{+,N} W^i_{+,N} - \rho_o a^i_{o,N} W^i_{o,N}}{\Delta z} = \rho_+ a^i_{+,N} W^i_{+,N} (\epsilon_i - \delta_i). \tag{3.112}$$

Here, $\Delta z$ and $W$ are defined as in the above section; $\rho_+$ and $\rho_o$ represents the density at full-levels $z_+$ and $z_o$, respectively; $\epsilon$ and $\delta$ are entrainment and detrainment rates at $(z_+, t_o)$. These values are computed explicitly with the input values of temperature and pressure. However, if the strict mass-conservation is enforced, then we should use $\rho_+$ from one time-step earlier for the term $\rho_+ a^i_{+,o}$. We have not implemented this, since this would require extra memory for $\rho$.

Solving this equation, we get

$$\rho_+ a^i_{+,N} = \frac{\rho_+ a^i_{+,o} \frac{\Delta z}{\Delta t} + \rho_o a^i_{o,N} W^i_{o,N}}{\frac{\Delta z}{\Delta t} + (1 + \delta_i \Delta z - \epsilon_i \Delta z) W^i_{+,N}}. \tag{3.113}$$

Note that the $-\epsilon_i$ in the denominator may generate unstable results. Thus we may change the entrainment term to be evaluated with $\rho_o a_{o,N} W^i_{o,N}$ instead of $\rho_+ a_{+,N} W^i_{+,N}$ in equation (3.112), and the solution is

$$\rho_+ a^i_{+,N} = \frac{\rho_+ a^i_{+,o} \frac{\Delta z}{\Delta t} + \rho_o a^i_{o,N} (1 + \epsilon_i \Delta z) W^i_{o,N}}{\frac{\Delta z}{\Delta t} + (1 + \delta_i \Delta z) W^i_{+,N}}. \tag{3.114}$$

Or we may compute both terms with $\rho_o a_{o,N} W^i_{o,N}$ and the solution is

$$\rho_+ a^i_{+,N} = \frac{\rho_+ a^i_{+,o} \frac{\Delta z}{\Delta t} + \rho_o a^i_{o,N} (1 + \epsilon_i \Delta z - \delta_i \Delta z) W^i_{o,N}}{\frac{\Delta z}{\Delta t} + W^i_{+,N}}. \tag{3.115}$$

Another way to solve equation (3.97) is by first rewritten it into the following form (as in Bretherton et al. 2004):

$$\frac{\partial}{\partial t}(\rho a_i) + e^{(\epsilon_i - \delta_i)(z - z_c)} \frac{\partial}{\partial z} \Big( e^{-(\epsilon_i - \delta_i)(z - z_c)} \rho a_i w^i \Big) = 0. \tag{3.116}$$

Depending on the value $z$ chosen in the discretization for the exponential term $e^{(\epsilon_i-\delta_i)(z-z_c)}$, this equation can be discretized as

$$\frac{\rho_+ a^i_{+,N} - \rho_+ a^i_{+,o}}{\Delta t} + \frac{\rho_+ a^i_{+,N} W^i_{+,N} e^{(\epsilon_i-\delta_i)(z-z_+)} - \rho_o a^i_{o,N} W^i_{o,N} e^{(\epsilon_i-\delta_i)(z-z_0)}}{\Delta z} = 0. \quad (3.117)$$

The general solution is

$$\rho_+ a^i_{i,N} = \frac{\rho_+ a^i_{+,o} \frac{\Delta z}{\Delta t} + \rho_o a^i_{o,N} W^i_{o,N} e^{(\epsilon_i-\delta_i)(z-z_0)}}{\frac{\Delta z}{\Delta t} + W^i_{+,N} e^{(\epsilon_i-\delta_i)(z-z_+)}}. \quad (3.118)$$

Here we choose $z = z_+$, and the result is

$$\rho_+ a^i_{+,N} = \frac{\rho_+ a^i_{+,o} \frac{\Delta z}{\Delta t} + \rho_o a^i_{o,N} W^i_{o,N} e^{(\epsilon_i-\delta_i)\Delta z}}{\frac{\Delta z}{\Delta t} + W^i_{+,N}}. \quad (3.119)$$

If we choose $z = z_o$ instead, the result is

$$\rho_+ a^i_{+,N} = \frac{\rho_+ a^i_{+,o} \frac{\Delta z}{\Delta t} + \rho_o a^i_{o,N} W^i_{o,N}}{\frac{\Delta z}{\Delta t} + W^i_{+,N} e^{-(\epsilon_i-\delta_i)\Delta z}}. \quad (3.120)$$

Note that at the non-entraining/detraining limit ($(\epsilon_i - \delta_i)\Delta z \to 0$), the results are respectively

$$\begin{aligned} \rho_+ a^i_{+,N} &= \frac{\rho_+ a^i_{+,o} \frac{\Delta z}{\Delta t} + \rho_o a^i_{o,N} W^i_{o,N} (1 + (\epsilon_i - \delta_i)\Delta z)}{\frac{\Delta z}{\Delta t} + W^i_{+,N}}, \\ \rho_+ a^i_{+,N} &= \frac{\rho_+ a^i_{+,o} \frac{\Delta z}{\Delta t} + \rho_o a^i_{o,N} W^i_{o,N}}{\frac{\Delta z}{\Delta t} + W^i_{+,N} (1 - (\epsilon_i - \delta_i)\Delta z)}. \end{aligned} \quad (3.121)$$

These results are the same as the direct discretization of equations (3.115) and

(3.113), where the entrainment/detrainment terms are evaluated with bottom conditions or top conditions.

In all of the four discretized solutions by equations (3.113), (3.114), (3.115), (3.119), and (3.120), there are two situations that would greatly increase $a^i$: one is when $W^i_{o,N} \gg W^i_{+,N}$, and the other is when $\epsilon$ is large. The first situation occurs at top-detrainment areas; the second situation is mostly related to the lowest layer. In both of these conditions, we have to increase the detrainment to avoid excessive $a_{i,N}$. Also, to keep a constant updraft fraction at the bottom, we need to additionally include the bottom entrainment at the lowest level.

Here let's take the formulation (3.119), i.e., the current default formulation, as an example to illustrate the updraft procedure. It is similar for other formulations.

At the lowest level, we would like to have a constant updraft fraction ($a_+$ =const). However, this is impossible with the formulation, since the entrainment rate needs to be infinity for the updraft mass flux to increase from 0 at the bottom to some finite value at the top of the first level. Thus we modify the equation (3.119) with an extra term representing bottom entrainment (similar to the 'organized entrainment' in some other models):

$$\rho_+ a^i_{+,N} = \frac{\rho_+ a^i_{+,o} \frac{\Delta z}{\Delta t} + \rho_o a^i_{o,N} W^i_{o,N} e^{(\epsilon_i - \delta_i)\Delta z} + m^i_{\epsilon,B}}{\frac{\Delta z}{\Delta t} + W^i_{+,N}}, \tag{3.122}$$

where $m^i_{\epsilon,B}$ is the boundary (bottom) entrainment mass-flux. If we denote the lateral

entrainments and detrainments as follows:

$$m^i_{\epsilon,L} = \frac{\epsilon_i}{\epsilon_i - \delta_i}\rho_o a^i_{o,N} W^i_{o,N}(e^{(\epsilon_i-\delta_i)\Delta z} - 1), \quad m^i_{\delta,L} = \frac{\delta_i}{\epsilon_i - \delta_i}\rho_o a^i_{o,N} W^i_{o,N}(e^{(\epsilon_i-\delta_i)\Delta z} - 1), \tag{3.123}$$

then the equation is rewritten as

$$\rho_+ a^i_{+,N} = \frac{\rho_+ a^i_{+,o}\frac{\Delta z}{\Delta t} + \rho_o a^i_{o,N} W^i_{o,N} + m^i_{\epsilon,L} - m^i_{\delta,L} + m^i_{\epsilon,B}}{\frac{\Delta z}{\Delta t} + W^i_{+,N}}. \tag{3.124}$$

Thus, with bottom condition of $W^i_{o,N} = 0$, we have $m^i_{\epsilon,L} = m^i_{\delta,L} = 0$, and thus for $a^i_{+,N} = a^i_{+,o}$, we need

$$m^i_{\epsilon,B} = \rho_+ a^i_{+,N} W^i_{+,N}. \tag{3.125}$$

For the highest levels of the updraft, we need to have an extra term representing boundary (top) detrainment (similar to 'organized detrainment' in other models). This term is denoted as $m_{\delta,B}$, and the equation is modified as

$$\rho_+ a^i_{+,N} = \frac{\rho_+ a^i_{+,o}\frac{\Delta z}{\Delta t} + \rho_o a^i_{o,N} W^i_{o,N} + m^i_{\epsilon,L} - m^i_{\delta,L} - m^i_{\delta,B}}{\frac{\Delta z}{\Delta t} + W^i_{+,N}}, \tag{3.126}$$

where $m^i_{\epsilon,L}, m^i_{\delta,L}$ are as defined in (3.123), and $m^i_{\delta,B}$ can be closed by multiple assumptions. For example, if we assume that the maximum updraft fraction does not exceed the bottom value (which then ensures that the total updraft fraction is much smaller than 1), then if $a^i_{+,N} > a^i_{bot,N}$ without $m^i_{\delta,B}$, we can define

$$m^i_{\delta,B} = (\frac{\Delta z}{\Delta t} + W^i_{+,N})(a^i_{+,N} - a^i_{bot,N}). \tag{3.127}$$

Then with this $m^i_{\delta,B}$, $a^i_{+,N}$ will be equal to $a^i_{bot,N}$ exactly.

Another possible constraint assumption is to choose $m^i_{\delta,B}$ such that $a^i$ never increases with height, i.e., top detrainment occurs whenever the updraft decelerates. This will also limit the total updraft fraction to be less than 1, but this may detrain the updrafts too early (i.e., detrainment level may be too low). We will test the sensitivity of the model to these two assumptions, but we would use the former assumption and enforce equation (3.127) by default.

Note that by equations (3.123, 3.125, 3.127), we can actually compute the entrainment/detrainment mass fluxes for each level by top/bottom and lateral mixing processes. With these values, the updraft continuity equation can be written in the following form that clarifies the discretized form of mass conservation:

$$\frac{\rho_+ a^i_{+,N} - \rho_+ a^i_{+,o}}{\Delta t} + \frac{\rho_+ a^i_{+,N} W^i_{+,N} - \rho_o a^i_{o,N} W^i_{o,N}}{\Delta z} = \frac{m^i_{\epsilon,L} - m^i_{\delta,L} + m^i_{\epsilon,B} - m^i_{\delta,B}}{\Delta z}. \tag{3.128}$$

The first fraction on the left-hand-side represents the tendency for updraft mass for level $z_+$. The section fraction represent the bottom influx and top outflux of mass (using upwind flux and implicit time-stepping). The right-hand-side represents the entrainment/detrainment exchange of mass between the $i$-th updraft and the environment. Comparing this equation to equation (3.97), we can see that the corresponding continuous and discretized forms of mass-exchange terms as follows:

$$\rho a_i w^i \epsilon_i \longrightarrow (m^i_{\epsilon,L} + m^i_{\epsilon,B})/\Delta z, \quad \rho a_i w^i \delta_i \longrightarrow (m^i_{\delta,L} + m^i_{\delta,B})/\Delta z. \tag{3.129}$$

In the next sections we will see that the computed mass-exchange terms $m_{\epsilon/\delta,L/B}$ are directly used in the discretized updraft tracer equations and environmental equations. In this way, all discretizations are consistent, and all conservations would be satisfied.

#### 3.7.1.3 Tracer equation

The left-hand-side of the tracer equation (3.98) can be discretized similarly to equation (3.97) with upwind and implicit scheme. The entrainment/detrainment terms on the right-hand-side can be discretized consistently with formulation (3.129) as:

$$\rho a_i w^i \epsilon_i \phi^n \longrightarrow (m^i_{\epsilon,L}+m^i_{\epsilon,B})\phi^n_{+,o}/\Delta z, \quad \rho a_i w^i \delta_i \phi^i \longrightarrow (m^i_{\delta,L}+m^i_{\delta,B})\phi^i_{+,N}/\Delta z. \tag{3.130}$$

Here, the environmental value for $\phi$ is discretized explicitly, since it is generally not possible to implicitly compute the adjusted value of environmental tracer values, except by iteration. The updraft value for $\phi$ is discretized implicitly consistent with the other discretizations (e.g. for updraft velocity and mass). The full discretized equation is

$$\begin{aligned}\frac{\rho_+ a^i_{+,N}\phi^i_{+,N} - \rho_+ a^i_{+,o}\phi^i_{+,o}}{\Delta t} + \frac{\rho_+ a^i_{+,N} W^i_{+,N}\phi^i_{+,N} - \rho_o a^i_{o,N} W^i_{o,N}\phi^i_{o,N}}{\Delta z} \\ = \frac{(m^i_{\epsilon,L}+m^i_{\epsilon,B})\phi^n_{+,o} - (m^i_{\delta,L}+m^i_{\delta,B})\phi^i_{+,N}}{\Delta z} + \rho_+ a^i_{+,N} S^i_\phi.\end{aligned} \tag{3.131}$$

Notice that the equations (3.128) and (3.131) can be combined to yield the discretized form of the advection-form updraft tracer equation that satisfies the dis-

cretized conservations.

$$\frac{\rho_+ a^i_{+,o}(\phi^i_{+,N} - \phi^i_{+,o})}{\Delta t} + \frac{\rho_o a^i_{o,N} W^i_{o,N}(\phi^i_{+,N} - \phi^i_{o,N})}{\Delta z} = \frac{(m^i_{\epsilon,L} + m^i_{\epsilon,B})(\phi^n_{+,o} - \phi^i_{+,N})}{\Delta z} + \rho_+ a^i_{+,N} S^i_\phi. \tag{3.132}$$

This corresponds to the continuous form advective equation (3.71). Note that many upwind-implicit terms are cancelled with the subtraction between equations (3.128) and (3.129), and thus the residue equation is neither upwind-like nor fully-implicit. However, this is still a first-order accurate discretization, and the solution for $\phi^i_{+,N}$ is as follows (assuming that the source term $S^i_\phi$ is zero):

$$\phi^i_{+,N} = \frac{\rho_+ a^i_{+,o} \frac{\Delta z}{\Delta t} \cdot \phi^i_{+,o} + \rho_o a^i_{o,N} W^i_{o,N} \cdot \phi^i_{o,N} + (m^i_{\epsilon,L} + m^i_{\epsilon,B}) \cdot \phi^n_{+,o}}{\rho_+ a^i_{+,o} \frac{\Delta z}{\Delta t} + \rho_o a^i_{o,N} W^i_{o,N} + (m^i_{\epsilon,L} + m^i_{\epsilon,B})} \tag{3.133}$$

The solution $\phi^i_{+,N}$ is a convex linear combination of $\phi^i_{+,o}$, $\phi^i_{o,N}$, and $\phi^n_{+,o}$, and thus it should be stable. Especially, at the limit of $\Delta z/\Delta t \to 0$ (i.e., equilibrium updraft), $\delta \to 0$, $m^i_{\epsilon,B} = 0$, this equation is just simplified as

$$\phi^i_{+,N} = \phi^i_{o,N} e^{-\epsilon_i \Delta z} + \phi^n_{+,o}(1 - e^{-\epsilon_i \Delta z}), \tag{3.134}$$

which is exactly as the discretization by Bretherton et al. (2004). Further analysis indicates that our solution for $\delta_i \neq 0$ differs from their solution by a term with magnitude of $O((\epsilon_i \Delta z)^2)$. This difference is consistent with the upwind discretization: in our model, the grid-mean tracer concentration is assumed to be the same as that of

the top-outflow, while in Bretherton et al. (2004) the two concentrations are different due to the piecewise exponential profile.

After equation (3.133) is evaluated for $\theta_l$ and $q_t$, we then follow equations (3.18) to (3.21) for the precipitative adjustment, and the tendencies $\Delta\phi^i|_{\text{prec}}$ are added to the results of $\theta_l$ and $q_t$. This is equivalent to prescribing the source term $S^i_\phi$ in equation (3.131) as

$$\begin{aligned}\rho_+ a^i_{+,N} S^i_\phi &= \Delta\phi^i|_{\text{prec}} \cdot \frac{\rho_+ a^i_{+,o}\frac{\Delta z}{\Delta t} + \rho_o a^i_{o,N} W^i_{o,N} + (m^i_{\epsilon,L} + m^i_{\epsilon,B})}{\Delta z} \\ &= \Delta\phi^i|_{\text{prec}} \cdot \frac{\rho_+ a^i_{+,N}\frac{\Delta z}{\Delta t} + \rho_+ a^i_{+,N} W^i_{+,N} + (m^i_{\delta,L} + m^i_{\delta,B})}{\Delta z}.\end{aligned} \tag{3.135}$$

### 3.7.2 Discretization of the environmental equations

The flux form of environmental equations can generally be deduced by subtracting the updraft equations from the grid-mean equation. The grid-mean equations are:

$$\begin{aligned}&\frac{\partial}{\partial t}(\rho\phi^T) + \frac{\partial}{\partial z}(\rho w^T \phi^T) + \overline{[\nabla_h \cdot (\rho\phi \mathbf{u}_h)]}_T \\ &\qquad = -\frac{\partial}{\partial z}\sum_{i\neq n}\Big((m_i - \rho a_i w^T)(\phi^i - \phi^n)\Big) - \frac{\partial}{\partial z}\Big(a_n \rho \overline{w'\phi'}^n\Big) + \rho S^T_\phi.\end{aligned} \tag{3.136}$$

In the GCM, the grid-scale advection terms (i.e., the second and third terms on the left hand side) are handled by the dynamical core. Spatial filters are also applied to the numerical solutions, which are not represented here in the exact equation. And we also need to parameterize for the right hand side terms.

The corresponding updraft equation that we have solved is as equation (3.98):

$$\frac{\partial}{\partial t}(\rho a_i \phi^i) + \frac{\partial}{\partial z}(\rho a_i w^i \phi^i) = \rho a_i \overline{w}^i (\epsilon_i \phi^n - \delta_i \phi^i) + \rho a_i S^i_\phi. \tag{3.137}$$

So subtracting this updraft equation from the total equation, we can get the flux form of environmental equation as

$$\begin{aligned} &\frac{\partial}{\partial t}(\rho a_n \phi^n) + \frac{\partial}{\partial z}(\rho a_n w^n \phi^n) + \overline{[\nabla_h \cdot (\rho \phi \mathbf{u}_h)]}_T \\ &\qquad = -\frac{\partial}{\partial z}\Big(a_n \rho \overline{w' \phi'}^n\Big) - \rho a_i w^i (\epsilon_i \phi^n - \delta_i \phi^i) + \rho a_n S^n_\phi, \end{aligned} \tag{3.138}$$

where we have used the equality

$$\sum_{i \neq n} \Big( (m_i - \rho a_i w^T)(\phi^i - \phi^n) \Big) = \sum_i m_i (\phi^i - \phi^T) = \Big( \sum_i \rho a_i w^i \phi^i \Big) - \rho w^T \phi^T. \tag{3.139}$$

Note that in reality, the horizontal advection term should be decomposed between the environment and the updrafts. The horizontal flux has the form $\rho \phi \mathbf{u}_h$. Doing the area decomposition on the grid boundary gives (neglecting all sub-area horizontal variations)

$$\overline{\rho \phi \mathbf{u}_h}^B = \sum_i \rho a_{B_i} \phi^i {\mathbf{u}_h}^{B_i}. \tag{3.140}$$

Let's first assume that the updrafts and environment are randomly distributed at the grid boundaries (with the same probability distribution as the grid interior and without coherent patterns), thus $a_{B_i} = a_i$. From here we can further make two different assumptions. One assumption is that the velocity distribution at the

boundary is uncorrelated to the distribution of updraft and the environment, so that

$$\mathbf{u}_h{}^{B_i} = \mathbf{u}_h{}^B, \quad \text{for all } i, \tag{3.141}$$

and the corresponding decomposition is

$$\overline{\rho\phi\mathbf{u}_h}^B = \mathbf{u}_h{}^B \sum_i \rho a_i \phi^i. \tag{3.142}$$

In this case, the horizontal flux can be linearly decomposed between the environment and the updrafts as

$$\overline{[\nabla_h \cdot (\rho\phi\mathbf{u}_h)]}_T = \sum_{i\neq n} \overline{[\nabla_h \cdot (\rho a_i \phi^i \mathbf{u}_h)]}_T + \overline{[\nabla_h \cdot (\rho a_n \phi^n \mathbf{u}_h)]}_T. \tag{3.143}$$

And the term $\overline{[\nabla_h \cdot (\rho a_i \phi^i \mathbf{u}_h)]}$ should be added to the left hand side of the updraft equation (3.137). So the updraft and environmental equations appear as

$$\frac{\partial}{\partial t}(\rho a_i \phi^i) + \frac{\partial}{\partial z}(\rho a_i w^i \phi^i) + \overline{[\nabla_h \cdot (\rho a_i \phi^i \mathbf{u}_h)]}_T = \rho a_i w^i (\epsilon_i \phi^n - \delta_i \phi^i) + \rho a_i S^i_\phi, \tag{3.144}$$

$$\begin{aligned}\frac{\partial}{\partial t}(\rho a_n \phi^n) + \frac{\partial}{\partial z}(\rho a_n w^n \phi^n) + \overline{[\nabla_h \cdot (\rho a_n \phi^n \mathbf{u}_h)]}_T = -\frac{\partial}{\partial z}\Big(a_n \rho \overline{w'\phi'}^n\Big) \\ -\rho a_i \overline{w}^i (\epsilon_i \phi^n - \delta_i \phi^i) + \rho a_n S^n_\phi,\end{aligned} \tag{3.145}$$

which would still sum up to the same total equation (3.136). So we can think of the equations (3.137) and (3.138) as approximate equations, which differ from the exact equation by the terms $\overline{[\nabla_h \cdot (\rho a_i \phi^i \mathbf{u}_h)]}_T$ $(i \neq n)$. This approximation should be valid,

since the timescales for the vertical advection and mixing in the updraft are much shorter than the grid-scale horizontal advection ($|w^i|/|\Delta z| \gg |\mathbf{u_h}|/|\Delta x|$).

The alternative assumption is that the fluxes through the boundaries are only contributed by the environment. The physical meaning is that the updrafts are not moving at the grid boundary. Thus, the velocities are

$$\mathbf{u}_h{}^{B_i} = \mathbf{0}, \text{ where } i \neq n; \quad \mathbf{u}_h{}^{B_n} = a_n^{-1}\mathbf{u}_h{}^{B}, \tag{3.146}$$

and the corresponding decomposition is

$$\overline{\rho\phi\mathbf{u}_h}^{B} = \rho a_n \phi^n (a_n^{-1}\mathbf{u}_h{}^{B}) = \mathbf{u}_h{}^{B}\rho\phi^n. \tag{3.147}$$

Similar to the above discussion, the updraft and environmental equations appear as

$$\frac{\partial}{\partial t}(\rho a_i \phi^i) + \frac{\partial}{\partial z}(\rho a_i w^i \phi^i) = \rho a_i w^i(\epsilon_i \phi^n - \delta_i \phi^i) + \rho a_i S_\phi^i, \tag{3.148}$$

$$\begin{aligned}\frac{\partial}{\partial t}(\rho a_n \phi^n) + \frac{\partial}{\partial z}(\rho a_n w^n \phi^n) + \overline{[\nabla_h \cdot (\rho\phi^n \mathbf{u}_h)]}_T \\ = -\frac{\partial}{\partial z}\Big(a_n \rho \overline{w'\phi'}^n\Big) - \rho a_i w^i(\epsilon_i \phi^n - \delta_i \phi^i) + \rho a_n S_\phi^n.\end{aligned} \tag{3.149}$$

Now these two equations no longer sum up to the total equation (3.136). There would be an extra term $\overline{[\nabla_h \cdot (\rho(\phi^n - \phi)\mathbf{u}_h)]}_T$ that represents the sub-grid component of the horizontal advection, since the correlation between velocity and tracer $\phi$ is no longer zero. Although this term may still be small, we are not in favor of this

assumption, and would use the first assumption instead.

Here we will only discretize the right hand side of equation (3.136) in the solver (denoted as $\rho\frac{d\phi^T}{dt}|_{EDMF}$), for which we separately discretize the three terms, denoted respectively as the mass-flux component $\rho\frac{d\phi^T}{dt}|_{MF}$, the eddy-diffusion component $\rho\frac{d\phi^T}{dt}|_{ED}$, and the source/sink component $\rho\frac{d\phi^T}{dt}|_{S}$, i.e.,

$$\left.\frac{d\phi^T}{dt}\right|_{EDMF} = \left.\frac{d\phi^T}{dt}\right|_{MF} + \left.\frac{d\phi^T}{dt}\right|_{ED} + \left.\frac{d\phi^T}{dt}\right|_{S}. \tag{3.150}$$

The individual terms are formulated as follows:

$$\left.\frac{d\phi^T}{dt}\right|_{MF} = -\frac{1}{\rho}\frac{\partial}{\partial z}\sum_{i\neq n}\Big((m_i - \rho a_i w^T)(\phi^i - \phi^n)\Big) = -\frac{1}{\rho}\frac{\partial}{\partial z}\sum_{i\neq n}\Big(\rho a_i (w^i - w^T)(\phi^i - \phi^n)\Big), \tag{3.151}$$

$$\left.\frac{d\phi^T}{dt}\right|_{ED} = -\frac{1}{\rho}\frac{\partial}{\partial z}\Big(a_n \rho \overline{w'\phi'}^n\Big), \tag{3.152}$$

$$\left.\frac{d\phi^T}{dt}\right|_{S} = S_\phi^T = \sum_{i\neq n}(a_i S_\phi^i) + a_n S_\phi^n. \tag{3.153}$$

#### 3.7.2.1 Mass-flux component

The mass-flux component term $\left.\frac{d\phi^T}{dt}\right|_{MF}$ is discretized in the following form:

$$\left.\frac{d\phi^T}{dt}\right|_{MF}^{z=z_+} \approx -\frac{1}{\rho_+ \Delta z}\sum_{i\neq n}\Big(M_+^i(\phi_{+,N}^i - \phi_{+,o}^n) - M_o^i(\phi_{o,N}^i - \phi_{o,o}^n)\Big), \tag{3.154}$$

where

$$M_+^i = \rho_+ a_{+,N}^i (W_{+,N}^i - W_+^T), \quad M_o^i = \rho_o a_{o,N}^i (W_{o,N}^i - W_o^T). \tag{3.155}$$

The meanings of the subscripts are the same as in section 3.1.1. The updraft parameters $a^i$, $\phi^i$, and $W^i$ are computed as in section 3.1, and the other parameters (environment and grid-mean) $\rho$, $W^T$, $\phi^n$ are taken from the GCM values of the previous step (with modification by any parameterization preceding to the EDMF scheme).

#### 3.7.2.2 Eddy-diffusion component

After solving the grid-box mean mass-flux tendency, we can update the grid-box mean variables $\phi^T$ as

$$\phi_*^T = \phi_o^T + \Delta t\Big(\frac{d\phi^T}{dt}\Big|_{MF} + a_N^i S_\phi^i\Big). \tag{3.156}$$

Thus $\phi_*^T$ is the adjusted grid-mean value with MF tendencies and updraft source terms. Then we can compute the updraft/environment decomposition again to get the updated environmental value after MF effects, i.e.,

$$a_N^n = 1 - \sum_{i\neq n} a_N^i, \quad \phi_*^n = \frac{1}{a_N^n}\big(\phi_*^T - \sum_{i\neq n} a_N^i \phi_N^i\big). \tag{3.157}$$

Using the relation

$$\phi_{**}^T = \sum_{i\neq n} a^i \phi_{**}^i + a^n \phi_{**}^n = \phi_*^T + a^n(\phi_{**}^n - \phi_*^n), \tag{3.158}$$

where the subscript $**$ represents the values after adjustment with ED tendencies. Then the eddy-diffusion component is computed by solving the following diffusive

equation (discretized version of equation (3.152)):

$$\begin{aligned}\frac{\rho_o a^n_{o,N}(\phi^n_{o,**}-\phi^n_{o,*})}{\Delta t} &= \rho_o \frac{\phi^T_{o,**}-\phi^T_{o,*}}{\Delta t} \\ &= \frac{1}{\Delta z_o}\Big((\rho a^n K_m)_{+/2}\frac{\phi^n_{+,**}-\phi^n_{o,**}}{\Delta z_+} - (\rho a^n K_m)_{-/2}\frac{\phi^n_{o,**}-\phi^n_{-,**}}{\Delta z_-}\Big),\end{aligned} \tag{3.159}$$

where the diffusive flux $\overline{w'\phi'}^n$ at the half-level $z_{+/2}$ has been parameterized implicitly in time as

$$\overline{w'\phi'}^n|_{z_{+/2}} = -K_m\frac{\partial \phi^n}{\partial z}\Big|_{z_{+/2}} \approx -(K_m)|_{z_{+/2}}\frac{\phi^n_{+,**}-\phi^n_{o,**}}{\delta z_+}, \tag{3.160}$$

and $\Delta z_+ = z_+ - z_o$, $\Delta z_- = z_o - z_-$, $\Delta z_o = z_{+/2} - z_{-/2}$. Also, note that the half-level values of $\rho a^n K_m$ need to be interpolated from the known values at full-levels.

The diffusive equation is implicit and tridiagonal, so it can be solved with a tridiagonal solver. Actually, this equation is the same as ED equation in the previous GCM, except that the effective density is $\rho a_n$ instead of $\rho$. The top boundary condition is zero-flux, and the bottom boundary flux is given as the total surface flux divided by $a_n$ at surface, i.e., it is assumed that all surface fluxes go into the environmental part. But the most energetic part will be immediately entrained into the updraft, so there is still effectively a decomposition of surface fluxes between the updraft and the environment.

After solving this equation, we get the new tracer values in the environment ($\phi^n_{**}$)

as well as the ED tendency of the grid-box mean:

$$\left.\frac{d\phi^T}{dt}\right|_{ED} = a^n \frac{\phi^n_{**} - \phi^n_*}{\Delta t}. \tag{3.161}$$

We will use the value $\phi^n_{**}$ in the cloud and precipitation schemes, and thus calculate source terms of the environment $S^n_\phi$. The details are given as below.

#### 3.7.2.3 TKE prognostic equation

Similar to the environmental equations, the TKE prognostic equation is written in the following flux form:

$$\begin{aligned}
&\frac{\partial}{\partial t}(\rho E^T) + \frac{\partial}{\partial z}(\rho w^T E^T) + \overline{[\nabla_h \cdot (\rho E \mathbf{u}_h)]}_T = \\
&- \frac{\partial}{\partial z}\sum_{i\neq n}\Big((m_i - \rho a_i w^T)(-E^n)\Big) - \frac{\partial}{\partial z}\Big(a_n \rho \overline{w' E'}^n\Big) \\
&+ \sum_{i\neq n}\Big(m_i \delta_i \big(\frac{1}{2}(w^i - w^n)^2\big) - m_i \epsilon_i E^n\Big) + \rho a_n (P^n_E + B^n_E + D^n_E).
\end{aligned} \tag{3.162}$$

Here we have used $E^i = 0, E^T = a_n E^n$. The difference from the other tracers is that, upon entrainment, the entrained TKE (i.e., $E^n$) into the updraft is instantly reset to 0; and that upon detrainment, the detrained TKE from the updraft is assumed to be $\frac{1}{2}(w^i)^2$ instead of 0.

With this form of TKE equation, we can discretize the mass-flux term and the entrainment (detrainment) terms in a consistent way as the other tracers. The right

hand side can be written in four terms:

$$\frac{dE^T}{dt}\Big|_{EDMF} = \frac{dE^T}{dt}\Big|_{MF} + \frac{dE^T}{dt}\Big|_{ED} + \frac{dE^T}{dt}\Big|_{S}. \tag{3.163}$$

The individual terms are formulated as follows:

$$\frac{dE^T}{dt}\Big|_{MF} = -\frac{1}{\rho}\frac{\partial}{\partial z}\sum_{i\neq n}\Big((m_i - \rho a_i w^T)(-E^n)\Big) + \frac{1}{\rho}\sum_{i\neq n}\Big(m_i\delta_i\big(\frac{1}{2}(w^i - w^n)^2\big) - m_i\epsilon_i E^n\Big), \tag{3.164}$$

$$\frac{dE^T}{dt}\Big|_{ED} = -\frac{1}{\rho}\frac{\partial}{\partial z}\Big(a_n\rho\overline{w'E'}^n\Big), \tag{3.165}$$

$$\frac{dE^T}{dt}\Big|_{S} = a_n(P_E^n + B_E^n + D_E^n). \tag{3.166}$$

The MF component is discretized as

$$\begin{aligned}\frac{d\overline{E}^T}{dt}\Big|_{MF}^{z=z_+} \approx \frac{1}{\rho_+\Delta z}\sum_{i\neq n}\Big(&M_+^i E_{+,o}^n - M_o^i E_{o,o}^n \\ &+ (m_{\delta,L}^i + m_{\delta,B}^i)\cdot\frac{1}{2}(W_{+,N}^i - W_{+,N}^n)^2 - (m_{\epsilon,L}^i + m_{\epsilon,B}^i)E_{+,o}^n\Big),\end{aligned} \tag{3.167}$$

where we have used the relation (3.129)

$$m_i\epsilon_i \longrightarrow (m_{\epsilon,L}^i + m_{\epsilon,B}^i)/\Delta z, \quad m_i\delta_i \longrightarrow (m_{\delta,L}^i + m_{\delta,B}^i)/\Delta z.$$

The source terms are computed as discretized versions of equations (3.32) - (3.34), with diagnosed environmental buoyancy flux $\overline{w'\theta_v'}^n$ computed as in the above section, and diffusivity $K_m$ is taken from the previous time step.

After the MF and source components are computed, the TKE is updated. Then the ED component is computed in the same way as other tracers in the previous section (Equations (3.156) - (3.161)).

One caveat is the parameterization of dissipation term. It can be computed explicitly as

$$D_E^n = -c_e \frac{(E_o^n)^{3/2}}{l_d}, \tag{3.168}$$

but we are doing a single step integration instead, i.e., integrating the equation $(\partial/\partial t)E^n = -c_e \frac{(E_o^n)^{3/2}}{l_d}$ over the time period $\Delta t$, so we get the time-averaged dissipation as

$$\overline{D_E^n} = \frac{E_o^n}{\Delta t}\Big( -1 + \big(1 + \frac{c_e \Delta t}{2 l_d}\sqrt{E_o^n}\big)^{-2}\Big). \tag{3.169}$$

This is the same as the explicit formulation at the limit of $\Delta t \to 0$. Alternative to computing $D_E^n$ as the other source terms with $E_o^n$, we may also delay the dissipation after the computation diffusion, and use $E_{**}^n$ (the updated TKE with EDMF and all other sources) to compute diffusion.

### 3.7.3 Summary of work-flow

The work-flow of the whole model is as follows:

- Finish the other parameterizations (e.g., the radiation scheme in the SCM);
- Get the parameters $\phi^i$, $w^i$, $a^i$, $w^T$, $\phi^T$ from the previous model step;
- Compute the decomposition to get environmental parameters $\phi^n$, $w^n$, $a^n$ for the previous model step;

- Compute the updraft equation to get the $\phi^i$, $w^i$, $a^i$ for the new step;
- Compute the mass-flux part of the EDMF tendency and update the grid-mean variables $w^T$, $\phi^T$ ;
- Compute the decomposition again to get updated environmental parameters $\phi^n$, $w^n$, $a^n$ with the MF effects;
- Compute the eddy-diffusion part of the EDMF tendency, then also diagnose clouds and precipitation, and update again the grid-mean variables $w^T$, $\phi^T$;
- Compute the MF tendency (mass flux from new step), ED tendency (diffusivity from old step), and other source terms of environmental TKE and update it;
- Loop for several times if split-stepping is used;
- Move on to the dynamical core.

The set of equations to solve are:

Equation (3.101) for $W^i$:

$$\frac{W^i_{+,N} - W^i_{+,o}}{\Delta t} + \frac{(W^i_{+,N})^2 - (W^i_{o,N})^2}{2\Delta z} = aB^i_u + b\epsilon_i W^i_{+,N}\big(W^n_{+,o} - W^i_{+,N}\big)$$

$$\Big\{\text{Continuous form: } \frac{\partial w^i}{\partial t} + \frac{1}{2}\frac{\partial (w^i)^2}{\partial z} = aB^i_u + b\epsilon_i w^i(w^n - w^i)\Big\}$$

Equation (3.128) for $a^i$:

$$\frac{\rho_+ a^i_{+,N} - \rho_+ a^i_{+,o}}{\Delta t} + \frac{\rho_+ a^i_{+,N} W^i_{+,N} - \rho_o a^i_{o,N} W^i_{o,N}}{\Delta z} = \frac{m^i_{\epsilon,L} - m^i_{\delta,L} + m^i_{\epsilon,B} - m^i_{\delta,B}}{\Delta z}$$

$$\Big\{\text{Continuous form: } \frac{\partial(\rho a_i)}{\partial t} + \frac{\partial(\rho a_i w^i)}{\partial z} = \rho a_i w^i(\epsilon^i - \delta^i)\Big\}$$

Equation (3.132) for $\phi^i$:

$$\frac{\rho_+ a^i_{+,o}(\phi^i_{+,N} - \phi^i_{+,o})}{\Delta t} + \frac{\rho_o a^i_{o,N} W^i_{o,N}(\phi^i_{+,N} - \phi^i_{o,N})}{\Delta z} = \frac{(m^i_{\epsilon,L} + m^i_{\epsilon,B})(\phi^n_{+,o} - \phi^i_{+,N})}{\Delta z} + \rho_+ a^i_{+,N} S^i_\phi$$

$$\Big\{\text{Continuous form: } \rho a_i \frac{\partial \phi^i}{\partial t} + \rho a_i w^i \frac{\partial \phi^i}{\partial z} = \rho a_i w^i \epsilon^i(\phi^n - \phi^i) + \rho a_i S^i_\phi\Big\}$$

Equations (3.154),(3.155) for $(d\phi^T/dt)_{MF}$:

$$M^i_+ = \rho_+ a^i_{+,N}(W^i_{+,N} - W^T_+), \quad M^i_o = \rho_o a^i_{o,N}(W^i_{o,N} - W^T_o)$$

$$\frac{d\phi^T}{dt}\Big|^{z=z_+}_{MF} \approx -\frac{1}{\rho_+ \Delta z}\sum_{i\neq n}\Big(M^i_+(\phi^i_{+,N} - \phi^n_{+,o}) - M^i_o(\phi^i_{o,N} - \phi^n_{o,o})\Big)$$

$$\Big\{\text{Continuous form: } M^i = \rho a_i(w^i - w^T), \quad \frac{d\phi^T}{dt}\Big|_{MF} = -\frac{1}{\rho}\frac{\partial}{\partial z}\sum_{i\neq n}\Big(M^i(\phi^i - \phi^n)\Big)\Big\}$$

Equation (3.159), (3.161) for $(d\phi^T/dt)_{ED}$:

$$\frac{\rho_o a^n_{o,N}(\phi^n_{o,**} - \phi^n_{o,*})}{\Delta t} = \rho_o \frac{\phi^T_{o,**} - \phi^T_{o,*}}{\Delta t}$$
$$= \frac{1}{\Delta z_o}\Big((\rho a^n K_m)_{+/2}\frac{\phi^n_{+,**} - \phi^n_{o,**}}{\Delta z_+} - (\rho a^n K_m)_{-/2}\frac{\phi^n_{o,**} - \phi^n_{-,**}}{\Delta z_-}\Big)$$

$$\frac{d\phi^T}{dt}\Big|_{ED} \approx a^n \frac{\phi^n_{**} - \phi^n_*}{\Delta t}$$

$$\Big\{\text{Continuous form: } \frac{d\phi^T}{dt}\Big|_{ED} = \frac{1}{\rho}\frac{\partial}{\partial z}\Big((\rho a_n K_m)\frac{\partial \phi^n}{\partial z}\Big)\Big\}$$

The equations of environmental cloud and precipitation, and equations (3.163) - (3.167) for the evolution of environmental TKE.

### 3.7.4 Solutions at the limit of zero updraft fraction

At the limit of zero updraft fraction, updraft velocity equation (3.101) is rewritten as

$$\frac{(W^i_{+,N})^2 - (W^i_{o,N})^2}{2\Delta z} = aB^i_u + b\epsilon_i W^i_{+,N}\big(W^n_{+,o} - W^i_{+,N}\big).$$

And the updraft mass flux formulation (equation (3.154)) is approximated as:

$$M^i = \rho a^i (W^i - W^T) \to \rho a^i W^i.$$

Strictly speaking, at the limit of $a^i \to 0$, the left hand side of the updraft continuity equation (3.128) is just zero, and also $M^i \to 0$ and $(d\phi^T/dt)|_{MF} \to 0$. Physically, this means that the infinitesimal updraft with finite velocity would have no effect on the grid-box. However, the physically relevant limit is that $a^i \to 0$ but $M^i \nrightarrow 0$. This corresponds to an updraft with infinite velocity, and thus zero adjustment time within the updraft. We still need to compute for the other updraft equations with $M^i$ replacing $\rho a^i W^i$, i.e., the updraft continuity equation becomes

$$\frac{M^i_{+,N} - M^i_{o,N}}{\Delta z} = \frac{m^i_{\epsilon,L} - m^i_{\delta,L} + m^i_{\epsilon,B} - m^i_{\delta,B}}{\Delta z},$$

and updraft tracer equation becomes

$$\frac{M^i_{o,N}(\phi^i_{+,N} - \phi^i_{o,N})}{\Delta z} = \frac{(m^i_{\epsilon,L} + m^i_{\epsilon,B})(\phi^n_{+,o} - \phi^i_{+,N})}{\Delta z} + \rho_+ a^i_{+,N} S^i_\phi.$$

Note that $M^i$ does not depend on $W^i$ in these formulations.

With $a^i \to 0$, we have $\phi^T = \phi^n$. The $(d\phi^T/dt)_{MF}$ term is just the same, except that $\phi^n$ is replaced by $\phi^T$:

$$\frac{d\phi^T}{dt}\Big|^{z=z_+}_{MF} \approx -\frac{1}{\rho_+ \Delta z} \sum_{i \neq n} \Big( M^i_+(\phi^i_{+,N} - \phi^T_{+,o}) - M^i_o(\phi^i_{o,N} - \phi^T_{o,o}) \Big).$$

Note that the updraft source term in the grid-mean equation scales with mass flux $M^i$ instead of updraft fraction $a^i$, so it is not zero even with the assumption of $a^i \to 0$. Therefore, the updraft source terms are computed in the same way and added to $\phi^T$. The updated grid-mean values after computing MF tendencies and updraft source terms are denoted as $\phi^T_*$.

The computation of $(d\phi^T/dt)_{ED}$ term is also the same, except that $a^n = 1, \phi^T = \phi^n$:

$$\rho_o \frac{\phi^T_{o,**} - \phi^T_{o,*}}{\Delta t} = \frac{1}{\Delta z_o} \Big( (\rho K_m)_{+/2} \frac{\phi^T_{+,**} - \phi^T_{o,**}}{\Delta z_+} - (\rho K_m)_{-/2} \frac{\phi^T_{o,**} - \phi^T_{-,**}}{\Delta z_-} \Big),$$

$$\frac{d\phi^T}{dt}\Big|_{ED} \approx \frac{\phi^T_{**} - \phi^T_*}{\Delta t}.$$

Then we can compute the cloud and precipitation tendencies in the environment (using $\phi_{**}$ directly). The total tendencies with ED, MF, updraft source terms, and

environmental source terms are obtained by a simple summation.

The environmental TKE equation is similar to the set of equations (3.163) - (3.167) with modifications, and they are as below (only the continuous forms are shown here):

$$\left.\frac{dE^T}{dt}\right|_{EDMF} = \left.\frac{dE^T}{dt}\right|_{MF} + \left.\frac{dE^T}{dt}\right|_{ED} + \left.\frac{dE^T}{dt}\right|_{S},$$

where

$$\left.\frac{dE^T}{dt}\right|_{MF} = -\frac{1}{\rho}\frac{\partial}{\partial z}\sum_{i\neq n}\Big( - m_i E^T)\Big) + \frac{1}{\rho}\sum_{i\neq n}\Big(m_i\delta_i(\frac{1}{2}(w^i - w^T)^2) - m_i\epsilon_i E^T\Big), \quad (3.170)$$

$$\left.\frac{dE^T}{dt}\right|_{ED} = -\frac{1}{\rho}\frac{\partial}{\partial z}\Big(\rho\overline{w' E'}^T\Big), \quad (3.171)$$

$$\left.\frac{dE^T}{dt}\right|_{S} = P_E^T + B_E^T + D_E^T. \quad (3.172)$$

The MF component is thus discretized similarly to equation (3.167):

$$\begin{aligned}\left.\frac{dE^T}{dt}\right|_{MF}^{z=z_+} \approx \frac{1}{\rho_+\Delta z}\sum_{i\neq n}\Big(&M_+^i E_{+,o}^n - M_o^i E_{o,o}^n \\ &+ (m_{\delta,L}^i + m_{\delta,B}^i)\cdot\frac{1}{2}(W_{+,N}^i - W_{+,N}^T)^2 - (m_{\epsilon,L}^i + m_{\epsilon,B}^i)E_{+,o}^n\Big).\end{aligned}$$

Here the $W^i$ term is computed from the updraft velocity equation. Physically, the MF tendencies of other tracers scale with $M^i \sim a^i W^i$ only, but the MF tendencies of $E^T$ scales with $a^i M^i (W^i)^2 \sim a^i (W^i)^3$. Thus, with the same mass-flux and tracer properties, a thinner but faster updraft would produce the same grid-mean tendencies of normal tracers like $\theta_l$ and $q_t$, but it is much more effective in producing environmental TKE.

# Conclusion

This thesis focuses on the development of closures for both the large-scale general circulation models (GCM) and the small-scale large-eddy simulation (LES) such that the processes that are beyond the range of these models can be represented in a physically consistent way. The approach described in this thesis helps to reconcile the investigation and understanding of cloud responses between the large-scale and small-scale perspectives.

The first chapter presents a framework of forcing LES of subtropical MBL clouds that enforces a closed surface energy budget. This is achieved by coupling the atmospheric LES to a slab ocean layer, whose temperature depends on radiative fluxes and surface sensible and latent heat fluxes. Present-day simulations of a variety of subtropical MBL cloud regimes (stratocumulus, cumulus, stratocumulus over cumulus) within this framework give steady-state results similar to simulations under the widely used CGILS framework with fixed SST. The sensitivity of the results to parameters such as a prescribed perturbation in ocean energy uptake is investigated. The agreement of present-day simulations to the observed cloud regimes validates the framework for studies of MBL clouds and how they respond to climate change.

The second chapter follows the forcing framework developed in the first chapter,

and investigates the subtropical cumulus response to warming. With unchanged surface heat uptake and an assumed tropical equilibrium climate sensitivity of 4K per doubling $CO_2$, the subtropical SST warming is found to be less than the tropics, because of the weaker water vapor LW feedback related to the dryness of subtropical free troposphere. This reduced warming is linked to the increased inversion strength and the decrease of inversion height. The surface buoyancy flux also decreases slightly with slight increase in surface RH. The cumulus LWP decreases with warming, mostly due to the reduced cloud-layer depth. The fixed SST experiment shows opposite results with exponential increase of LHF, increased surface buoyancy flux and LCL, and rise of inversion with warming. This contrast in cloud response highlights the importance of constraining the energy budgets in the study of low cloud response.

The third chapter presents a unified EDMF closure of SGS turbulence and convection processes. It follows the work of Siebesma and Teixeira (2000), Soares et al. (2004) and Siebesma et al. (2007) and decomposes the SGS motion into the environment where local isotropic downgradient mixing dominates, and the draft regions where strong non-local transport dominates. The EDMF equations and the various closure assumptions are reexamined, the prognostic terms that represent the life cycles of drafts are included, and the downdraft terms and second-order moment equations can also be consistently formulated. The conventional approximation of small draft area is eliminated, making it more flexible for representing convection across models of different scales. Tests on current-day boundary layer regimes generally agree with the LES results, and further tests with a wide range of LES cloud regimes will be

undertaken, after which it will be available for implementation in GCMs to study how the low cloud interacts with the large-scale circulation under climate change.

# Bibliography

Ackerman, A. S., et al., 2009: Large-eddy simulations of a drizzling, stratocumulus-topped marine boundary layer. *Mon. Wea. Rev.*, **137 (3)**, 1083–1110.

Allen, M. R. and W. J. Ingram, 2002: Constraints on future changes in climate and the hydrologic cycle. *Nature*, **419**, 224–232.

Arakawa, A. and V. R. Lamb, 1977: Computational design of the basic dynamical processes of the UCLA general circulation model. *General Circulation Models of the Atmosphere*, J. Chang, Ed., Academic Press, New York, NY, Methods in Computational Physics: Advances in Research and Applications, Vol. 17, 173–265.

Asselin, R., 1972: Frequency filter for time integrations. *Mon. Wea. Rev.*, **100 (6)**, 487–490.

Balsara, D. S. and C.-W. Shu, 2000: Monotonicity preserving weighted essentially non-oscillatory schemes with increasingly high order of accuracy. *J. Comput. Phys.*, **160**, 405–452.

Bechtold, P., N. Semane, P. Lopez, J.-P. Chaboureau, A. Beljaars, and N. Bormann, 2014: Representing equilibrium and nonequilibrium convection in large-scale models. *J. Atmos. Sci.*, **71 (2)**, 734–753.

Bellon, G. and B. Stevens, 2012: Using the sensitivity of large-eddy simulations to evaluate atmospheric boundary layer models. *J. Atmos. Sci.*, **69**, 1582–1601.

Betts, A. K., 1976: Modeling subcloud layer structure and interaction with a shallow cumulus layer. *J. Atmos. Sci.*, **33 (12)**, 2363–2382.

Blossey, P. N., et al., 2013: Marine low cloud sensitivity to an idealized climate change: The CGILS LES intercomparison. *J. Adv. Model. Earth Sys.*, **5**, 234–258.

Boer, G. J., 1993: Climate change and the regulation of the surface moisture and energy budgets. *Climate Dyn.*, **8**, 225–239.

Bony, S. and J. L. Dufresne, 2005: Marine boundary layer clouds at the heart of tropical cloud feedback uncertainties in climate models. *Geophys. Res. Lett.*, **32**, L20 806.

Bretherton, C. S. and P. N. Blossey, 2014: Low cloud reduction in a greenhouse-warmed climate: Results from lagrangian LES of a subtropical marine cloudiness transition. *J. Adv. Model. Earth Sys.*, **6 (1)**, 91–114.

Bretherton, C. S., P. N. Blossey, and C. R. Jones, 2013: Mechanisms of marine low cloud sensitivity to idealized climate perturbations: A single-LES exploration extending the CGILS cases. *J. Adv. Model. Earth Sys.*, **5**, 316–337.

Bretherton, C. S., J. R. McCaa, and H. Grenier, 2004: A new parameterization for shallow cumulus convection and its application to marine subtropical cloud-topped boundary layers. Part I: Description and 1D results. *Mon. Wea. Rev.*, **132 (4)**, 864–882.

Bretherton, C. S., J. Uchida, and P. N. Blossey, 2010: Slow manifolds and multiple

equilibria in stratocumulus-capped boundary layers. *J. Adv. Model. Earth Sys.*, **2 (4)**.

Bretherton, C. S., et al., 1999: An intercomparison of radiatively driven entrainment and turbulence in a smoke cloud, as simulated by different numerical models. *Quart. J. Roy. Meteor. Soc.*, **125 (554)**, 391–423.

Brient, F., T. Schneider, Z. Tan, S. Bony, X. Qu, and A. Hall, 2015: Shallowness of tropical low clouds as a predictor of climate models response to warming. *Climate Dyn.*, 1–17.

Byun, D. W., 1990: On the analytical solutions of flux-profile relationships for the atmospheric surface-layer. *J. Appl. Meteor.*, **29 (7)**, 652–657.

Caldwell, P. and C. S. Bretherton, 2009: Large eddy simulation of the diurnal cycle in Southeast Pacific stratocumulus. *J. Atmos. Sci.*, **66 (2)**, 432–449.

Cess, R. D., et al., 1990: Intercomparison and interpretation of climate feedback processes in 19 atmospheric general circulation models. *J. Geophys. Res.*, **95**, 16 601–16 615.

Cess, R. D., et al., 1996: Cloud feedback in atmospheric general circulation models: An update. *J. Geophys. Res.*, **101**, 12 791–12 794.

Charney, J. G., 1963: A note on large-scale motions in the tropics. *J. Atmos. Sci.*, **20**, 607–609.

Cheng, A., K.-M. Xu, and B. Stevens, 2010: Effects of resolution on the simulation of boundary-layer clouds and the partition of kinetic energy to subgrid scales. *J. Adv. Model. Earth Sys.*, **2 (1)**.

Chung, D., G. Matheou, and J. Teixeira, 2012: Steady-state large-eddy simulations to study the stratocumulus to shallow cumulus cloud transition. *J. Atmos. Sci.*, **69**, 3264–3276.

Cuijpers, J. W. M. and P. Bechtold, 1995: A simple parameterization of cloud water related variables for use in boundary layer models. *J. Atmos. Sci.*, **52**, 2486–2490.

Dee, D. P., et al., 2011: The ERA-Interim reanalysis: configuration and performance of the data assimilation system. *Quart. J. Roy. Meteor. Soc*, **137**, 553–597.

Donner, L. J., et al., 2011: The dynamical core, physical parameterizations, and basic simulation characteristics of the atmospheric component AM3 of the GFDL global coupled model CM3. *J. Climate*, **24 (13)**, 3484–3519.

Dufresne, J.-L. and S. Bony, 2008: An assessment of the primary sources of spread of global warming estimates from coupled atmosphere–ocean models. *J. Climate*, **21**, 5135–5144.

Duynkerke, P. G., et al., 1999: Intercomparison of three- and one-dimensional model simulations and aircraft observations of stratocumulus. *Bound.-Layer Meteor.*, **92 (3)**, 453–487.

Frierson, D. M. W., I. M. Held, and P. Zurita-Gotor, 2006: A gray-radiation aqua-

planet moist GCM. Part I: Static stability and eddy scale. *J. Atmos. Sci.*, **63**, 2548–2566.

Gesso, S. D., A. P. Siebesma, S. R. de Roode, and J. M. van Wessem, 2014: A mixed-layer model perspective on stratocumulus steady states in a perturbed climate. *Quart. J. Roy. Meteor. Soc.*, **140 (684)**, 2119–2131.

Grabowski, W. W., 1998: Toward cloud resolving modeling of large-scale tropical circulations: A simple cloud microphysics parameterization. *J. Atmos. Sci.*, **55 (21)**, 3283–3298.

Held, I. M. and B. J. Soden, 2000: Water vapor feedback and global warming. *Annu. Rev. Energy Environ.*, **25**, 441–475.

Held, I. M. and B. J. Soden, 2006: Robust responses of the hydrological cycle to global warming. *J. Climate*, **19**, 5686–5699.

Iacono, M. J., J. S. Delamere, E. J. Mlawer, M. W. Shephard, S. A. Clough, and W. D. Collins, 2008: Radiative forcing by long-lived greenhouse gases: Calculations with the AER radiative transfer models. *J. Geophys. Res.: Atmos.*, **113**, D13 103.

Jiang, G.-S. and C.-W. Shu, 1996: Efficient implementation of weighted ENO schemes. *J. Comput. Phys.*, **126**, 202–228.

Kain, J. S. and J. M. Fritsch, 1990: A one-dimensional entraining/detraining plume model and its application in convective parameterization. *J. Atmos. Sci.*, **47 (23)**, 2784–2802.

Knutson, T. R. and S. Manabe, 1995: Time-mean response over the tropical Pacific to increased $CO_2$ in a coupled ocean-atmosphere model. *J. Climate*, **8**, 2181–2199.

Lappen, C.-L. and D. A. Randall, 2001: Toward a unified parameterization of the boundary layer and moist convection. Part I: A new type of mass-flux model. *J. Atmos. Sci.*, **58 (15)**, 2021–2036.

Larson, K., D. L. Hartmann, and S. A. Klein, 1999: The role of clouds, water vapor, circulation, and boundary layer structure in the sensitivity of the tropical climate. *J. Climate*, **12 (8)**, 2359–2374.

Lilly, D. K., 1962: On the numerical simulation of buoyanct convection. *Tellus*, **2**, 148–172.

Liu, X.-D., S. Osher, and T. Chan, 1994: Weighted essentially nonoscillatory schemes. *J. Comput. Phys.*, **115**, 200–212.

Lock, A. P., 2009: Factors influencing cloud area at the capping inversion for shallow cumulus clouds. *Quart. J. Roy. Meteor. Soc.*, **135**, 941–952.

Mailhot, J. and R. Benoit, 1982: A finite-element model of the atmospheric boundary layer suitable for use with numerical weather prediction models. *J. Atmos. Sci.*, **39**, 2249–2266.

Manabe, S. and Wetheral.Rt, 1967: Thermal equilibrium of atmosphere with a given distribution of relative humidity. *J. Atmos. Sci.*, **24 (3)**, 241–259.

Merlis, T. M. and T. Schneider, 2010: Atmospheric dynamics of earth-like tidally locked aquaplanets. *J. Adv. Model. Earth Sys.*, **2 (4)**.

Neale, R. B., et al., 2010: Description of the NCAR Community Atmosphere Model (CAM 5.0). Tech. rep.

Neggers, R., B. Stevens, and J. D. Neelin, 2006: A simple equilibrium model for shallow-cumulus-topped mixed layers. *Theor. Comput. Fluid Dyn.*, **20 (5-6)**, 305–322.

Neggers, R. A. J., B. Stevens, and J. D. Neelin, 2007: Variance scaling in shallow-cumulus-topped mixed layers. *Quart. J. Roy. Meteor. Soc.*, **133 (628)**, 1629–1641.

Nuijens, L., B. Medeiros, I. Sandu, and M. Ahlgrimm, 2015: The behavior of trade-wind cloudiness in observations and models: The major cloud components and their variability. *J. Adv. Model. Earth Sys.*, **7 (2)**, 600–616.

O'Gorman, P. A. and T. Schneider, 2008: The hydrological cycle over a wide range of climates simulated with an idealized GCM. *J. Climate*, **21**, 3815–3832.

Pauluis, O., 2008: Thermodynamic consistency of the anelastic approximation for a moist atmosphere. *J. Atmos. Sci.*, **65**, 2719–2729.

Pierrehumbert, R. T., 1995: Thermostats, radiator fins, and the local runaway greenhouse. *J. Atmos. Sci.*, **52 (10)**, 1784–1806.

Pressel, K. G., C. M. Kaul, T. Schneider, Z. Tan, and S. Mishra, 2015: Large-eddy

simulation in an anelastic framework with closed water and entropy balances. *J. Adv. Model. Earth Sys.*, **7 (3)**, 1425–1456.

Rieck, M., L. Nuijens, and B. Stevens, 2012: Cloud feedbacks in a constant relative humidity atmosphere. *J. Atmos. Sci.*, **69**, 2538–2550.

Robert, A. J., 1966: The integration of a low order spectral form of the primitive meteorological equations (spherical harmonics integration of low order spectral form of primitive meteorological equations). *J. Meteor. Soc. Japan*, **44**, 237–245.

Sandu, I. and B. Stevens, 2011: On the factors modulating the stratocumulus to cumulus transitions. *J. Atmos. Sci.*, **68 (9)**, 1865–1881.

Schalkwijk, J., H. J. J. Jonker, and A. P. Siebesma, 2013: Simple solutions to steady-state cumulus regimes in the convective boundary layer. *J. Atmos. Sci.*, **70 (11)**, 3656–3672.

Schneider, T., P. A. O'Gorman, and X. J. Levine, 2010: Water vapor and the dynamics of climate changes. *Rev. Geophys.*, **48**, RG3001.

Seifert, A. and K. D. Beheng, 2001: A double-moment parameterization for simulating autoconversion, accretion and selfcollection. *Atmos. Res.*, **59**, 265–281.

Seifert, A. and K. D. Beheng, 2006: A two-moment cloud microphysics parameterization for mixed-phase clouds. Part 1: Model description. *Meteor. Atmos. Phys.*, **92**, 45–6.

Shu, C.-W. and S. Osher, 1988: Efficient implementation of essentially non-oscillatory shock-capturing schemes. *J. Comput. Phys.*, **77**, 439–471.

Siebesma, A., 1998: Shallow cumulus convection. *Buoyant Convection in Geophysical Flows*, E. Plate, E. Fedorovich, D. Viegas, and J. Wyngaard, Eds., Springer Netherlands, NATO ASI Series, Vol. 513, 441–486.

Siebesma, A. P. and J. W. M. Cuijpers, 1995: Evaluation of parametric assumptions for shallow cumulus convection. *J. Atmos. Sci.*, **52**, 650–666.

Siebesma, A. P., P. M. M. Soares, and J. Teixeira, 2007: A combined eddy-diffusivity mass-flux approach for the convective boundary layer. *J. Atmos. Sci.*, **64 (4)**, 1230–1248.

Siebesma, A. P. and J. Teixeira, 2000: An advection-diffusion scheme for the convective boundary layer: Description and 1D results. *American Meteorological Society 14th Symposium on Boundary Layers and Turbulence*, 133–136.

Siebesma, A. P., et al., 2003: A large eddy simulation intercomparison study of shallow cumulus convection. *J. Atmos. Sci.*, **60 (10)**, 1201–1219.

Smagorinsky, J., 1963: General circulation experiments with the primitive equations. I. the basic experiment. *Mon. Wea. Rev.*, **91**, 99–164.

Soares, P. M. M., P. M. A. Miranda, A. P. Siebesma, and J. Teixeira, 2004: An eddy-diffusivity/mass-flux parametrization for dry and shallow cumulus convection. *Quart. J. Roy. Meteor. Soc.*, **130 (604)**, 3365–3383.

Sobel, A. H., J. Nilsson, and L. M. Polvani, 2001: The weak temperature gradient approximation and balanced tropical moisture waves. *J. Atmos. Sci.*, **58**, 3650–3665.

Soden, B. J. and I. M. Held, 2006: An assessment of climate feedbacks in coupled ocean-atmosphere models. *J. Climate*, **19 (14)**, 3354–3360.

Sommeria, G. and J. W. Deardorff, 1977: Subgrid-scale condensation in models of nonprecipitating clouds. *J. Atmos. Sci.*, **34**, 344–355.

Stephens, G., 1978: Radiation profiles in extended water clouds. II: Parameterization schemes. *J. Atmos. Sci.*, **35 (11)**, 2123–2132.

Stephens, G. L. and T. D. Ellis, 2008: Controls of global-mean precipitation increases in global warming GCM experiments. *J. Climate*, **21**, 6141–6155.

Stevens, B., 2005: Atmospheric moist convection. *Ann. Rev. Earth Planet. Sci.*, **33**, 605–643.

Stevens, B., 2007: On the growth of layers of nonprecipitating cumulus convection. *J. Atmos. Sci.*, **64 (8)**, 2916–2931.

Stevens, B. and S. Bony, 2013: What are climate models missing? *Science*, **340**, 1053–1054.

Stevens, B. and A. Seifert, 2008: Understanding macrophysical outcomes of microphysical choices in simulations of shallow cumulus convection. *J. Meteor. Soc. Japan*, **86A**, 143–162.

Stevens, B., et al., 2005: Evaluation of large-eddy simulations via observations of nocturnal marine stratocumulus. *Mon. Wea. Rev.*, **133 (6)**, 1443–1462.

Sundqvist, H., 1988: Parameterization of condensation and associated clouds in models for weather prediction and general circulation simulation. *Physically-Based Modelling and Simulation of Climate and Climatic Change*, M. Schlesinger, Ed., Springer Netherlands, NATO ASI Series, Vol. 243, 433–461.

Sušelj, K., J. Teixeira, and D. Chung, 2013: A Unified Model for Moist Convective Boundary Layers Based on a Stochastic Eddy-Diffusivity/Mass-Flux Parameterization. *J. Atmos. Sci.*, **70**, 1929–1953.

Teixeira, J., et al., 2011: Tropical and subtropical cloud transitions in weather and climate prediction models: The GCSS/WGNE Pacific Cross-section Intercomparison (GPCI). *J. Climate*, **24 (20)**, 5223–5256.

Tiedtke, M., 1993: Representation of clouds in large-scale models. *Mon. Wea. Rev.*, **121 (11)**, 3040–3061.

van der Dussen, J. J., S. R. de Roode, S. D. Gesso, and A. P. Siebesma, 2015: An LES model study of the influence of the free tropospheric thermodynamic conditions on the stratocumulus response to a climate perturbation. *J. Adv. Model. Earth Sys.*, **7 (2)**, 670–691.

vanZanten, M. C., et al., 2011: Controls on precipitation and cloudiness in simulations of trade-wind cumulus as observed during RICO. *J. Adv. Model. Earth Sys.*, **3 (2)**.

Vial, J., J.-L. Dufresne, and S. Bony, 2013: On the interpretation of inter-model spread in CMIP5 climate sensitivity estimates. *Climate Dyn.*, **41 (11-12)**, 3339–3362.

Webb, M. J., et al., 2006: On the contribution of local feedback mechanisms to the range of climate sensitivity in two GCM ensembles. *Climate Dyn.*, **27 (1)**, 17–38.

Witek, M. L., J. Teixeira, and G. Matheou, 2011: An integrated TKE-based eddy diffusivity/mass flux boundary layer closure for the dry convective boundary layer. *J. Atmos. Sci.*, **68 (7)**, 1526–1540.

Wood, R. and C. S. Bretherton, 2006: On the relationship between stratiform low cloud cover and lower-tropospheric stability. *J. Climate*, **19 (24)**, 6425–6432.

Zhang, M., et al., 2013: CGILS: results from the first phase of an international project to understand the physical mechanisms of low cloud feedbacks in general circulation models. *J. Adv. Model. Earth Sys.*, **5 (4)**, 826–842.